Dynamic Spatio-Temporal Interaction of Morphogens, Forces and Growth in Embryonic Morphogenesis

Ying Zhang

Submitted to the faculty of the University Graduate School

in partial fulfillment of the requirements

for the degree of

Doctor of Philosophy

in the Department of Physics,

Indiana University

August 14, 2007

Accepted by the Graduate Faculty, Indiana University, in partial fulfillment of the requirements for the degree of Doctor of Philosophy.

Doctoral
Committee

James A. Glazier, Ph.D.

John M. Beggs, Ph.D.

Andrew J. Hanson, Ph.D.

Anton W. Neff, Ph.D.

Santiago D. Schnell, Ph.D.

_____, 2007

Acknowledgement

First of all, I would like to thank my advisor Dr. James A. Glazier for his patience, support, excellent supervision and provision of various learning opportunities. His guidance and care were indispensable factors in my accomplishment. His comprehensive knowledge of morphogenesis modeling and broad interests in multidisciplinary research lead me to a scientific world of fascinating discoveries and advanced technologies.

I am extremely grateful to Dr. Anton Neff for his delightful kindness and for his guidance in biology, from the semester I moved from the University of Notre Dame to Bloomington, until the day I finished my graduate studies. Additionally, I am deeply indebted to Dr. Santiago Schnell, Dr. John Beggs and Dr. Andrew Hanson for their kindness and guidance and to Dr. Mike Levin for encouraging me to continue in scientific research.

Many scientists have been generous hosts to me during my thesis research. I would like to thank Dr. Gabor Forgacs, whose hard work and enthusiasm for scientific achievement encouraged me, and whose care for me made me feel not like a research team member, but a valued family member during my visits to his laboratory. I was deeply impressed by Dr. Stephen Wolfram, the successful CEO of Wolfram Research, who has spent much time guiding students in their research and helping them solve complex questions and who generously discussed fundamental science with me. I am very grateful to Dr. Stuart A. Newman, whose deep insight into both the biology and physics of interdisciplinary problems in developmental biology provided great guidance and encouragement. I was greatly

influenced by Dr. Rusty Lansford who taught me to design and conduct accurate and repeatable biological experiments. His guidance has helped me to avoid wasting tremendous amounts of time collecting and attempting to interpret meaningless data.

I gratefully acknowledge the help of many members of Dr. Glazier's group and of the many laboratories I have visited and of the staff in the Biocomplexity Institute and Department of Physics at Indiana University, especially Dr. Maciej Swat, Dr. Ariel Balter, Dr. Nikodem Poplawski, Benjamin Zaitlen, Scott Chris, Natalie Bronstein, Christiane Hassel, Betsy Osborne and Sue Childress. I also acknowledge discussions, suggestions, criticisms and support from Adam Sheya and Dr. Michael Trosset from the Indiana Statistical Consulting Center, which greatly helped my research. David Sprinkle, Mike Hosek and Philip Childress helped me set up a running laboratory; which would have been impossible for me otherwise. Beth Reeves help me set up a biosafety-II-standard laboratory for my retrovirus work.

I would like to acknowledge other great scientists, including Dr. James W. Nelson, Dr. Gary Nolan, Dr. Cliff Tabin, Dr. Masatoshi Takeichi, Dr. Niswander Lee, Dr. Stephen H. Hughes, Dr. Philip Maini, Dr. Oliver Pourquié and Dr. David Stocum for their kindness and help, which not only supported my research but also encouraged my idealistic love of science despite real-world frustrations.

Last and most, I would like to thank my family, my root and spiritual source through happiness, sadness, failure and success.

Abstract

My dissertation investigates the important biological/biophysical question of how dynamic spatio-temporal interactions among morphogens, forces and growth determine embryonic morphogenesis. I first explore cell sorting due to continuous variations in inter-cellular adhesion. My analysis connects molecular signaling pathways to cell-level morphogenesis and suggests one way to translate genetic information into tissue structure. Next, I consider the role of differential adhesion in somite segmentation, a much more complicated phenomenon than cell sorting. My results suggest how adhesion and repulsion coordinate to induce segmentation. Again, my analysis connects the molecular regulation within cells to macroscopic patterning *via* control of the physical properties of cells. Finally, I use chick-limb micromass cultures to study the role of the fibroblast growth factors, FGF4 and FGF8, in limb growth and patterning. FGF4 and FGF8 induce characteristic growth and patterning in micromass cultures, which suggests a plausible model for limb outgrowth and patterning.

Contents

List of Figures

List of Tables

CHAPTER ONE

MULTISCALE APPROACHES TO EMERGENT PATTERNING DURING EMBRYONIC MORPHOGENESIS

Abstract

Morphogenesis is the formation and differentiation of tissues and organs. Morphogenesis is a puzzle at multiple scales, as diverse patterns at the tissue and organ level emerge from the underlying spatio-temporal dynamics of structurally-sophisticated and functionally-coherent molecular networks and cellular interactions. Biochemical signaling and physical interactions are the two main mechanisms by which I can explain morphogenesis in a mechanistic and, perhaps, quantitative manner. Exploration of morphogenetic questions using a cell-centered approach which crosses molecular, cellular and tissue scales unites these two mechanisms and illuminates emergent and complex morphogenetic behaviors. Experiments on and computational simulations of morphogenesis serve as independent and complementary approaches to discovering the underlying principles of morphogenesis, helping to guide, interpret and validate each other.

1.1 Introduction

During metazoan embryonic *morphogenesis*, patterns and shapes arise as organisms grow. Because life forms are astonishingly diverse, pursuing the underlying principles of development is a restless and never-ending journey full of confrontation, confusion, anxiety and fantasy. From the times of Hippocrates (460 BC – 370 BC) and Aristotle (384 BC – 322 BC), two theories of development competed: *epigenesis*, in which new structures arise progressively, and *preformation*, which suggested that a complete miniature established at the very beginning of development merely grew later. In the 19th century, with the identification of the cell as the basic unit of life, epigenesis displaced preformation, leaving the question of how architecturally-complex, functionally-coherent multicellular structures develop from a single cell. In the 1940s, the discovery that genes encode proteins suggested possible control mechanisms for embryogenesis. In the 1970s and 1980s, the discovery of homeotic genes, which provide positional information to cells, in some ways vindicated the preformationists (for a review, see Gilbert, 2006). However, the genome does not contain a full description of an organism. Instead, by controlling protein production and activity, genes control cell behavior to achieve a final developmental outcome. **Thus, cell behavior links genetic information to tissue-level morphogenesis.**

Neglecting environmental influence, phenotype represents a spatio-temporal integration of genetic, signaling, metabolic, cellular and extracellular behaviors, each of which may have emergent characteristics (Jochen, 2004). Both components and interactions are sophisticated and complex. For instance, *Escherichia coli* has 4,400 genes*, Drosophila melanogaster* has

13,700 genes, and *Homo sapiens* has 27,000 genes (from http://en.wikipedia.org/wiki/Gene, 05/10/07). Each step in the transcription and translation of genes into proteins can be regulated, *e.g.,* by modification of DNA, regulation of transcription, post-transcriptional modification due to RNA transport, splicing and degradation, and post-translational protein modifications. Since genotype does not directly control phenotype, no single gene causes a specific morphogenetic consequence.

Most contemporary theories of morphogenesis fall into one of two philosophical approaches: *Positional-Information Theories* focus on how long-range molecular signaling creates patterns, while *Differential-Adhesion Theories* focus on the role of physical interactions between neighboring cells. Both approaches contribute useful tools for explaining morphogenesis. Unfortunately, developmental biology has tended to view them as competing rather than complementary and to apply them in isolation.

In the 1970s, Dr. Lewis Wolpert, a South-African engineer who became a prominent biologist, proposed his Positional-Information Theory (Wolpert, 1969, 1971, 1996, 2002) to explain how cells interpret genetic information reliably to produce specific and complex multicellular organisms. In this theory, particular types of signaling molecule serve as diffusive morphogens, which form concentration gradients across developmental areas. A cell interprets the levels of particular morphogens in the context of its genetic makeup and developmental history. Positional-Information Theory provides a unifying concept for the developmental regulation of emerging patterns, and inspired scientists to explore biological pattern formation in a mechanistic and quantitative manner. Modern molecular biology has

clarified the fundamental mechanisms of Positional Information and extended the theory by showing that only a relatively small number of genetic networks are essential for morphogenesis (Tabata, 2001). Diffusive morphogens are key molecules which act as the hub nodes for these genetic networks. Open questions include how morphogen gradients form and persist and how cells respond to morphogen gradients (Dillon and Othmer, 1999; Gurdon and Bourillot, 2001; Freeman, 2002; Dillon, *et al.,* 2003; Eldar *et al.,* 2004; Tabata and Takei, 2004; Umulis, *et al.,* 2006; Gregor *et al.,* 2007a, 2007b; Kicheva *et al.,* 2007).

Long before the molecular era, Trembley (1744) and Wilson (1907) demonstrated that *hydra* and marine sponges could regenerate from random mixed aggregates of dissociated cells or minute fragments. Their experiments suggested that clusters of cells have the ability to self-organize, prompting inquiry into how cells recognize each other to form multicellular functional tissues. Later, Townes and Holtfreter (1955) observed that dissociated amphibian embryonic cells would aggregate, sort out and arrange themselves according to their original germ layer. They suggested *Tissue-Specific-Affinities* and *Chemotaxis* as possible sorting mechanisms. In the 1970s, Steinberg confirmed the Tissue-Specific-Affinity mechanism for cell sorting. His *Differentia-Adhesion Hypothesis* (Steinberg, 1963, 1970) explained cell population behavior in terms of pattern rearrangement to maximize cell-cell adhesion. The later discovery of adhesive *cadherins* (Yoshida and Takeichi, 1982) on the cell membrane provided a molecular basis for cell-type-specific cell-cell adhesion and surface tension (Foty and Steinberg, 2005). Additional types of adhesion molecules can also affect cell-cell adhesion and cell sorting (Gumbiner, 2005), though analysis of the contributions of adhesion molecules to cell sorting has largely focused on the *classic cadherins*, a subfamily of

cadherins that interacts with the actin cytoskeleton *via catenins*. Extensive studies have found that adhesion molecules send signals to and are regulated by genetic-regulatory and signal-transduction pathways (for reviews, see Nelson and Nusse, 2004; Gumbiner, 2005; Halbleib and Nelson, 2006) and also modulate intercellular physical behaviors.

Because of the apparent disjunction between the two dominant patterning theories, experiments on morphogenesis have tended to have either a biochemical or a physical focus. Similarly, mathematical models of development split into two distinct schools, *e.g.*, in explaining cartilage patterning, positional reaction-diffusion models consider the interactions of two morphogens, an activator and an inhibitor; while mechanical-contraction models focus on physical interactions of cells. Both types of model can explain certain aspects of development and fail to explain others. Progress requires integration of biochemical and physical approaches, which is why the multiscale approach I employ in this thesis combines biochemical and physical elements.

1.2 Multiscale Approaches to Development

In spite of the complexity of biological development, simple molecular screens have identified many single genes or proteins that appear to play specific roles during embryogenesis, while high-throughput screens, such as genomic microarrays, mass-spectrometry-based proteomics and yeast-two-hybrid analysis, have produced large-scale data to identify possible functional components of biological networks and their interactions.

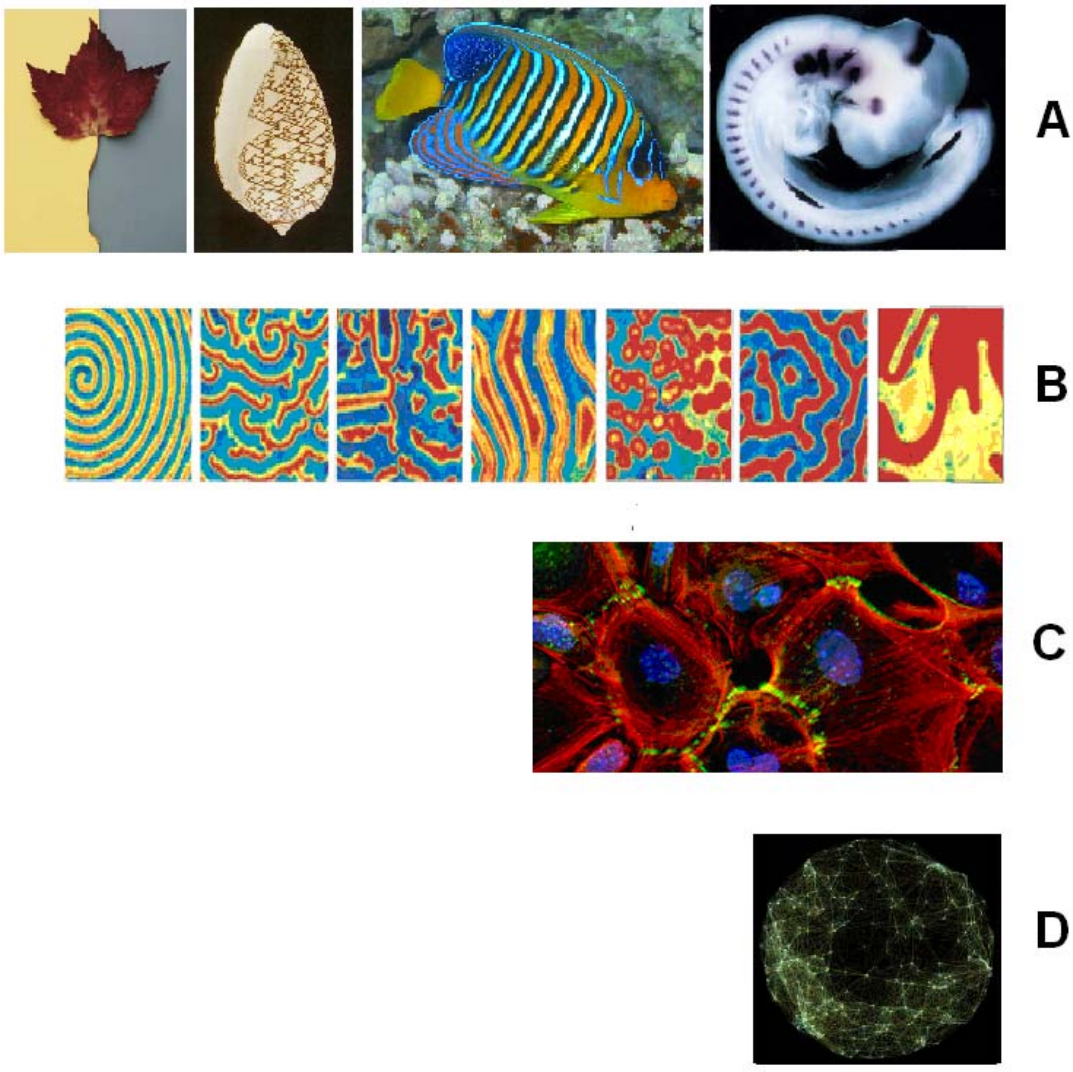

Figure 1.1: Complexity at multiple scales. A. Biological pattern diversity. From left to right: maple leaf (from http://en.easyart.com), cone shell (from http://www.rudzick.de/), Egyptian royal angelfish (from http://www.richard-seaman.com/) and three-day chick embryo (Gilbert, 2006). **B.** Pattern diversity of a non-biological chemical reaction: experimental spatial patterns of the *Belousov-Zhabotinsky* (*BZ*) reaction driven at different frequencies (Lin *et al*., 2000). **C.** Mechanics of cell-cell interactions: green–cadherins, blue–nuclei, red–actin cytoskeletons (from http://newswire.rockefeller.edu/). **D.** Genetic network;

green dots are nodes (from http://network-infinity.stumbleupon.com/). Diverse life forms begin with complex interactions at the molecular level. From the bottom, up: thousands of genes and other molecules form highly-connected signaling networks with specific functions (D). These networks determine the expression and activity of subcellular proteins, which determine cell-level behaviors, such as cadherin binding between cells (C). These cell behaviors give rise to specific patterns at the tissue level (B). The tissues, in turn, organize into diverse complex life forms, from leaves to vertebrates (A). Hence, to decode the origin of organismal diversity and specificity requires exploring function, structure and expression at the molecular level, understanding essential elements at each individual level, and linking information between levels.

However, molecular-level approaches are still not capable of explaining how a genotype gives rise to a phenotype, *i.e.,* how genetic information translates into morphology. Multiscale approaches (Chaturvedi *et al.,* 2005; Merks and Glazier, 2005; Christley *et al.,* 2007; Mackenzie, 2006; Schnell *et al.,* 2007) may help. **The basic multiscale philosophy is to describe and integrate components and interactions within and between subcellular, cellular, tissue and organ scales.** Understanding morphogenesis as the emergent outcome of smaller-scale components may prove valuable in clinical application, such as drug design and gene therapy.

To build a multiscale model, I begin by including the key components and interactions of a biological phenomenon at each spatial scale, based on current understanding and the

capabilities of my simulation tools. I then identify linkages between each pair of levels I consider. The particular simplifications of biological reality and the range of scales I consider vary with the specific questions the model addresses.

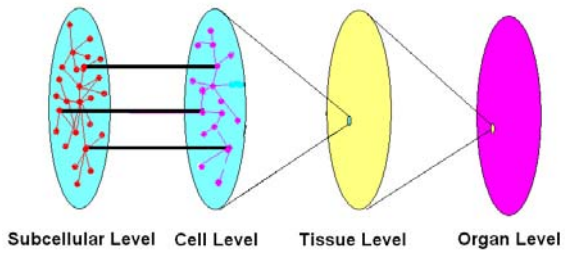

Subcellular: Gene,
Protein: Cadherins, Integrins, Cytoskeleton, Extracellular Matrix, Morphogens.

Cell: Physical Interactions, Biochemical Signaling

Tissue… Organ…

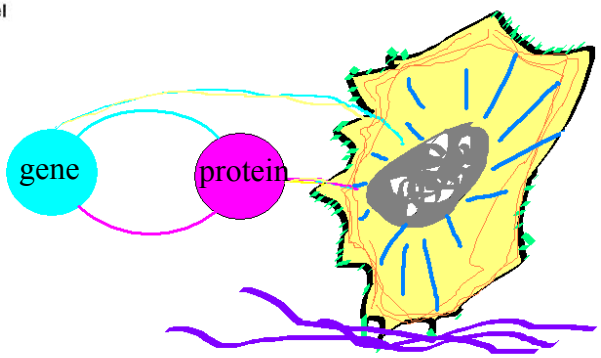

Figure 1.2: Multiscale aspects of morphogenesis. At the subcellular/molecular level, genetic, signaling and metabolic networks regulate key molecules (such as cadherins, integrins, and cytoskeletal and extracellular matrix (*ECM*) components), which determine cell behaviors. Cell behaviors give rise to patterns at the tissue level and to anatomical architecture at the organ level.

Since genes control cell behaviors through protein production and modification and the behaviors of interacting cells give rise to emergent morphologies, in this thesis, I adopt a

cell-centered approach (Merks and Glazier, 2005) **in which cells and the molecules that modulate their behaviors are the key components** (Newman *et al.,* 2006). In this chapter, I describe genetic-regulatory and signal-transduction cascades and how they affect cell behaviors. The transition from cells to tissue-level patterns forms the core of the subsequent chapters, which I will not review here. Large scales, *e.g.,* whole organs, are beyond the scope of this thesis.

1.2.1 Cell-Level Interactions

The cell is the basic unit of tissues and organs. How a cell interacts with other cells to reach and recognize its position or status is crucial to tissue patterning. I first categorize various cell-cell and cell-environment interactions as physical or biochemical, then consider their interplay. Both physical and biochemical interactions can cause cells to migrate, divide, grow, die, differentiate and switch between epithelial and mesenchymal types.

1.2.1.1 Cell-Cell Adhesion and Repulsion

Molecules on the cell membrane can lead to both cell-cell adhesion and effective cell-cell repulsion. The binding of corresponding cadherins on the membranes of apposing cells causes cell-cell adhesion, the strength of which depends on extracellular calcium concentration and the number, types, conformations and distributions of cadherins. Cadherin binding specificities and expression levels both affect the final shape of morphogenetic

boundaries between compartments (A tissue *compartment* is a group of cells which stay together during development, forming a coherent structural component. Sharp morphogenetic boundaries usually divide compartments from each other, and cells from one compartment normally do not cross into another compartment). The binding of Eph receptors on one cell to their ephrin ligands on another cell can trigger cytoskeletal collapse in both cells, causing them to retract from touching each other in a complex mechanism that in many ways resembles a repulsive interaction (Poliakov *et al.,* 2004).

1.2.1.2 Cell-Substrate Adhesion

During morphogenesis, besides the cell-cell adhesion and repulsion involved in establishing compartment boundaries, *extracellular matrix* (*ECM*) proteins also help to stabilize structures and maintain boundaries (Downie and Newman, 1994, 1995). ECM can also transmit long-range forces to regulate morphogenesis at large scales (Kulesa *et al.,* 2007). Cells bind to ECM *via integrins*, which, like cadherins, both regulate and are regulated by intracellular signaling cascades. This bidirectional signaling creates feedback loops, which regulate cell behavior and modulate the cellular environment, *e.g., via haptotaxis*, where cells migrate up or down gradients of chemicals or mechanical properties in the ECM (Rhoads and Guan, 2007).

1.2.1.3 Biochemical Signaling between Cells

Secretion and absorption of diffusible molecules by receptor-ligand binding on cell membranes and/or chemical coupling through gap junctions can all cause cells to change their behaviors. Such changes are crucial to embryonic patterning.

Signaling can be *hierarchical* or *reciprocal* (Salazar-Ciudad *et al.,* 2003). In *hierarchical* signaling, a cell affects another cell but is not influenced by the receiving cell. In *reciprocal* signaling, the cell sending signals is affected by the receiving cell's responses. Reciprocal signaling can lead to emergent or self-organized patterns, *e.g.,* by activator-inhibitor mechanisms (Gibert, 2006). Most morphogenesis involves both types of behavior. *E.g.*, in both fish-skin and butterfly-wing patterning, a self-organized prepattern of activators and inhibitors leads to hierarchical differentiation of the final pattern, while in somitogenesis and limb outgrowth, a partially self-organized pattern of gene expression leads to hierarchical differentiation and then to self-organized cell rearrangement.

During embryonic development, the most striking events involve long-range, coordinated cell migration. During gastrulation, epithelial cells migrate into the primitive groove to form the third germ layer. Both cell-substrate-adhesion and diffusive-molecule gradients can guide cell motion (Rhoads and Guan, 2007). To build multicellular structures, cells must migrate to specific locations at specific times in response to signals in their local environment. Cell migration on a substrate requires coordinated activity of a cell's cytoskeleton, membrane and adhesion molecules. For a cell to move forward, it must:

1) Protrude in the direction of motion by forming and extending lamellipodia, filopodia or pseudopods;
2) Create an adhesive contact between the cytoskeleton and substrate in the new region of contact;
3) Selectively deadhere its trailing edge;
4) Retract its trailing edge, which leads to forward movement of the cell body.

Cell movement in response to the external environment requires self-organized force generation and transduction, signaling loops to regulate cytoskeleton assembly and disassembly, and energy generation and consumption.

1.2.2 Molecular-Level Considerations

Cadherins, Eph and ephrin, integrins and cytoskeletal proteins are all essential to controlling cell behavior during patterning. These molecules induce and/or transduce cell motility and cell-cell and cell-ECM physical interactions. Various signaling pathways regulate the expression and behavior of these molecules (*e.g.*, those involving fibroblast growth factors). The molecules may themselves modify signaling cascades through regulatory feedback loops. Thus, understanding the regulation and signaling of these proteins in detail is a crucial step in extracting the key aspects of the genetic-regulatory and signal-transduction networks to allow construction of manageably-simple models.

Below, I describe the regulation and signaling loops for classic cadherins, the most intensively-studied cell-cell adhesion molecules, to demonstrate the intimate links among networks, protein activities and expression. This example illustrates the complexity of interactions between genes and proteins: multiple gene and signal cascades dynamically regulate cadherin expression and activity, creating complex spatio-temporal patterns.

I also discuss the regulation and signaling loops for Ephs and ephrins, which can cause cell-cell repulsion, and for intergrins, which generate the main adhesion between cells and ECM.

1.2.2.1 Cadherin Regulation and Signaling

Cadherins are a large family of cell-cell adhesion molecules, expressed in complex patterns during embryonic development (for a review, see Gumbiner, 2005). The four main subfamilies of cadherins are: the *desmosomal cadherins*, the *proto-cadherin*s, the *cadherin-like proteins* and the *classic cadherins*. Classic cadherins are trans-membrane proteins, whose C-terminals bind to the cytoskeleton *via* catenins. They transmit mechanical forces to the cell and can affect cell shape and motility (Gumbiner, 2005). Signaling cascades precisely regulate cadherin numbers, subtypes and conformational structures, modulating cadherin expression and activity. In turn, cadherin binding modifies intracellular signaling cascades in response to mechanical interactions (for reviews, see Tepass *et al.,* 2000; Gumbiner, 2005; Halbleib and Nelson, 2006). In order to understand how signaling networks and cadherin interactions help translate genetic information into pattern requires detailed understanding of cadherin regulation and signaling.

Fig. 1.3 shows some elements of the signaling and regulatory loops involving cadherins. Changes in gene expression, transport to the cell surface and protein turnover all affect membrane levels and activities of cadherins. *E.g., Fibroblast Growth Factor-2* (*FGF-2*) can upregulate N-cadherin expression in human calvaria osteoblasts (Debiais *et al.,* 2001). Methylation and repression of promoter activity directly downregulate cadherin transcription. *E.g.,* zinc-finger proteins of the *Slug/Snail* family and *Smad-Interacting Proteins* (*SIP1*) can repress E-cadherin gene transcription. Fibroblast-growth-factor (*FGF*) and Wnt signaling cascades both can regulate Snail, while Slug may be a target gene of the *T-cell factor* (*TCF,* a transcription factor)/*β-catenin* complex, which is related to the Wnt signaling pathway. Smad is a member of the *Sonic Hedgehog* (*Shh*) signaling pathway. Thus, FGF-, Wnt- and Shh-cascades, the most active signaling cascades during embryonic development, can all regulate cadherin expression. Binding of β-catenin facilitates transportation of cadherin to the plasma membrane. Phosphorylation, ubiquitination, and proteolysis also regulate membrane cadherin levels (Halbleib and Nelson, 2006). Since cadherins connect to the actin cytoskeleton *via* α-catenin and β-catenin, they can modulate Wnt transcription by sequestering β-catenin from the cytosol, and by competing with TCF for β-catenin. Both β-catenin and the TCF/β-catenin complex function as Wnt transcription factors (Gumbiner, 2005).

The complexity of cadherin regulation and signaling shows why a simple description of cadherin expression and activities is simultaneously so desirable and so difficult to achieve.

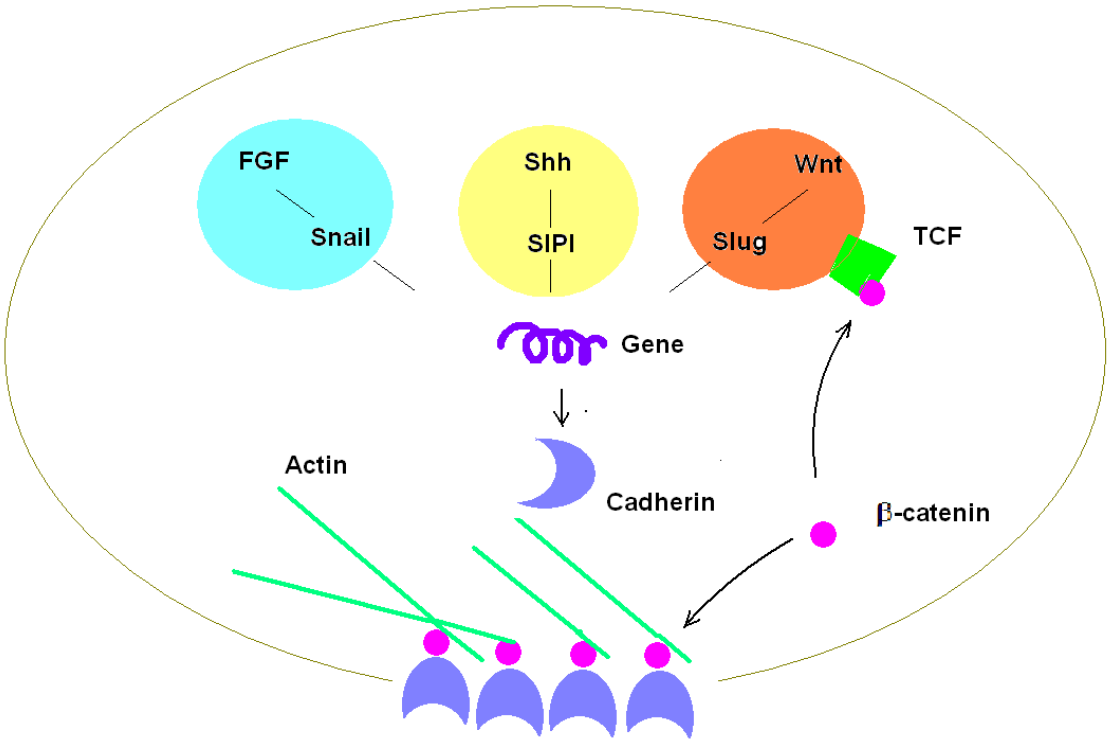

Figure 1.3: Cadherin regulation and signaling. The expression of cadherins can be regulated by common signaling pathways, such as the FGF, Shh and Wnt cascades. In turn, cadherins may regulate signaling cascades, *e.g.*, modifying the Wnt cascade through β-catenin. The binding of cadherins on apposing cells generates intercellular mechanical forces, which are transferred into the cell through the cytoskeleton, *e.g.*, *via* actin filaments.

1.2.2.2 Eph/ephrin Regulation and Signaling

Cell-cell repulsion is also important to both embryonic and adult morphogenesis. Repulsive interactions between transmembrane Eph receptors and their ephrin ligands are required for tissue compartmentalization, neurite outgrowth, angiogenesis and oncogenesis (Murai and

Pasquale, 2003). The Eph receptors are a large family of receptor tyrosine kinases with at least ten EphA and six EphB receptors. Ephrins also form a large family, with six *glycosylphosphatidylinositol* (*GPI*)-Anchor-linked ephrin-A ligands and three transmembrane ephrin-B ligands in vertebrates (Hirai *et al.,* 1987; Murai and Pasquale, 2003).

The binding of Eph receptors on one cell to ephrin ligands on an apposing cell triggers signaling in both cells, modulating cell shape, adhesion and movement (Murai and Pasquale, 2003). Various transcription factors help create the complex patterns of Eph and ephrin expression observed in development. TCF/β-catenin signaling can simultaneously upregulate some Eph receptors and downregulate some ligands in the intestine. During somitogenesis, the *Notch/Delta* pathway regulates Eph expression through *Mesp*, a transcription factor, which also represses DLL expression. DLL, in turn, maintains ephrin expression. Some homeobox genes regulate expression of Eph receptors or ephrins. For example, Vax2 modulates EphB2 in the developing retina and the Krox-20 zinc finger regulates Eph during hindbrain segmentation. Translation of Eph receptors is restricted to specific subcellular compartments during axon growth.

Eph receptors regulate cytoskeletal dynamics *via Rho-family small GTPases* (Rho, Rac and Cdc42). Rac promotes lamellipodia and Cdc42 promotes filopodia, increasing cell motility and adhesion. Rho activation reduces cell motility and adhesion, causing collapse of growth cones, retraction of cell processes, cell rounding and detachment. Binding to Eph receptors reduces the activity of H-Ras, which can increase cell proliferation and modulate cell

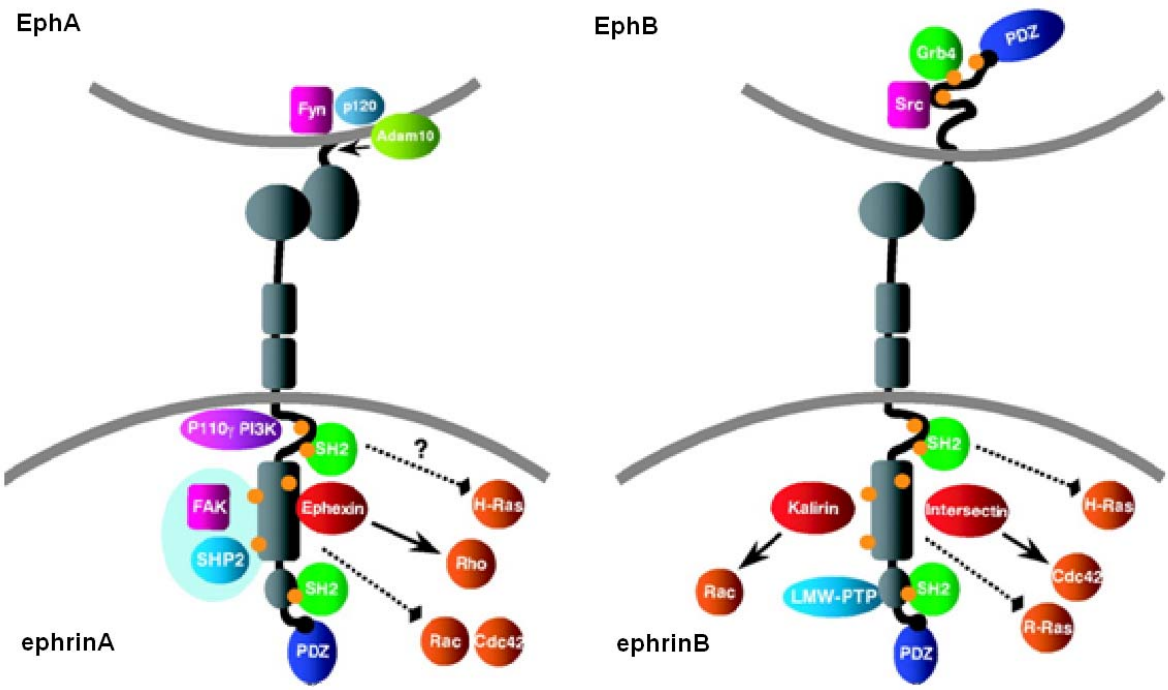

Figure 1.4: Forward and reverse signaling cascades resulting from Eph/ephrin interaction. The binding of Eph receptors (Gray color. Left, EphA. Right, EphB) to ephrin receptors (Gray color. Left, ephrinA. Right, ephrinB) on apposing cells triggers bi-directional signaling cascades: Eph or ephrin intracellular domains bind to cytoplasmic proteins, such as Ephexin and Kalirin, which interact with FAK or Rho-, Ras- and Rac-family small GTPases, modifying cells' motilities and adhesion properties (Picture from Murai and Pasquale, 2003).

migration (Murai and Pasquale, 2003). Ephrin signaling may act through proteins containing Src homology-2 (*SH2*) or PSD95/Dlg, ZO-1 (*PDZ*) binding motifs to regulate focal-adhesion-kinase (*FAK*) and mitogen-activated-protein-kinase (*MAPK*) activity, and modulate cell-ECM binding (Murai and Pasquale, 2003).

1.2.2.3 Integrin Regulation and Signaling

Integrins are transmembrane heterodimers with α- and β-subunits. Mammals have twenty four distinct integrins combining one of eighteen α-subunits with one of eight β-subunits. Integrins bind to extracellular proteins, including fibronectin, collagen and laminin and to the cytoskeleton (in particular to microfilaments) through scaffolding proteins like talin, paxillin and α-actinin, allowing them to transmit information about cell-substrate interactions to cells. Integrins interact with other cell-surface receptors, including growth-factor receptors, activating signaling pathways and affecting cell proliferation, differentiation, shape and motility (for reviews, see Hynes, 2002; Moissoglu and Schwartz, 2006).

1.2.3 Tissue-Level Considerations

While we know the least about morphogenesis at this level, boundary and initial conditions seem to be the primary determinants of tissue organization.

1.2.4 Summary

In this thesis, I focus on **cadherins, integrins and Ephs/ephrins, since they are the most important bridges which connect gene activity to cell behavior. Because they are regulated by genetic cascades, modulate signaling pathways and control many**

mechanical interactions at the cell level, they transfer information from the molecular to the cellular level.

1.3 Emergent Patterning during Embryonic Development

Emergence is an essential and fundamental aspect of morphogenesis. A few classical theoretical and experimental examples illustrate pattern emergence from simple interactions of two or more factors. The *Keller-Segal* model (Keller and Segal, 1971) of the spiral patterns of cell migration during *Dictyostelium discoideum* cell aggregation employs two coupled *partial-differential equations* (*PDE*s). An equation for cell density describes *chemotaxis* (in which cells migrate up or down gradients of certain diffusing chemicals). A second equation describes concentration changes of the signaling chemical *cAMP* due to diffusion, decay and cell secretion. The interplay of chemotaxis and diffusion results in spiral-wave chaos (Van Oss *et al.,* 1996). Similar equations describe cardiac fibrillation (Bernus *et al.,* 2003). In *Turing-type reaction-diffusion* models (Turing, 1952; Newman and Frisch, 1979; Sick *et al.,* 2006), the diffusion-driven instability of an activator and an inhibitor creates stable, static patterns.

During embryonic development, proliferation and death of cells complicate morphogenesis. *E.g.,* in cartilage patterning during vertebrate limb development, the mesenchymal precursors to the cartilage cells must develop while the limb grows from an initially-homogeneous mesenchymal cluster of cells. A structure at the distal end of the limb, the *Apical Ectodermal*

Ridge (*AER*) is essential to limb growth and patterning. Currently, two different models compete to explain its role, the *progress zone model,* which focuses on the AER's regulation of differentiation (Summerbell and Wolpert, 1973), and the *early-specification model* (Richardson *et al.,* 2004), which focuses on the AER's role in growth. Choosing between the models is complex, especially since molecular expression studies support neither one (Duboule, 2002; Saunders, 2002; Wolpert, 2002; Tabin and Wolpert, 2007). Thus limb development shows that patterning and growth can be indispensable for each other and that molecular details are required to explain morphogenesis at the tissue level, necessitating a multiscale approach.

1.4 Relations among Experiment, Modeling and Simulation

Biological experiments normally suggest possibilities rather than prove causal relations, both because single genes or proteins rarely cause morphological consequences directly, and because the networks regulating morphogenesis are redundant. Thus, observation and interpretation are context dependent. The current state of experimental technology further prevents many potentially definitive experiments.

Mathematical modeling and computer simulations complement experiments. Models allow simple and clear determination of cause and effect. Analytical or numerical stability analysis can probe the origins of complicated emergent behaviors. However, building models and simulations requires limiting the number of parameters and assumptions, and hence requires

radical simplification of biological complexity. Both computer technology and the lack of experimentally-measured parameter values thus limit the scope and accuracy of simulations.

Experiments and simulations need to be used together to uncover even approximate truth. Simulations can predict and guide experiments, while experiments offer reference points for simulations. In this thesis, wherever possible, I apply both experimental and computational approaches to each biological question.

1.5 Thesis Outline

Cell-cell adhesion caused by cadherins is fundamental to biological morphogenesis. Besides producing physical forces between cells, cadherins are also regulated by and affect signaling cascades. An intensive exploration of how cadherins induce pattern formation is critical to a final understanding of how genotype leads to phenotype. In Chapters Two and Three, I observe sorting of cells which express a continuous range of cadherin levels experimentally, construct a multiscale model of sorting and explore cell-sorting kinetics using computer simulations.

However, patterning requires more than cell-cell adhesion. Cell-ECM interactions and cell-cell repulsion are also elements of morphogenesis. During somitogenesis, somites separate from the presomitic mesoderm sequentially along the rostro-caudal body axis. In chick, transient oscillations of gene expression must translate into a fixed, spatially-periodic pattern

of somites. In Chapter Four, I propose and validate by simulation that the coordination of cell-cell adhesion caused by N-cadherin and N-CAM and of cell-cell repulsion induced by Eph/ephrin pairs translates the oscillatory prepattern into stable morphological structures.

FGFs are key molecules in almost all embryonic morphogenesis, *e.g.,* limb cartilage patterning. FGFs play multiple roles, controlling cell proliferation, differentiation, migration and survival. In Chapter Five, I use limb-cell micromass-culture experiments to quantify the effects of FGF4 and FGF8 on chondrogenic patterning and cell division. I assay the changes in the *average interval* (the distance between chondrogenic nodules) and average division rates of cells in response to different FGF treatments, and propose a plausible model for limb outgrowth and patterning based on these results.

In the final chapter, I present a possible mechanism for the emergence of left-right asymmetry during early chick development and suggest possible experimental and computational approaches to validate my hypotheses.

CHAPTER TWO

EXPERIMENTS ON CELL SORTING DUE TO DIFFERENTIAL ADHESION

Abstract

While cell-adhesion molecules are essential to embryonic development, wound healing, immune response and cancer metastasis, significant uncertainty remains about how adhesive interactions between pairs of apposing molecules on cell membranes contribute to the formation of morphological structures. Prior experiments have studied sorting between two or three cell types, each expressing uniform levels of one or more adhesion molecules. However, none studied the developmentally-significant case of cells expressing multiple or continuously-variable levels of a single adhesion molecule. I studied sorting of cells expressing varying levels of a single cadherin molecule, E-cadherin. I transfected Chinese Hamster Ovary cells, which are normally non-adhesive, to create a polyclonal cell line, which expressed a wide range of levels of an E-cadherin-GFP fusion-protein. I then examined their sorting in aggregates. Cadherins clustered at the edges of cell-cell contact surfaces, consistent with expectations from two-dimensional experiments. I then used these cells to form aggregates and observed their sorting dynamics. Cells with high and low cadherin expression first formed homotypic clusters, then evolved towards a fully-sorted

configuration, with cells expressing more cadherins near the center and cells expressing fewer cadherins at the periphery of aggregates, though sorting appeared less complete than for classical sorting between two distinct cell types.

2.1 Introduction

The *cadherin* family of cell-adhesion membrane proteins plays a key role in both early and adult tissue morphogenesis (Radice *et al.,* 1997; Price *et al.,* 2002; Gumbiner, 2005). Spatio-temporal variations in cadherins regulate many morphogenetic processes, including: neural-crest-cell migration (Xu *et al.,* 2001), somite segmentation (Linask *et al.,* 1998; Horikawa *et al.,* 1999), epithelial-to-mesenchymal transformations during tumor invasion and metastasis (Takeichi 1993; Berx and Van Roy, 2001), and wound healing (Bement *et al.,* 1993; Lorger and Moelling, 2006). Often these processes involve continuous variations in the expression level of a single adhesion molecule. During proximo-distal limb growth (Yajima *et al.,* 1999) and rostro-caudal body-axis elongation (Bitzur *et al.,* 1994), adhesion gradients may maintain cells' positions. In *Drosophila*, an adhesion gradient drives the oocyte towards the posterior follicle cell, which expresses the highest level of DE-cadherin (Godt and Tepass, 1998). A cell-cell adhesion gradient along the dorso-ventral axis directs lateral cell migration during zebrafish gastrulation (Von der Hardt *et al.,* 2007). Thus, understanding the role of cadherins, especially of continuous variations in the level of a single cadherin, in creating and stabilizing structures is a crucial part of understanding embryonic morphogenesis.

The basic idea that cell sorting results from variations in cell-cell adhesivity comes from Steinberg's *Differential Adhesion Hypothesis* (*DAH*) (Steinberg 1963; Steinberg and Wiseman, 1972; Steinberg and Takeichi, 1994; Foty and Steinberg, 2005). Cell sorting depends on the effective molecular binding strength between apposing cadherins, which depends on their types and expression levels in each cell (Friedlander *et al.,* 1989). Differences in expression levels of a single type of cadherin (Steinberg and Takeichi, 1994; Foty and Steinberg, 2005) and differences in types of cadherins expressed (Niessen and Gumbiner, 2002; Foty and Steinberg, 2005) can both lead to sorting.

The relationship between cadherin binding at the molecular level and cell sorting is quite complicated. Measurements of cadherin binding have employed a wide variety of approaches and obtained widely differing estimates of the cadherin binding force, cell-cell adhesion force and surface tension at the tissue level (Baumgartner *et al.,* 2000; Chu *et al.,* 2004; Panorchan *et al.,* 2006; Foty and Steinberg, 2005; Prakasam *et al.,* 2006). In some experiments, the scaling between cadherin expression levels and surface tension is linear (Foty and Steinberg, 2005); in others, the scaling between cadherin expression levels and the cell-cell adhesion force is quadratic (Chu *et al.,* 2004). Cadherin reorganization into adhesive patches on the cell membrane due to passive diffusion and interaction with the actin cytoskeleton (Angres *et al.,* 1996; Adams *et al.,* 1998; Adams and Nelson, 1998) can greatly increase the effective binding strength per cadherin pair between two cells. Cluster formation depends on the proper functioning of the actin cytoskeleton, since actin-disrupting drugs like cytochalasin-D and latrunculin greatly decrease cell-cell adhesivity (Behrens *et al.,* 1985). The nature of binding may differ for cadherins in different conformational states (Gumbiner,

2005). Cadherin distribution also changes gradually after two cells come into contact (Angres *et al.,* 1996; Adams *et al.,* 1998; Adams and Nelson, 1998; Gumbiner, 2005).

Multiple transcriptional and post-translational signaling cascades can regulate cadherin expression levels and per-cadherin binding strengths (Gumbiner, 2005; Halbleib and Nelson, 2006). In turn, cadherin binding can modify gene expression (Gumbiner, 2005). This complexity obscures the role of the cadherin-binding force in cell sorting (Prakasam *et al.,* 2006). Experiments on specific types of cadherin have led to at least four cadherin-binding models.

Experiments on cell sorting in aggregates simplify this complexity, since observed sorting depends only on the levels of adhesion molecules (Steinberg and Takeichi, 1994). However, these experiments have only studied sorting between two or three cell types, each with defined levels and types of cell-adhesion molecules (Steinberg and Takeichi, 1994; Foty and Steinberg, 2005). To clarify the biologically-important case of continuously-variable levels of a single adhesion molecule, I transfected *Chinese Hamster Ovary* (*CHO*) cells to produce a polyclonal cell line, with cells that expressed a wide range of levels of a single E-cadherin-GFP fusion protein with roughly equal fractions of cells expressing each level present (see Fig. 2.1A-B) and observed the distribution and expression of cadherins in sorting cell aggregates. Since wild-type CHO cells do not express endogenous cadherins and do not adhere to each other (Niessen and Gumbiner, 2002), their cell-cell adhesion is primarily due to the introduced E-cadherin-GFP. During sorting, the E-cadherin-GFP fusion protein reports E-cadherin expression, allowing observation of cadherin distribution during cell-cell

adhesion and cell rearrangement. Such normally non-adherent cell lines transformed to express recombinant cadherins are common experimental models in the study of cell sorting (Nose *et al.,* 1988; Niessen and Gumbiner, 2002; Foty and Steinberg, 2005).

2.2 Material and Methods

2.2.1 CHO-EC7 Cell-Line Construction and Selection

I grew wild-type CHO cells (Sigma) in Dulbecco's modified Eagle medium (*DMEM*, GIBCO) supplemented with 10% fetal bovine serum (*FBS*, GIBCO), 10 units/ml penicillin and 10 μg/ml streptomycin (GIBCO) in a humidified 5% CO_2 atmosphere at 37°C. I transfected the cells using an E-cadherin-GFP plasmid provided by Dr. J. W. Nelson of the Stanford University School of Medicine (Yamada *et al.,* 2005). Briefly, I transfected 60-80% confluent cells with 5 μg plasmid in a 35 mm dish using Qiagen superfection reagent. After 1-2 days of 400 μg/ml G418 selection, I transferred the transfected cells to 100 mm dishes and selected cells expressing E-cadherin-GFP using 400 μg/ml G418 for about two weeks. I isolated cell lines by cloning ring (Nose *et al.,* 1988; Duguay *et al.,* 2003) and analyzed their E-cadherin-GFP expression levels using flow cytometry (BD Biosciences FACS@Calibur). I then observed cell morphology and E-cadherin-GFP distribution within cells using a Leica multiphoton laser-scanning confocal microscope (SP2) to select cell lines positive for E-cadherin-GFP expression on their membranes but with no or little E-cadherin-GFP in their

cytoplasm. I selected one polyclonal cell line, which I denoted *EC7*, whose cells expressed a broad range of E-cadherin-GFP levels with approximately uniform frequency. Because polyclonal lines can be unstable in culture, I cryopreserved this line and serially-cultured cells from the frozen stock for use for no more than one month before restarting from the original frozen stock. I monitored E-cadherin-GFP levels periodically using confocal microscopy to check that the cultured cells had not changed their range of E-cadherin-GFP expression.

2.2.2 Flow-Cytometry Analysis of Cadherin Expression

A *flow-cytometer* uses laminar flow to transport cells one at a time through an excitation laser beam. It detects forward-scattered, side-scattered and fluorescent light from the excited cell to provide information on its physical and biochemical characteristics. *Cell sorters* also allow selection and segregation of cells on the basis of these measurements.

To prepare wild-type and transfected cells for flow-cytometry analysis, I detached the cells from their culture dishes using 0.05% Trypsin-EDTA (Gibco) and stopped the trypsination by adding an equal volume of DMEM with 10% FBS. I centrifuged and resuspended the cells in CO_2-independent DMEM with 2% FBS. I incubated the cells in a rotary shaker at 80 rpm at 37˚C for about 8 hours for flow-cytometry analysis the next morning. I collected, visualized and analyzed the data using CellQuest Pro software. GFP has an excitation wavelength of 488 nm and an emission wavelength of 508 nm. Therefore, I set the laser

excitation to 488 nm in the flow-cytometer and defined two fluorescence collection channels: *FL1-H,* corresponding to GFP fluorescence at 530 ± 30 nm and *FL2-H,* corresponding to *PE* (*phycoerythrin*, a fluorescent dye) fluorescence at 585 ± 42 nm. I used wild-type CHO cells as a negative control to define GFP- and PE-fluorescent negative and positive regions, using a quadrant marker on an FL1-H *vs*. FL2-H two-parameter scatter plot. The marker divides the plot into sub-regions of negative, single-positive, or double-positive subpopulations. Transfected cells should be GFP positive and PE negative and the geometric mean of the fluorescence intensity of the transfected cells should be much bigger than that of the wild-type cells. I collected data on 10,000 cells for each sample.

I also used CellQuest or WinMDI to visualize the data as a GFP-fluorescence histogram to estimate the range of cadherins per cell, assuming that intensity increases linearly with the number of GFP molecules. In the histogram (Fig. 2.1B), the horizontal axis represents the strength of the GFP-fluorescence signal in arbitrary units (channel number out of 1024 channels) and the vertical axis represents the number of events in that channel. I did not attempt to quantify either the fluorescence intensity or the absolute number of GFP molecules per cell.

2.2.3 Ca2+-Dependence Assays

To check that adhesion and cell sorting were due to cadherins, I tested whether cell aggregation required Ca^{2+} in the medium, since cadherin interactions are Ca^{2+} dependent. I

dissociated wild-type and transfected cells using either *TC* treatment (0.01% trypsin with 1 mM $CaCl_2$) or *TE* treatment (0.01% trypsin with 1 mM EGTA) (Nose *et al.,* 1988). Cadherins remain active in TC-treated cells but TE-treatment removes them from the cell surface. Thus, I expected TC-treated cells to form aggregates rapidly (within 1 hour) and TE-treated cells to take longer, because cadherin takes several hours to recover. I aggregated both TC- and TE-treated cells separately in 6-well Petri dishes and incubated them on a rotary shaker (80 rpm) at 37°C. For aggregation assays, I filled each well either with 1×10^6 TC-treated cells in 2 ml *HCMF* (Hepes buffer HBSS CMF) with 1% bovine serum albumin and either no, 0.1 mM or 1 mM $CaCl_2$ for 60 min, or with about 1×10^6 TE-treated cells in 2 ml of CO_2-independent DMEM with 10% FBS. I recorded the images using a 2 × objective in a Nikon inverted microscope in phase-contrast mode.

2.2.4 Production of Cell Aggregates for Cell-Sorting Experiments

I formed cell aggregates following Steinberg's protocol (Steinberg and Takeichi, 1994). I washed near-confluent cells twice with Hank's balanced salt solution (*HBSS*) containing 2 mM $CaCl_2$, then treated them for 15-30 min with trypsin 0.01% (GIBCO) with 1 mM $CaCl_2$. I resuspended the cells in CO_2-independent DMEM with 2% FBS, allowed them to recover from trypsinization for 0.5-2 hours on a shaker at 80 rpm at 37˚C, pipetted the suspensions gently to disperse any aggregates, then pelleted them in round-bottomed culture tubes by brief centrifugation at 1000 rpm in a table-top centrifuge. I incubated the pellets in DMEM with 2% FBS for 3-22 hours, then cut them into small fragments with a microscalpel and

allowed them to round up in DMEM with 2% FBS and 50 μg/ml DNase I (Sigma) on 1.25% agarose-coated Petri dishes (Falcon) at 37˚C in a 5% CO_2 atmosphere. I then selected rounded-up fragments of 150-300 μm in diameter for cell-sorting analysis.

2.2.5 Confocal Imaging

I observed aggregates using a Leica multiphoton laser-scanning confocal microscope (SP2) in both two-photon and conventional confocal modes. For GFP, the two-photon excitation wavelength is 950 nm and the emission wavelength is 500~560 nm. I also stained aggregates with *DAPI* (4',6-diamidino-2-phenylindole, a DNA-targeting fluorescent stain) to localize cells in aggregates. For DAPI, the two-photon excitation wavelength is 710 nm and the emission wavelength is about 470 nm. The two-photon mode uses a neutral-density detector (*NDD*) to collect the fluorescence signal. I further observed the distribution of E-cadherin-GFP on cell membranes either in Petri dishes or in three-dimensional cell aggregates using the microscope's conventional confocal mode with an excitation wavelength of 488 nm and an emission wavelength of 500-560 nm. The conventional confocal mode uses a photomultiplier-tube (*PMT*) detector. For cell-sorting analysis, I cut the fixed two-day, three-day and six-day cell aggregates in half using a microscalpel and laid the cut face on a glass cover-slip in a homemade observation chamber (Kulesa and Fraser, 2002). To reduce photo-bleaching, I scanned three-dimensional images from the bottom to the top of the sample.

2.3 Experimental Results

My transfected cell line, *CHO EC7*, exhibited a continuous variation of E-cadherin-GFP expression levels (Figs. 2.1A-B). The cells' fluorescence in the GFP channel varied over a range of [10, 230] in relative fluorescence strength (arbitrary units indicated by the bin

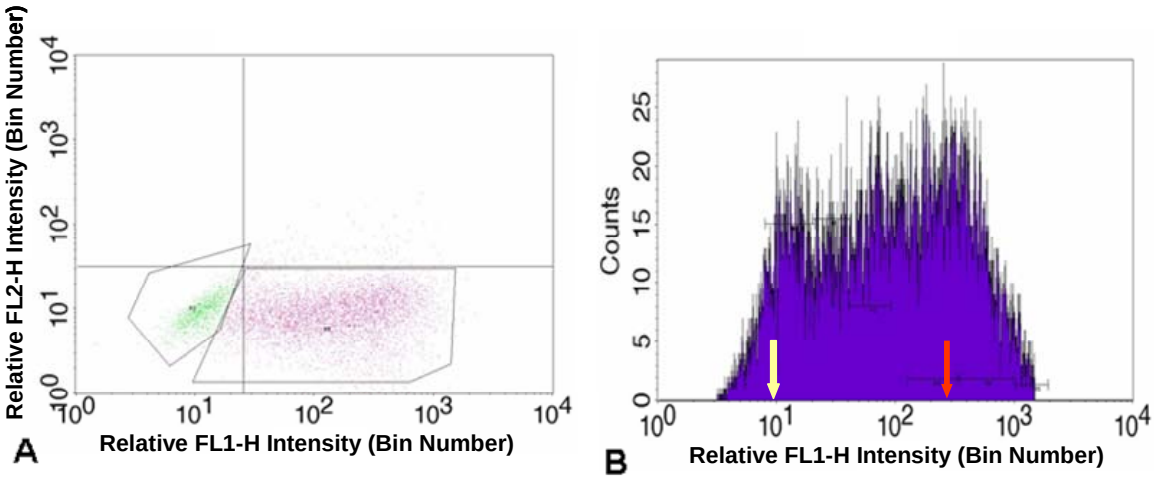

Figure 2.1: Cadherin expression levels in CHO-EC7 cells. A. Flow-cytometry analysis of E-cadherin-GFP expression in the transfected cell line CHO-EC7. Most CHO-EC7 cells are located in the GFP-positive and PE-negative subregion (the lower right quadrant). The lower left quadrant (green) includes GFP-negative cells. The FL1-H fluorescence channel covers a range of 530 ± 30 nm. The FL2-H channel covers a range of 585 ± 42 nm. **B.** Histogram of E-cadherin-GFP expression for CHO-EC7 cells. 10-20 cells fall into each GFP-fluorescence channel, from 10 (the yellow arrow) to 230 (the red arrow). Channel numbers are in units of relative fluorescence strength, given by bin number.

number) with an approximately equal number of cells in each channel. Assuming linear dependence of fluorescence on GFP number, I estimated a roughly 23-fold variation in the number of cadherins per cell.

The exogenous cadherins altered cells' morphologies from those of wild-type CHO cells. Wild-type CHO cells are non-adherent, essentially isotropic, and round up in Petri-dish culture. Most CHO-EC7 cells adhere to each other, elongate, spread on substrates and form cell clusters (Fig. 2.2).

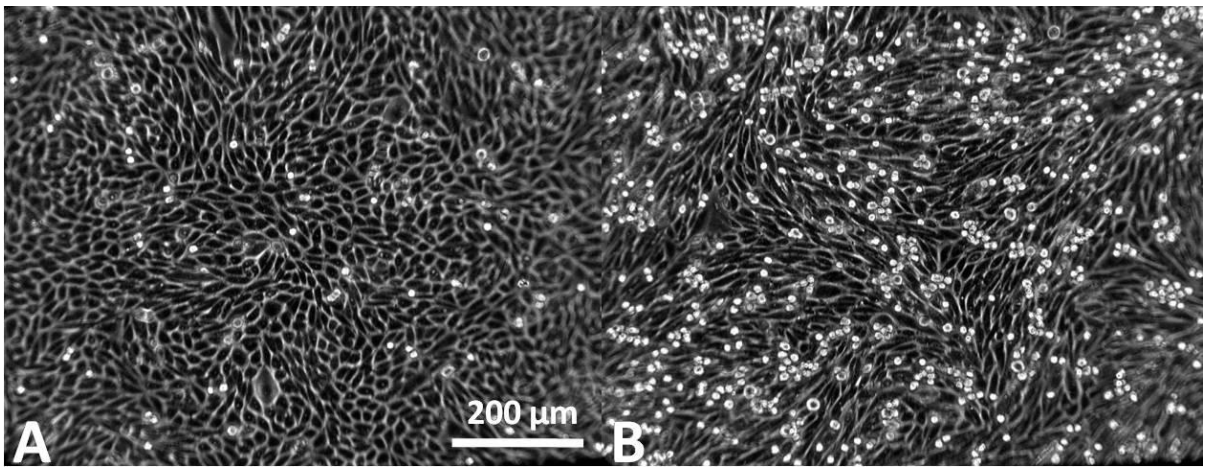

Figure 2.2: Wild-type CHO and transfected CHO-EC7 cells under confluent conditions. **A.** Wild-type CHO cells round up. **B.** CHO-EC7 cells stretch and adhere to each other. White round dots are cells detached from the Petri dish.

CHO 0 min
CHO 60 min
EC7 0 min
EC7 60 min
Ca2+ 0 mM
Ca2+ 0.1 mM
Ca2+ 1 mM
A1
A2
B1
B2
C1
C2
D1
D2
E1
E2
F1
F2
200 µm

Figure 2.3: Suspended wild-type CHO cells and transfected CHO-EC7 cells after TC-treatment for different concentrations of Ca^{2+}. Isolated wild-type CHO cells immediately after TC–treatment: **A1.** Without Ca^{2+}. **B1.** With 0.1 mM Ca^{2+}. **C1.** With 1 mM Ca^{2+}. Wild-type CHO cells do not form aggregates after 60 minutes in media: **A2.** Without Ca^{2+}. **B2.** With 0.1 mM Ca^{2+}. **C2.** With1 mM Ca^{2+}. Isolated CHO-EC7 cells immediately after TC-treatment: **D1.** Without Ca^{2+}. **E1.** With 0.1 mM Ca^{2+}. **F1.** With 1 mM Ca^{2+}. CHO-EC7 cells do not form aggregates after 60 minutes in media: **D2.** Without Ca^{2+}. **E2.** With 0.1 mM Ca^{2+}. **F2.** CHO-EC7 cells aggregate after 60 minutes in media with 1 mM Ca^{2+}.

After TC-treatment, neither wild-type (Figs. 2.3A1-2) nor transfected CHO-EC7 cells (Figs. 2.3D1-2) aggregated in Ca^{2+}-free medium over the first hour in stirred suspension, showing that they have little Ca^{2+}-independent cell-cell adhesion. Wild-type CHO cells do not aggregate in either normal (Figs. 2.3C1-2) or low-Ca^{2+} medium (Figs. 2.3B1-2). E-cadherin-GFP-expressing cells aggregate rapidly at normal Ca^{2+} concentrations (Figs. 2.3F1-2) and slowly in low Ca^{2+} medium (Figs. 2.3E1-2), confirming that cell adhesion is Ca^{2+}-dependent and cadherin-mediated.

In stirred suspensions, TE-treated E-cadherin-GFP-expressing cells take a few hours to aggregate, presumably due to the time they need to recover their surface cadherins after TE treatment. Wild-type cells do not aggregate after TE-treatment (Fig. 2.4) further confirming that all cell adhesion in this cell type results from E-cadherin-GFPs.

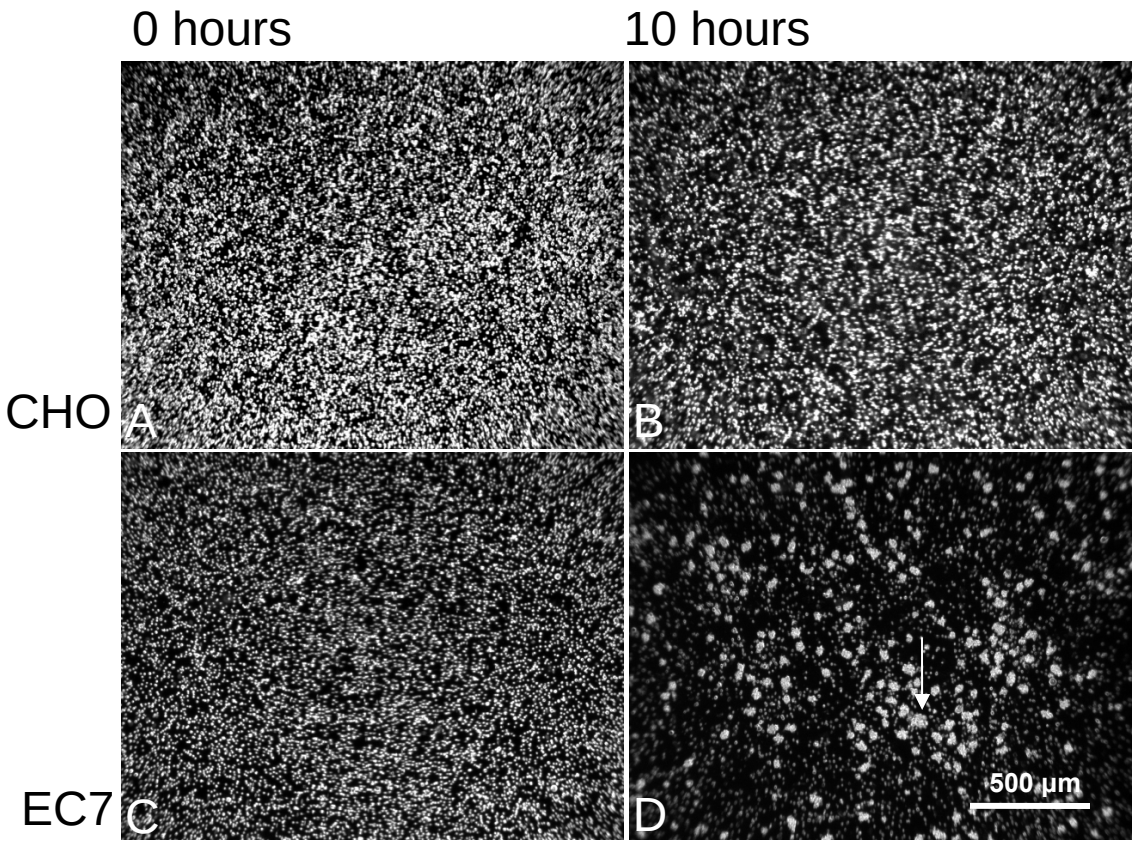

Figure 2.4: Suspended wild-type CHO cells and transfected CHO-EC7 cells after TE-treatment. A. Isolated wild-type CHO cells immediately after TE-treatment. **B.** Wild-type CHO cells do not form aggregates after 10 hours. **C.** Isolated CHO-EC7 cells immediately after TE-treatment. **D.** CHO-EC7 cells aggregate after 10 hours. The white arrow indicates one aggregate. All images to the same scale as that shown in D.

In two-dimensional cell culture, E-cadherin-GFP proteins do not localize evenly on the surface of CHO-EC7 cells, but form patches and cluster where cell-cell contacts form vertices, consistent with Nelson's results (Adams *et al.,* 1998). In three-dimensional aggregates E-cadherin-GFP proteins concentrate along cell-cell contact edges, not uniformly

across the contact surface (Fig. 2.5A). For a given number of cadherin molecules, this patchy distribution may enhance local cell-cell adhesion by increasing local cadherin concentrations. Cell morphologies in three-dimensional aggregates are similar to those in two-dimensional cultures. CHO-EC7 cells expressing E-cadherin-GFP at higher levels elongate and adhere to each other, while cells expressing lower levels are rounder, like wild-type CHO cells (Fig. 2.5B).

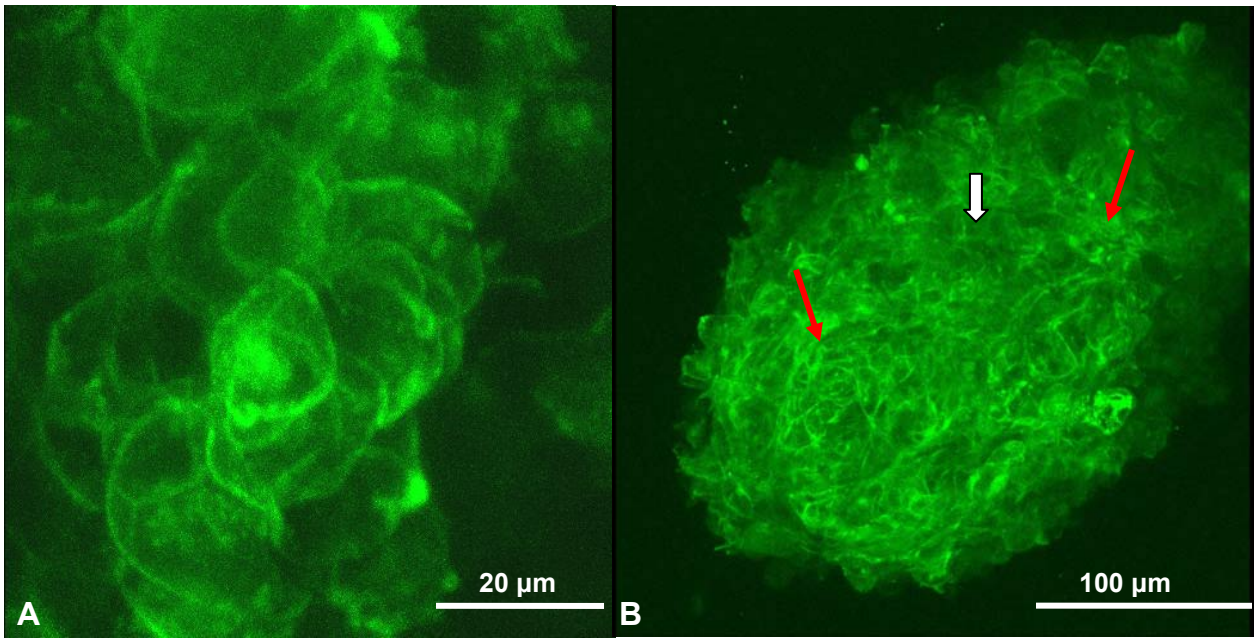

Figure 2.5: Cadherin distributions in CHO-EC7 cell aggregates. A. Three-dimensional reconstructed conventional confocal image of part of a three-dimensional cell aggregate. E-cadherin-GFP proteins accumulate at the edges of cell-cell contact surfaces. **B.** Three-dimensional reconstructed image of E-cadherin-GFP expression for a typical two-day-old cell aggregate. Cells with high expression levels (red arrows), and cells with low expression levels (white arrow) form homotypic clusters. Image contrast was enhanced using ImageJ.

I investigated sorting of three-dimensional aggregates with cells from the CHO-EC7 line. A confocal three-dimensional projection of a middle cross section (Fig. 2.5B) of a typical cell aggregate shows that after two days of incubation of an originally randomly-mixed cell aggregate, cells expressing E-cadherin-GFP at high levels (red arrows) or low levels (white arrow) cluster into homotypic domains (Fig. 2.5B).

If sorting occurs in my aggregates, I would expect the fluorescence intensity across the aggregate to be initially random. As cells aggregate into homotypic patches, I would expect to see uniform patches of different intensity levels, surrounded by random signal. Finally, in the fully-sorted aggregate, I would expect to see maximal fluorescence intensity near the center of the aggregate and a monotonic decrease in intensity from this maximum to the periphery of the aggregate.

Unfortunately, cadherins are expressed mostly on the cell membrane, causing big variations in the fluorescence intensity across aggregate cross-sections and complicating measurements of the degree of sorting within each aggregate. To determine whether the intensity variations I observe are statistically significant, I subdivided each $N \times N$-pixel image (N = 512, 1024, or 2048) into $2^k \times 2^k$ (k = 0, 1, 2, 3, …9) subregions. Choosing k = 5 gives a subregion of size 10×10 μm^2 (about the size of a biological cell) and has, to my eye, the most significant variations across the image. However, the variation in the average intensity between subregions across whole images is not statistically significant at this scale.

I next used the transform,

$$\text{Transformed Intensity of subregion}(i,j) = \left(\frac{\text{Mean Intensity of Subregion}(i,j)}{\text{Mean Intensity of the Whole Image}}\right)^{6}, \quad (2.1)$$

to enhance the contrast between subregions. This transform amplifies intensities which are bigger than the Mean Intensity of the Whole Image (*MIWI*) and reduces intensities which are weaker that the MIWI, making the difference in intensity among subregions more obvious. I further visualized the standard deviation in fluorescence for each subregion using this enhancement transform. I expected a concentric distribution of fluorescent intensity according to the DAH; however, I found no obvious concentric areas in most images (Fig. 2.6).

Contrast-enhanced visualization of the mean fluorescence intensity (Fig. 2.6) and standard-deviation measurements for each block of each image showed that cells with high cadherin expression (brown and red) and low cadherin expression (blue) did cluster into homotypic domains. The standard deviation of the fluorescent intensity in each subregion was uniform over the whole image. Two-day aggregates (Figs. 2.6A-C) have many small clusters of cells with similar cadherin-expression levels. Three-day aggregates (Figs. 2.6D-F) have larger clusters of cells with similar cadherin-expression levels. Six-day aggregates (Figs. 2.6G-I) have large clusters of high-cadherin cells near the center of the aggregate with some high-cadherin cells at the periphery. The figures suggest that cells first form small local clusters, which coalesce to form a larger cluster with high cadherin expression near the center of the aggregate and cadherin levels decreasing from the center to the periphery of the aggregate.

Two-Day

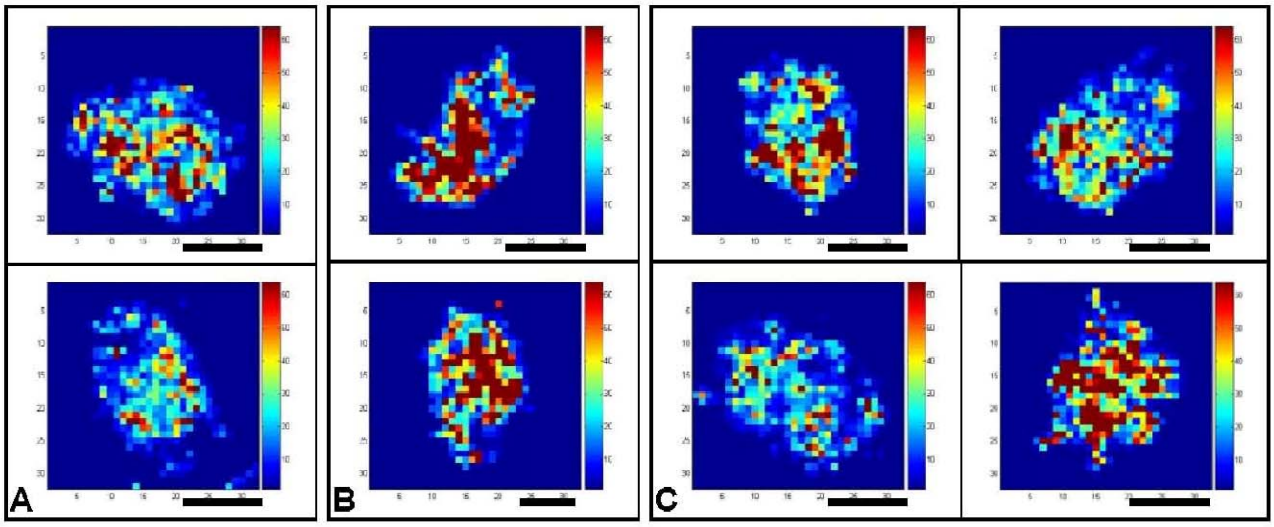

Three-Day

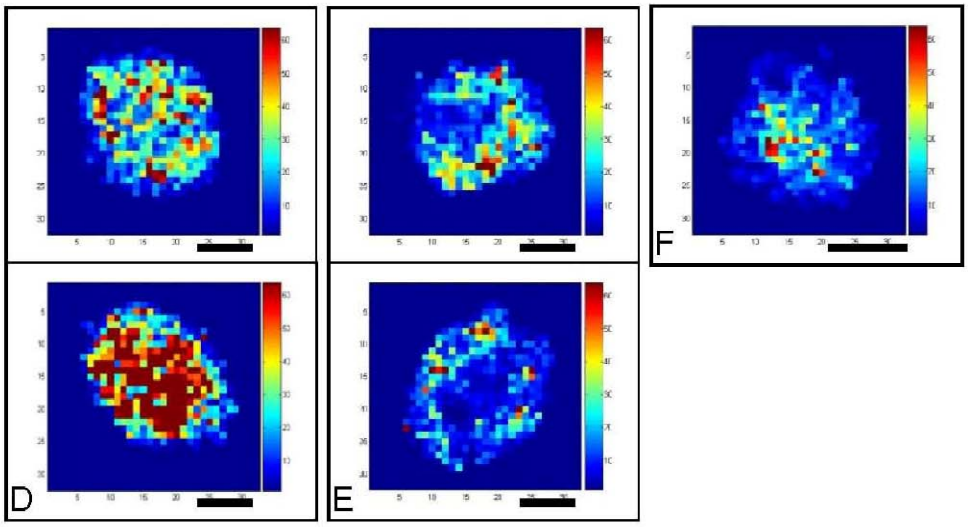

Six-Day

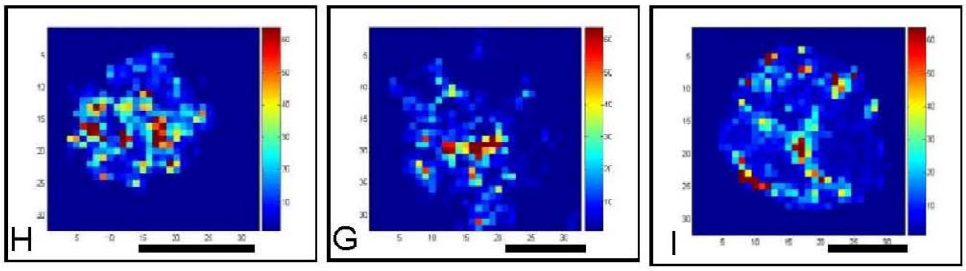

Figure 2.6: Distribution changes in E-cadherin-GFP expression levels in CHO-EC7 cell aggregates. Each image is an optical cross section of an aggregate, divided into 32 × 32 subregions. Intensity is averaged over each subregion and contrast is enhanced. The color indicates the enhanced mean intensity in each subregion (Red corresponds to high intensity, blue to low). **A-C.** Two-day aggregates. **D-F.** Three-day aggregates. **G-I.** Six-day aggregates. Each letter (A-I) corresponds to a single aggregate. Multiple images for a single letter are differently-oriented cross-sections of the same aggregate. Scale bars are 100 μm.

To clarify the distribution of cadherin expression within aggregates, I converted the images in Fig. 2.6 into intensity contour plots (Fig. 2.7). Most aggregates have multiple clusters of high or low cadherin expression, though Fig. 2.7F shows a clear decrease in the level of cadherin expression from the center to the periphery. Thus, I observed partial sorting in all aggregates, but complete sorting only in the aggregate in Fig. 2.7F.

I attempted to quantify homotypic clustering and centralization of high-cadherin cells within aggregates. To check for a decrease in cadherin expression from a high expression cluster (not necessarily at the exact center of the aggregate) towards the periphery, I analyzed the intensity distribution as follows: (1) I subdivided each cross-section into four concentric subregions with equal areas, excluding the edge of the aggregate where the spherical aggregate shape makes image-intensity measurements unreliable. I manually defined the subregions to obtain the highest-possible mean intensities for each subregion. Fig. 2.8 shows the subdivisions for all aggregates. (2) I then calculated the mean fluorescence intensity of each subregion for all the aggregates (Fig. 2.9).

Two-Day

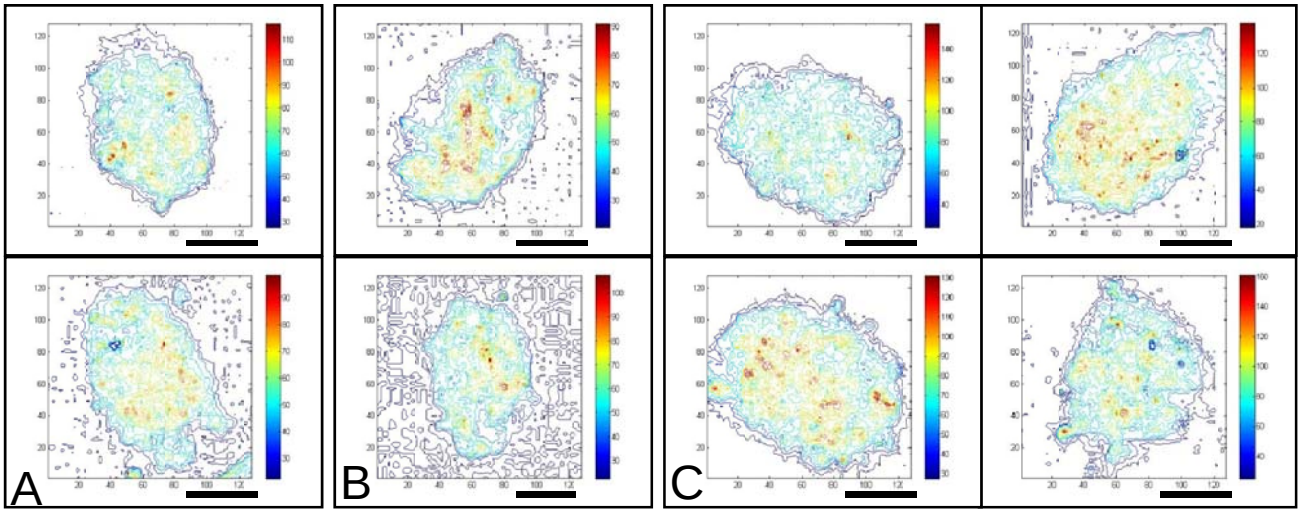

Three-Day

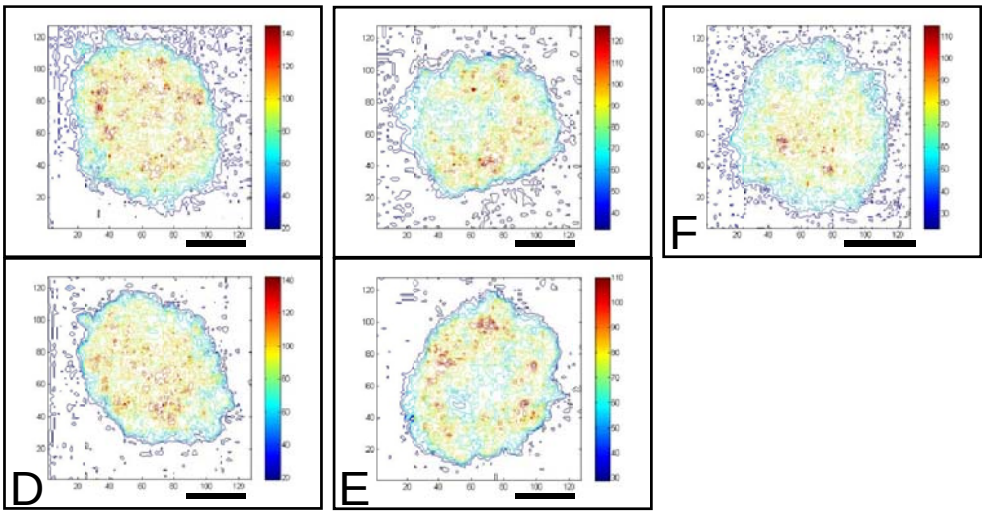

Six-Day

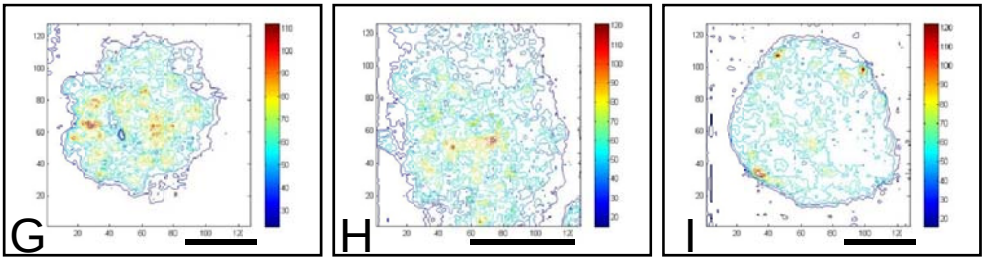

Figure 2.7: Cadherin-expression contour plots corresponding to Fig. 2.6. A-I. Images are contour plots of the corresponding intensity plots in Fig. 2.6.

To test whether the intensities of different subregions differed significantly, I used a paired-sample t-test to compare regions (Table 2.1).

Comparing increasingly peripheral subregions to the next-most central region, *i.e.*, CT_2 *vs.* CT_1, CT_3 *vs.* CT_2 and CT_4 *vs.* CT_3, the mean intensity differed significantly (one-tailed $P < 0.01$, P(two-day) < 0.01). Since I used the t-test three times to test one hypothesis, I used the Bonferroni correction to satisfy the $\alpha = 0.05$ criterion. While the relative average intensity decreased in more peripheral subregions, for three-day and six-day aggregates, the P values for CT_2 *vs.* CT_3, and CT_3 *vs.* CT_4 were not significant, possibly due to the small sample size ($n = 5$ and $n = 2$). In addition, the amplitude of the decrease from center to periphery did not increase with time as I would have expected for complete sorting. Thus, I am left with three possibilities: (1) Most aggregates did not sort completely. (2) Sorting was complete by day two. (3) My measurements were not sufficiently accurate to determine whether complete sorting occurred or not in most aggregates.

Two-Day

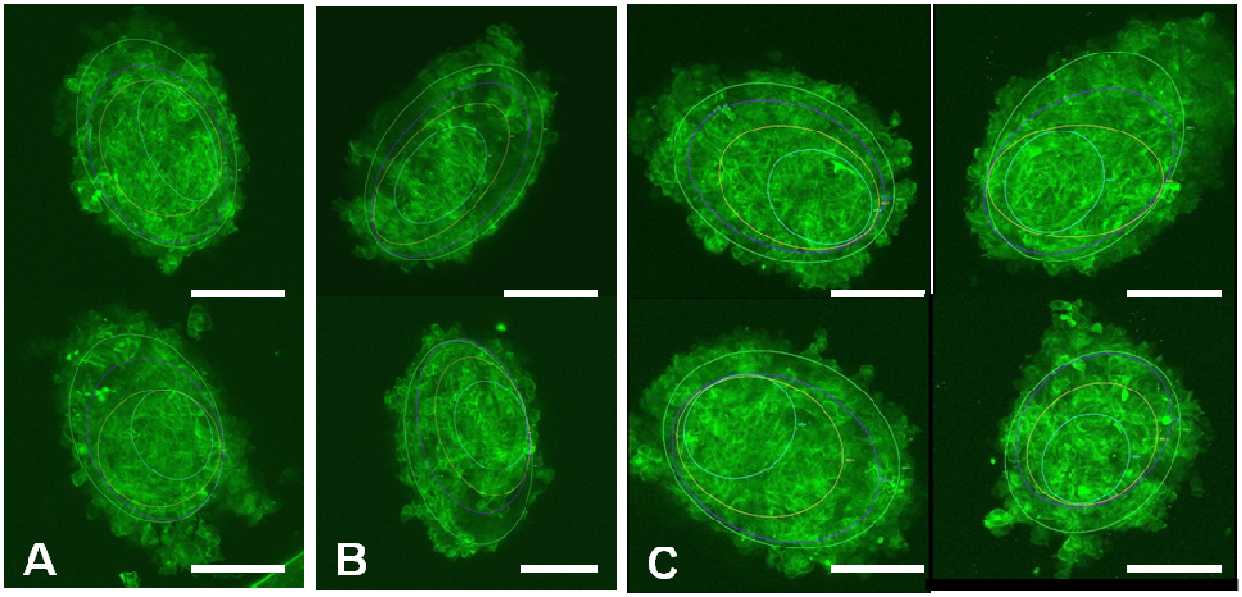

Three-Day

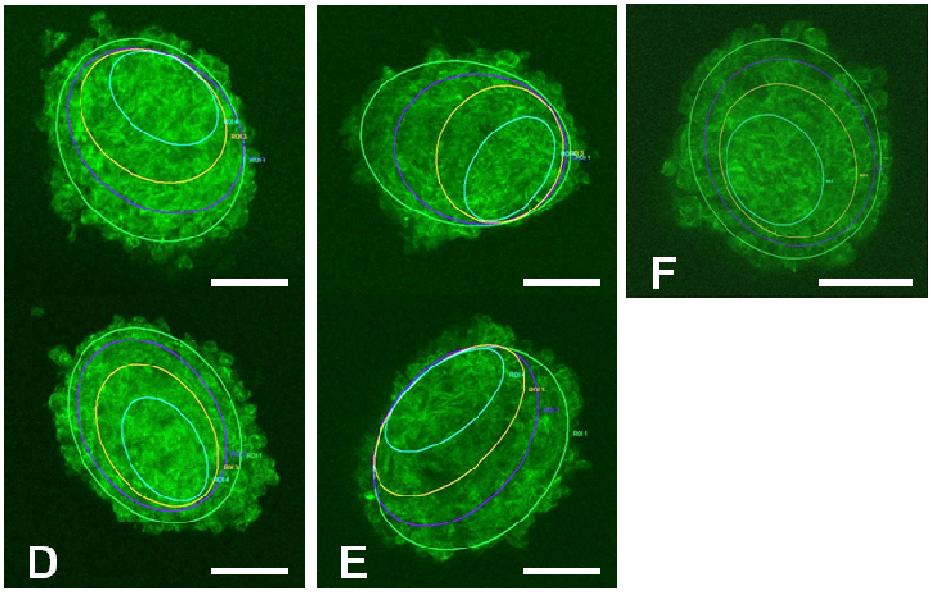

Six-Day

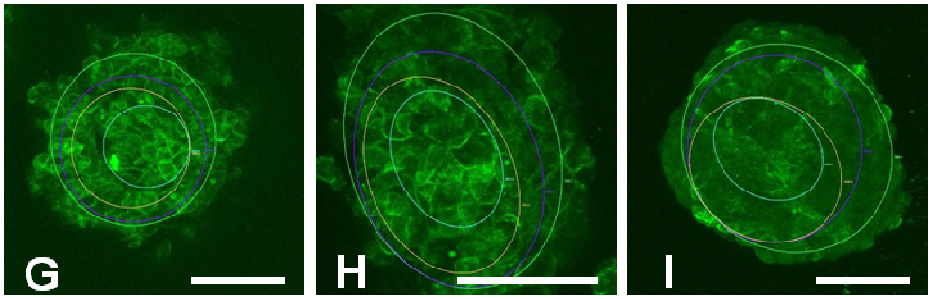

Figure 2.8: Subdivision of cross-sections of aggregates into four concentric subregions. A-I. Subdivision of the cross sections of aggregates into four equal-area subregions. Images correspond to those in Fig. 2.6.

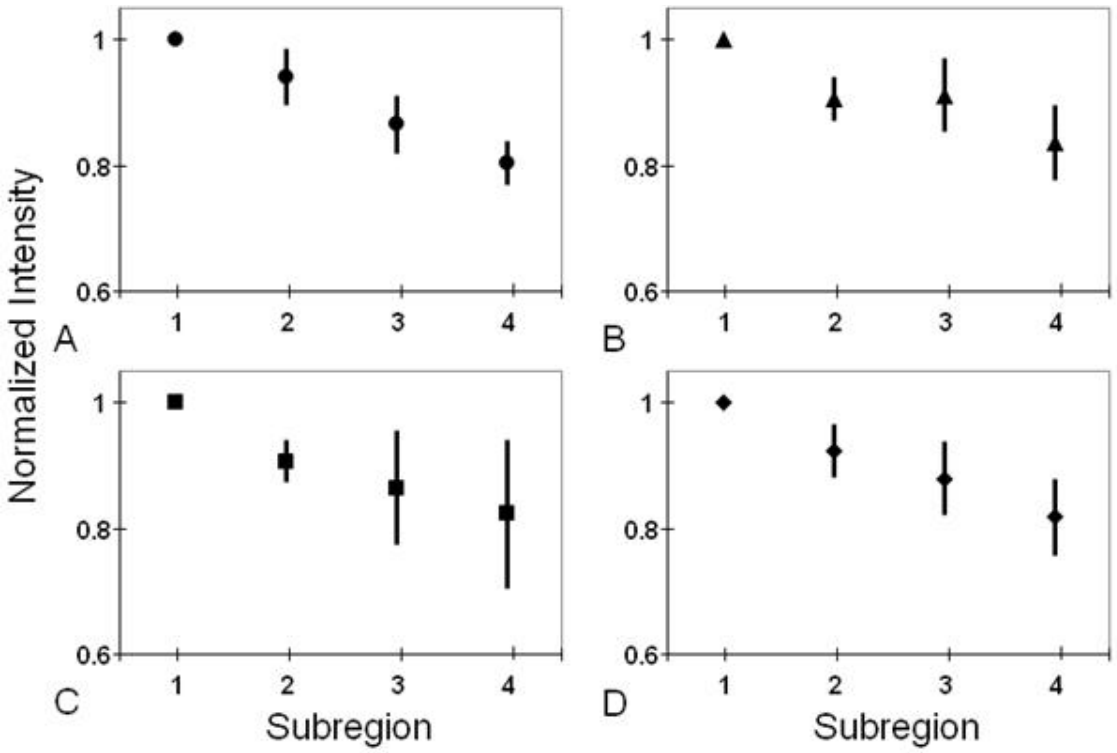

Figure 2.9: Mean fluorescence intensity with standard deviations for each subregion for individual aggregates. X-axis: subregions 1 to 4, center to periphery. **Y-axis**: Normalized intensity. **A.** Two-day aggregates. **B.** Three-day aggregates. **C.** Six-day aggregates. **D.** All aggregates. All data are normalized so that the intensity of the central region is one.

Table 2.1: Cadherin-expression variations by subregion and time during sorting. The mean and standard deviation of fluorescent intensity per pixel relative to subregion CT_1, for each subregion, averaged over all orientations of all aggregates for a given day, and the significance (P value) of their difference according to the paired-sample student t-test.

Subregion		2	3	4	
Day	*n*	$\langle I_2 \rangle \pm SD_2$	$\langle I_3 \rangle \pm SD_3$	$\langle I_4 \rangle \pm SD_4$	Significance of deviation from the paired sample t-test*
2	8	0.94 ± 0.04	0.86 ± 0.05	0.80 ± 0.03	$P_{12}, P_{23}, P_{34} < 0.01$
3	5	0.91 ± 0.04	0.91 ± 0.06	0.84 ± 0.06	$P_{12} < 0.01$; $P_{23} = 1.20$; $P_{34} = 0.06$
6	3	0.91 ± 0.03	0.86 ± 0.09	0.82 ± 0.12	$P_{12} = 0.06$; $P_{23} = 0.54$; $P_{34} = 0.18$

2.4 Discussion

In spite of the large variations in clustering of cells according to their cadherin levels, my experiments demonstrate that monotonic cadherin expression gradients characteristic of complete cell sorting can form in at least some aggregates of CHO-EC7 cells within three days (Figs. 2.6F, 2.7F and 2.8F), suggesting that the variation in expression of a single type of cell adhesion molecule can lead to an equilibrium cell-sorting configuration, in agreement with the computer simulations I present in Chapter Three. Real-time tracking of cells in aggregates would further validate my theory. However, I could not track cadherin expression

in an intact, living cell aggregate due to optical attenuation of the fluorescence signal. Because sectioning the aggregate destroys it, I had to use different aggregates for each image, rather than producing a time series of a single aggregate. These experiments show the complexity and hence difficulty of a definitive experimental study of real-time clustering in response to a large range of cadherin levels.

CHAPTER THREE

COMPUTER SIMULATIONS OF CELL SORTING DUE TO DIFFERENTIAL ADHESION

Abstract

Computer simulations of cell sorting due to adhesion have primarily studied the interactions of cells expressing a few discrete levels of cadherins, while during development cells often express continuously-variable levels of cadherins. In this chapter, I first construct three frameworks to link the molecular binding force to intercellular adhesion and interfacial tension. I then use the Glazier-Graner-Hogeweg model to investigate how variations in the distribution of numbers of cadherins per cell and in the choice of binding model affect sorting. Continuous variation of a single type of cadherin molecule decreases the sorting rate compared to the rate for two levels. The speed of sorting depends strongly on the interfacial tension, which depends both on the maximum difference in number of cadherins per cell and on the binding model.

3.1 Introduction

The *Differential Adhesion Hypothesis* (*DAH*) (Steinberg 1963; Steinberg and Wiseman, 1972; Steinberg and Takeichi, 1994; Foty and Steinberg, 2005) leaves open many questions, including:

1) How do molecular interactions between cadherins determine the strength of intercellular adhesion (Gumbiner 2005)?
2) What is the kinetics of cadherin rearrangement within the cell membrane?
3) How does intracellular cortical tension relate to adhesion between cells and how do these two effects couple during cell sorting?

The relation between forces at the molecular level (pairs of cadherins), cell level (cell-cell adhesion) and tissue level (surface tension) is complex. This chapter proposes a simple framework to illustrate how homotypic cadherin binding at the molecular level produces intercellular adhesion and eventually determines cell sorting at the tissue level. I neglect complex spatial and temporal changes in cadherin behavior, assuming that cadherin distributions are uniform and constant on the cell membrane and that adhesion-strength per molecular bond is also time-independent (*i.e.,* I assume no conformational changes of molecular structure). Therefore, I am able to explore how the sorting configuration and rate depend on a few essential parameters in the model.

3.2 Methods

3.2.1 Reaction-Kinetics Models of E-Cadherin Binding

The nature of cadherin-cadherin binding affects the way cell-cell adhesion energy depends on cells' cadherin densities, and thus the correct models to use in simulations of cell sorting. Models of cadherin binding include the *linear-zipper* model based on experiments on N-cadherin (Shapiro *et al.,* 1995; Sivasankar *et al.,* 1999; Chappuis-Flament *et al.,* 2001; Zhu *et al.,* 2003), the *cis-dimer* model based on experiments on E-cadherin (Pertz *et al.,* 1999), and the *trans-homophilic-bond* model based on experiments on C-cadherin (Boggon *et al.,* 2002). Since mutagenesis studies do not support the linear-zipper model (Gumbiner, 2005), I use the cis-dimer and trans-homophilic-bond models to relate the numbers of cadherins per cell to the cell-cell adhesion energy.

The cis-dimer model (Perts *et al.,* 1999) assumes that cis-dimers first form on the surfaces of individual cells and that two dimers on apposing cells then bind together to form homophilic tetramers.

Dimerization of monomers (A and A or B and B) on individual cells' surfaces to form dimers X and Y has the form:

$$A + A = X; B + B = Y. \tag{3.1}$$

Similarly, when trans-tetramers XY form between dimers (X and Y) on two apposing cells, the reaction has the form:

$$X + Y = XY. \tag{3.2}$$

I assume that the cadherin concentrations on the cells' surfaces are constant and that I can apply the Law of Mass Action. Dimerization and tetramerization quickly equilibrate if K_D and K_T, the *equilibrium dimerization* and *tetramerization dissociation constants* are large and the cadherin concentrations $C_A = N_A/S_A h$ and $C_B = N_B/S_B h$ are lower than the dissociation constants (Chen *et al.,* 2005). Here S_A and S_B are the surface areas of the cells, and h is the amplitude of cadherin fluctuations normal to the cells' surfaces. In this case, the total number of tetramers is less than the number of dimers, which in turn is less than the number of monomers. The equilibrium concentration of tetramers is approximately:

$$[XY] = C_A^2 C_B^2 / K_D^2 C_T = k_T N_A^2 N_B^2, \tag{3.3}$$

where $k_T \equiv 1/K_D^2 K_T (S_A S_B h^2)^2$ is the *tetramer effective equilibrium constant*.

According to the trans-homophilic bond model, cadherins bind individually between cells, so the concentration of bound pairs is:

$$[XY] = C_A C_B / K_D = k_D N_A N_B, \tag{3.3'}$$

where $k_D \equiv 1/K_D S_A S_B h^2$ is the *dimer effective equilibrium constant*.

In the case of strong clustering of cadherins, or a large difference in the number of molecules per cell, the concentration of bound cadherin pairs is:

$$[XY] = \text{Minimum}\{C_A, C_B\} = k_M \text{Minimum}\{N_A, N_B\}, \tag{3.3''}$$

where $k_M \equiv 1/(S_A|S_B)h$ is the *effective equilibrium constant*. The *S* included in the equation is that corresponding to the smaller of N_A or N_B.

The intercellular *adhesion energy density*, ΔG, due to cadherin binding is (Chen *et al.,* 2005):

$$\Delta G = [XY] \times \Delta g, \tag{3.4}$$

where Δg is the cadherin-cadherin-binding free-energy per cadherin bond. Bond formation releases energy, so $\Delta g < 0$.

The *intercellular adhesion-energy density*, $J(N_A, N_B)$, on cell-cell binding is:

$$J(N_A, N_B) = [XY] \times \Delta g + c, \tag{3.5}$$

where c is the *energy density due to nonspecific binding*.

The *interfacial-tension density* over the contact area between two cells expressing different numbers of cadherin is (Graner and Glazier, 1992; Glazier and Graner, 1993):

$$\gamma_{A,B} = [J(N_A, N_A) + J(N_B, N_B)]/2 - J(N_A, N_B) = \big(([XX] + [YY])/2 - [XY]\big)\Delta g, \tag{3.6}$$

For the cis-dimer model, according to Eq. (3.3), the interfacial-tension density is:

$$\gamma_{cis} = k_T(N_A^2 - N_B^2)^2 \Delta g/2 = k_T(N_A - N_B)^2(N_A + N_B)^2 \Delta g/2. \tag{3.7}$$

For the trans-homophilic-bond model, according to Eq. (3.3′), the interfacial-tension density is:

$$\gamma_{trans} = k_D(N_A - N_B)^2 \Delta g/2. \tag{3.7′}$$

For the saturation model, according to Eq. (3.3″), the interfacial-tension density is:

$$\gamma_{sat} = k_M(N_A - N_B)\Delta g/2, \tag{3.7″}$$

where $N_A > N_B$.

3.2.2 Glazier-Graner-Hogeweg Simulations of Cell Sorting

To simulate cell sorting due to cell-cell adhesion, I used the *Glazier-Graner-Hogeweg* model (*GGH*) (also known as the *Cellular Potts Model*, *CPM*) (Graner and Glazier, 1992; Glazier and Graner, 1993). The GGH is a multi-cell, lattice-based model, which uses an *Effective Energy, H,* to describe the behavior of cells, for instance, due to cell-cell adhesion. GGH simulations agree quantitatively with simple cell-sorting and other experiments (Mombach and Glazier, 1996; Rieu *et al.,* 2000; Zajac *et al.,* 2000; Maree and Hogeweg, 2001; Zeng *et al.,* 2004; Dan *et al.,* 2005; Merks *et al.,* 2006; Glazier *et al.,* 2007; Poplawski *et al.,* 2007).

Cells in the GGH are extended domains of pixels (on a regular lattice, denoted $\vec{\imath}$), which share the same *cell index,* $\sigma(\vec{\imath})$. The Effective Energy, governs how the lattice evolves as cells attempt to displace other cells by extending their pseudopodia, according to a *modified Metropolis algorithm* (Metropolis *et al.,* 1953). At each step, I select a lattice site $\vec{\imath}'$ and change its index into the index of a neighboring lattice site $\vec{\imath}$ with probability:

$$P\big(\sigma(\vec{\imath}') \rightarrow \sigma(\vec{\imath})\big) = \{exp(-\Delta H/T), \Delta H > 0;\ 1, \Delta H \leq 0\}, \tag{3.8}$$

where ΔH is the energy gain from the change and T is the *intrinsic cell motility*, or *fluctuation temperature*. If the lattice has N pixels, I define one *Monte Carlo Step* (*MCS*) to be N displacement attempts.

For a two-dimensional simulation of an aggregate containing cells expressing varying levels of a single type of cadherin, I assume that: (1) The Effective Energy between cells is due to cell-cell adhesion. (2) The cells have fixed and identical target volumes, membrane areas,

and intrinsic motilities. (3) Cells do not grow, divide or die. (4) Cells are isotropic, so cadherins are uniformly distributed on the cell membrane and their concentration is constant. For these conditions, the Effective Energy is:

$$H = \sum_{\substack{\vec{\imath},\vec{\imath}' \\ \text{neighbors}}} \left\{J_0 + J\left(N\left(\sigma(\vec{\imath})\right), N'\left(\sigma'(\vec{\imath}')\right)\right)\left(1 - \delta\left(\sigma(\vec{\imath}), \sigma(\vec{\imath}')\right)\right)\right\} + \sum_{\sigma} \lambda(V(\sigma) - V_t)^2 , \tag{3.9}$$

where, J_0 is the energy per unit contact area between two cells without cadherin binding. Since such cells do not cohere, $J_0 > 0$. $J\left(N\left(\sigma(\vec{\imath})\right), N'\left(\sigma'(\vec{\imath}')\right)\right)$ is the adhesion-energy per unit contact area between cells expressing N and N' adhesion molecules. Since forming cadherin bonds decreases the effective energy, $J\left(N\left(\sigma(\vec{\imath})\right), N'\left(\sigma'(\vec{\imath}')\right)\right) < 0$. Sums go up to fourth neighbors on a square lattice. λ, $V(\sigma)$ and V_t are the volume elasticity, actual volume and target volume of cell σ, respectively. The Kroeneker delta, $\delta\left(\sigma(\vec{\imath}), \sigma(\vec{\imath}')\right) = \{1, \text{if } \sigma(\vec{\imath}) = \sigma(\vec{\imath}');\ 0, \text{if } \sigma(\vec{\imath}) \neq \sigma(\vec{\imath}')\}$.

Each cell expresses a specific number of cadherins. The cell-cell adhesion energy relates to N and N' according to Eq. (3.3), (3.3′) or (3.3′′) and Eq. (3.5). Since I can rescale the energy by the intrinsic cell motility, I am free to pick the energy scale and set $\Delta g = -1$.

In an ideal, fully-sorted configuration, cells expressing high levels of cadherins will cluster together and round up into a solid sphere, surrounded by cells expressing low levels of cadherins. The *heterotypic boundary length* (*HBL*, the total contact length between cells with different cadherin levels) between two types of cells is minimized for complete sorting. The

HBL is a convenient monitor of the progress of cell sorting. For cells expressing two levels of cadherin, the HBL is just:

$$L_h = \sum_{\substack{\vec{\imath},\vec{\imath}' \\ \text{neighbors}}} \left\{1 - \delta\left(\text{type}\left(\sigma(\vec{\imath})\right), \text{type}\left(\sigma(\vec{\imath}')\right)\right)\right\}. \tag{3.10}$$

If cells express multiple cadherin levels, L_w, the heterotypic boundary length weighted by the energy differences between neighboring cells is a better metric for cell sorting. This *weighted heterotypic boundary length* (*WHBL*) is simply the total *interfacial tension* (Eq. (3.7), (3.7′) or (3.7′′)).

For the cis-dimer model:

$$L_w = k_T \sum_{\substack{\vec{\imath},\vec{\imath}' \\ \text{neighbors}}} \left(N\left(\sigma(\vec{\imath})\right)^2 - N'\left(\sigma(\vec{\imath}')\right)^2\right)^2 \left\{1 - \delta\left(\sigma(\vec{\imath}), \sigma(\vec{\imath}')\right)\right\} \frac{\Delta g}{2}. \tag{3.10′}$$

For the trans-homophilic-bond model:

$$L_w = k_D \sum_{\substack{\vec{\imath},\vec{\imath}' \\ \text{neighbors}}} \left(N\left(\sigma(\vec{\imath})\right) - N'\left(\sigma(\vec{\imath}')\right)\right)^2 \left\{1 - \delta\left(\sigma(\vec{\imath}), \sigma(\vec{\imath}')\right)\right\} \frac{\Delta g}{2}. \tag{3.10″}$$

For the saturation model:

$$L_w = k_M \sum_{\substack{\vec{\imath},\vec{\imath}' \\ \text{neighbors}}} \left(N\left(\sigma(\vec{\imath})\right) - N'\left(\sigma(\vec{\imath}')\right)\right) \left\{1 - \delta\left(\sigma(\vec{\imath}), \sigma(\vec{\imath}')\right)\right\} \frac{\Delta g}{2}. \tag{3.10‴}$$

Different aggregates may have different maximum (initial) and minimum HBLs or WHBLs. To compare sorting in different aggregates, I normalize the HBL and WHBL using the transformation:

$$l_N(t) = \frac{L(t) - L_{\text{Min}}}{L_{\text{Max}} - L_{\text{Min}}}, \tag{3.11}$$

where, $L_{\mathrm{Max}} = \mathrm{Maximum}\big(L(t)\big)$, $L_{\mathrm{Min}} = L_k$ or L_{sm} and $L(t)$ is the HBL or WHBL at time *t*. $L_k = \mathrm{Minimum}\big(L(t)\big)$ is the minimum value of HBL or WHBL over the estimated simulation duration of 1,000,000 MCS. L_{sm} is the theoretical minimum HBL or WHBL for a fully-sorted aggregate. The *sorting relaxation time*, τ, is the time at which the aggregate reaches its typical fully-sorted configuration. τ is defined *via* the relation:

$$l_N(\tau) = \frac{l_N(0)}{e}. \tag{3.12}$$

The *sorting rate*, R_s, is the inverse of the sorting relaxation time:

$$R_s = \frac{1}{\tau}. \tag{3.13}$$

3.2.3 Simulation Implementation

I implemented my simulations using the open-source software package CompuCell3D (downloadable from https://simtk.org/home/compucell3d and http://compucell3d.org/) which allows rapid translation of biological models into simulations using a combination of CC3DML and Python scripting. This framework allows a compact description of models and hence their publication and validation. I provide my simulation code in Appendix 7.F.

All my simulations for cell sorting use aggregates of 305 cells, close to the size of the aggregates I studied experimentally. Each cell has a 25-pixel target volume, which sets the lattice length scale to approximately 2 microns per pixel. I begin with a circular-disk aggregate with cells randomly assigned cadherin expression numbers, with each allowed

number having equal probability. Each simulation uses $T = 20$ and runs for 1,000,000 MCS, to allow for complete sorting for continuous variation of cadherin expression over the range [1, 23]. I set $\lambda = 25$, which allows patterns to evolve reasonably fast without large cell-volume or surface-area fluctuations. Changing λ around this value does not greatly affect the relaxation of cells' shapes and positions. I further set $J_0 = 16$ for all simulations. For different cadherin binding models and for the cadherin expression range [1, 23], I choose the values of k_T, k_D and k_M (according to Eqs. (3), (3′) and (3′′)) so that cells do not 'freeze' or 'melt'.

3.3 Results

I first investigated sorting completeness for the trans-homophilic-bond model (Eq. (3.3′), $k_D = 0.02$) as I moved from two levels of cadherin expression towards a continuous distribution of levels (two, three, five, nine and continuous levels) with the same range of cadherin numbers, $[N_{min} = 1, N_{max} = 23]$. The same range of cadherin expression numbers provides the same range of adhesion energies, independent of the number of levels.

Figs. 3.1A-E show final aggregates for cells expressing discrete or continuous levels of cadherins. Cells with higher expression (dark/red color) assume more central positions, while cells with lower expression (light/blue) move to the periphery. For multiple discrete levels, cells follow a sorting hierarchy (Steinberg and Wiseman, 1972); each layer of cells has a given expression number and surrounds the layer of cells with the next-higher level. For

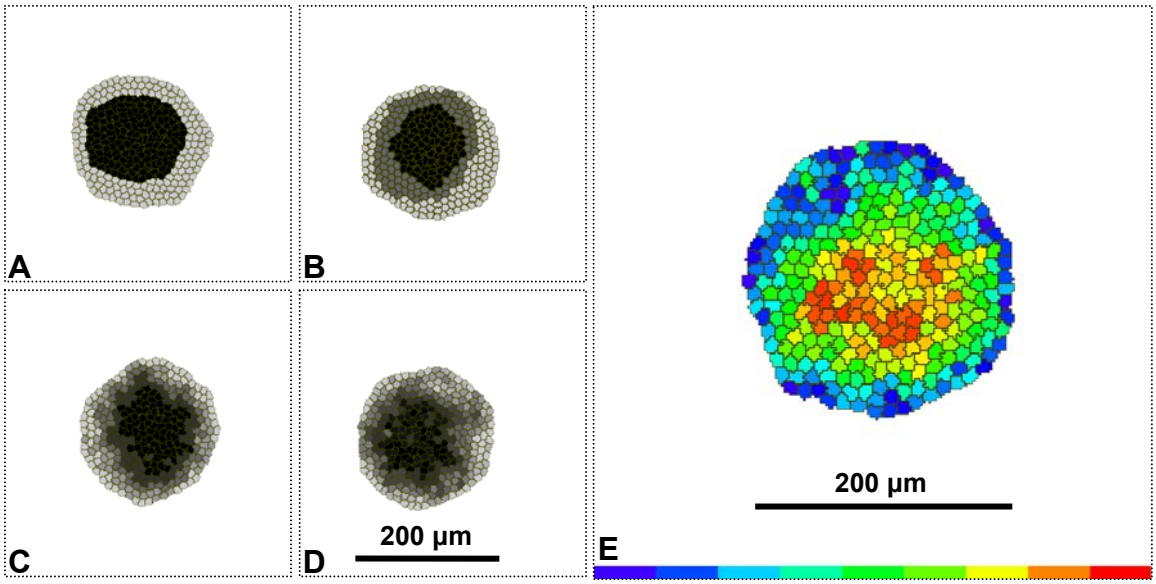

Figure 3.1: **Typical simulated sorting configurations for aggregates of cells for the trans-homophilic-bond model.** All images shown at time t = 999,000 MCS. In A-D, the gray scale represents cadherin-expression levels. The darkest color (gray level=0) represents the highest cadherin-expression level. The lightest color (gray level=200) represents the lowest cadherin-expression level. The cell culture medium is white (gray level=255). In E, HSV colors represent expression levels, $(H = (1 - (N - N_{min})/(N_{max} - N_{min}))255, S = 255, V = 255)$, where N is the cadherin-expression level, and N_{min} and N_{max} are the minimum and maximum cadherin-expression levels, respectively. **Red** ($H = 0$) is the highest expression level, **blue** ($H = 255$) the lowest expression level. The cell culture medium is white. Sorting for: **A.** Two levels. **B.** Three levels. **C.** Five levels. **D.** Nine levels. **E.** Continuous levels. Cadherin expression ranges from $N_{min} = 1$ to $N_{max} = 23$. In all simulations, $T = 20$ and $\lambda = 25$.

continuous levels (Fig. 3.1E), expression numbers decrease continuously from the center to the periphery of the aggregate.

I investigated the time evolution of the Effective Energy and HBL/WHBL for the trans-homophilic-bond model, in three cases:

1) Cells with different numbers of levels of cadherin expression, but the same range between maximum and minimum expression number.
2) Cells with different ranges between maximum and minimum expression number but with the same number of levels.
3) Cells with different motilities, but with the same cadherin levels.

I also studied:

4) Cells with different cadherin binding models, but the same range between maximum and minimum expression number for two, five, nine and continuous levels.

Fig. 3.2A shows the time evolution of the Effective Energy for cell aggregates with cells expressing two, three, five, nine, and continuous cadherin levels in the range [1, 23] using the trans-homophilic-bond model (Eq. (3.3′), $k_{\mathrm{D}} = 0.02$). Figs. 3.2B and 3.2C illustrate the time evolution of the normalized WHBL for cell aggregates in Fig. 3.2A, setting $L_{min} = L_k$ and $L_{min} = L_{sm}$, respectively. Aggregates with two or three levels sort quickly, while aggregates with more levels take more time to sort (Fig. 3.2D).

Fig. 3.3A shows the time evolution of the Effective Energy for aggregates with two cadherin levels but different expression ranges: [1, 12], [1, 14.75], [1, 17.50], [1, 20.25], [1, 23], [12,

23], and [19.62, 23]. Figs. 3.3B and 3.3C show the time evolution of the normalized WHBL for the same aggregates, using $L_{min} = L_k$ and $L_{min} = L_{sm}$, respectively. Sorting is quickest (τ = 14,040 MCS) for aggregates with the widest cadherin expression range [1, 23]. Sorting is slowest (no complete sorting, $\tau = \infty$) for aggregates with the smallest expression range [19.62, 23].

According to the theory of liquid phase separation, the sorting rate is proportional to the interfacial tension divided by the viscosity, η (Frenkel, 1945). This relationship should hold for cell sorting (Beysens *et al.,* 2000). Fig. 3.3D plots the sorting relaxation time against the interfacial tension (Eq. (3.7′)) for the aggregates in Fig. 3.4A. I fitted to a power law of form $\tau = a\gamma^{-b}$ to obtain *a* and *b* values. The relationship between τ and the interfacial tension γ is:

$$\tau = 3 \times 10^6 \gamma^{-2.5} = 3 \times 10^6 [k(N_{\mathrm{A}} - N_{\mathrm{B}})^2]^{-2.5}, \tag{3.14}$$

for $L_{min} = L_{sm}$, and:

$$\tau = 6.5 \times 10^5 \gamma^{-2.1} = 6.5 \times 10^5 [k(N_{\mathrm{A}} - N_{\mathrm{B}})^2]^{-2.1}, \tag{3.15}$$

for $L_{\mathrm{min}} = L_{\mathrm{k}}$. For $L_{min} = L_{sm}$, $R^2 = 0.89$, and for $L_{min} = L_k$, $R^2 = 0.98$. The coefficient of determination R^2 is defined to be: $R^2 \equiv \frac{\Sigma y_i^2 - \Sigma\left(y_i - a x_i^b\right)^2}{\Sigma y_i^2}$, where (x_i, y_i) is a sample point and ax_i^b is the fitting curve. R^2 can range from 0 for a bad fit to 1 for a perfect fit. Thus, the sorting relaxation time and interfacial tension obey an approximate power law (with exponent $b \sim -2$).

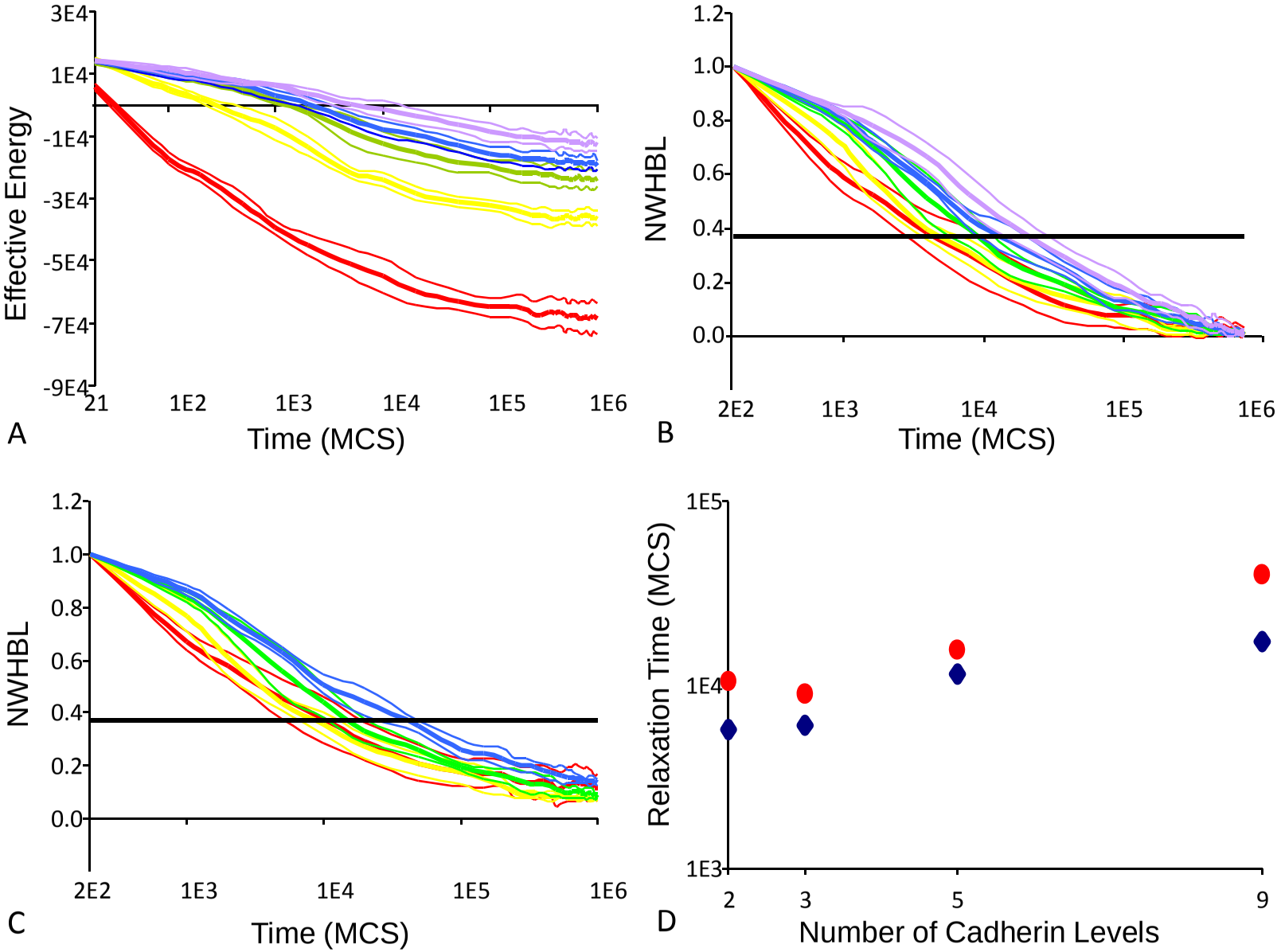
3E4
1E4
-1E4
-3E4
-5E4
-7E4
-9E4
Effective Energy
21
1E2
1E3
1E4
1E5
1E6
Time (MCS)
A
1.2
1.0
0.8
0.6
0.4
0.2
0.0
NWHBL
2E2
1E3
1E4
1E5
1E6
Time (MCS)
B
NWHBL
Time (MCS)
C
1E5
1E4
1E3
Relaxation Time (MCS)
2
3
5
9
Number of Cadherin Levels
D

Figure 3.2: Time evolution of the Effective Energies and Normalized (Weighted) Heterotypic Boundary Lengths for aggregates with differing numbers of cadherin levels for the trans-homophilic-bond model. In A-C: **Red**, two levels. **Yellow**, three levels. **Green**, five levels. **Blue**, nine levels. **Purple**, continuous levels. Thick lines show mean values. Thin lines show mean ± standard deviation. The heavy horizontal lines mark $1/e$. **A.** Time evolution of the Effective Energy. **B-C.** Time evolution of the Normalized Weighted Heterotypic Boundary Length for the simulations in A, with $L_{min} = L_k$ in **B** and $L_{min} = L_{sm}$ in **C**. **D.** Relation between relaxation time and number of levels. **Red dots** ($L_{min} = L_{sm}$). **Blue dots** ($L_{min} = L_k$).

I next compared the time evolution of the Effective Energy and normalized WHBL for different cadherin binding models with two, five, nine and continuous cadherin levels. I chose the effective equilibrium constants (k_T, k_D and k_M) so the cell-cell adhesion energies fell in the same range to exclude changes in cell sorting rates due to differences in these ranges. For two-level aggregates (Fig. 3.4A1), sorting times are equal, as I expected because Eqs. (3.7), (3.7′) and (3.7′′) give almost identical interfacial tensions. For aggregates with five and nine cadherin levels (Figs. 3.4B1 and 3.4C1), sorting is rapid for the saturation model, and slowest for the trans-homophilic-bond model. The average minimum WHBLs are largest for the saturation model, but are the same for both the cis-dimer model and the trans-homophilic-bond model. Since, the WHBL is actually the interfacial tension, the interfacial tension is the main factor which determines the sorting rate.

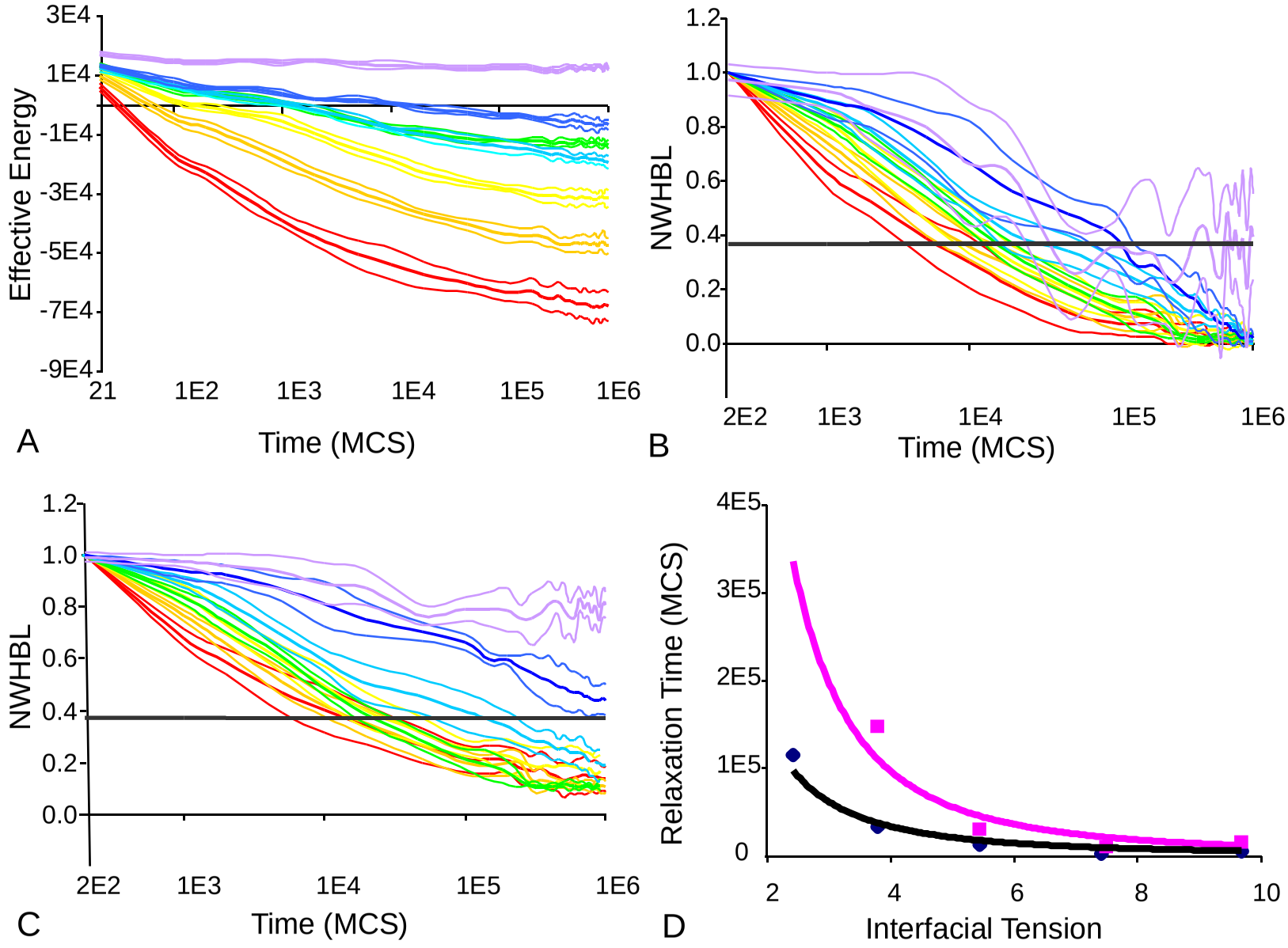
3E4
1E4
-1E4
-3E4
-5E4
-7E4
-9E4
Effective Energy
21
1E2
1E3
1E4
1E5
1E6
Time (MCS)
A
1.2
1.0
0.8
0.6
0.4
0.2
0.0
NWHBL
2E2
1E3
1E4
1E5
1E6
Time (MCS)
B
1.2
1.0
0.8
0.6
0.4
0.2
0.0
NWHBL
2E2
1E3
1E4
1E5
1E6
Time (MCS)
C
4E5
3E5
2E5
1E5
0
Relaxation Time (MCS)
2
4
6
8
10
Interfacial Tension
D

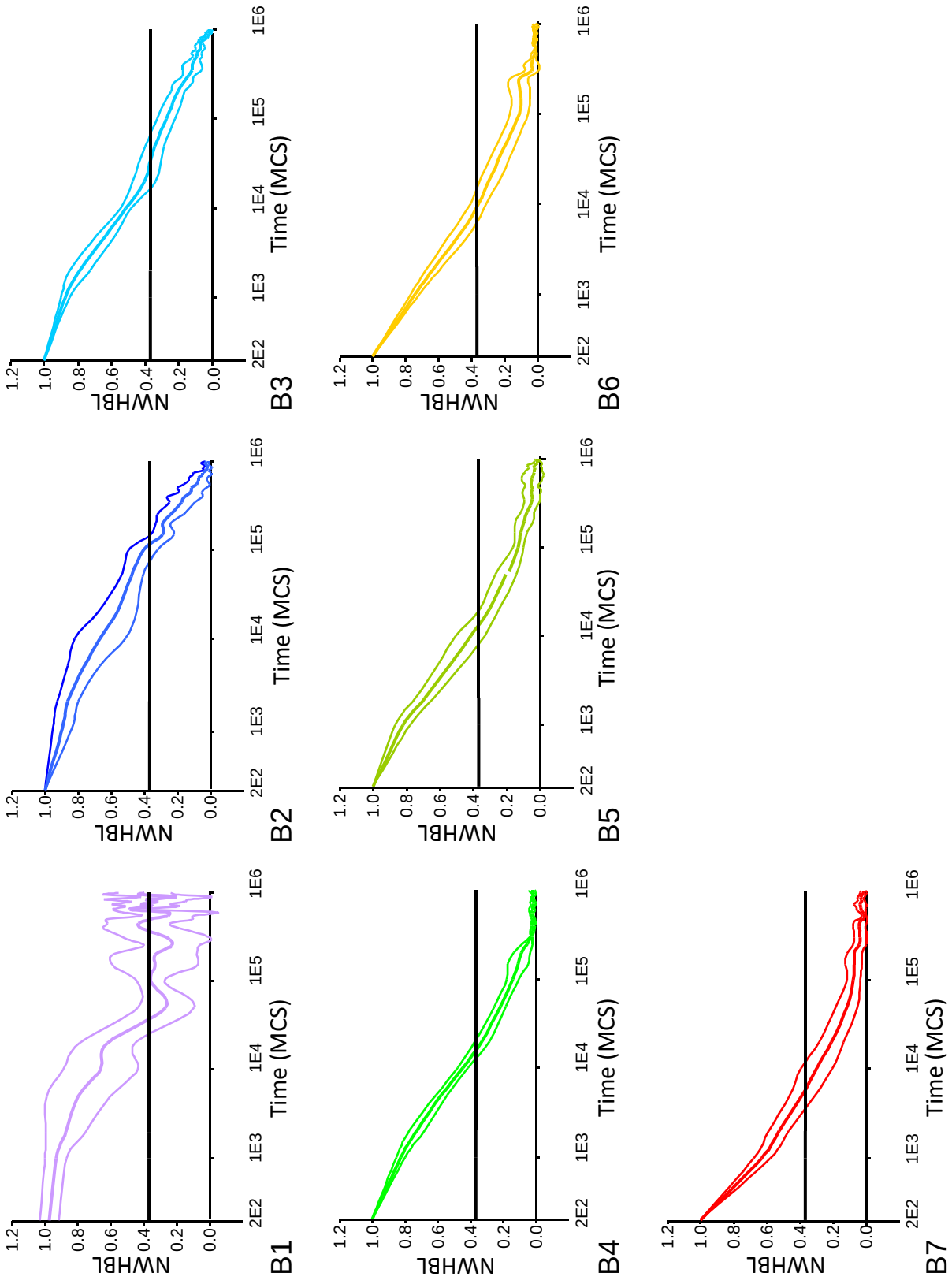
B1
B2
B3
B4
B5
B6
B7
NW/HBL
Time (MCS)
0.0
0.2
0.4
0.6
0.8
1.0
1.2
2E2
1E3
1E4
1E5
1E6

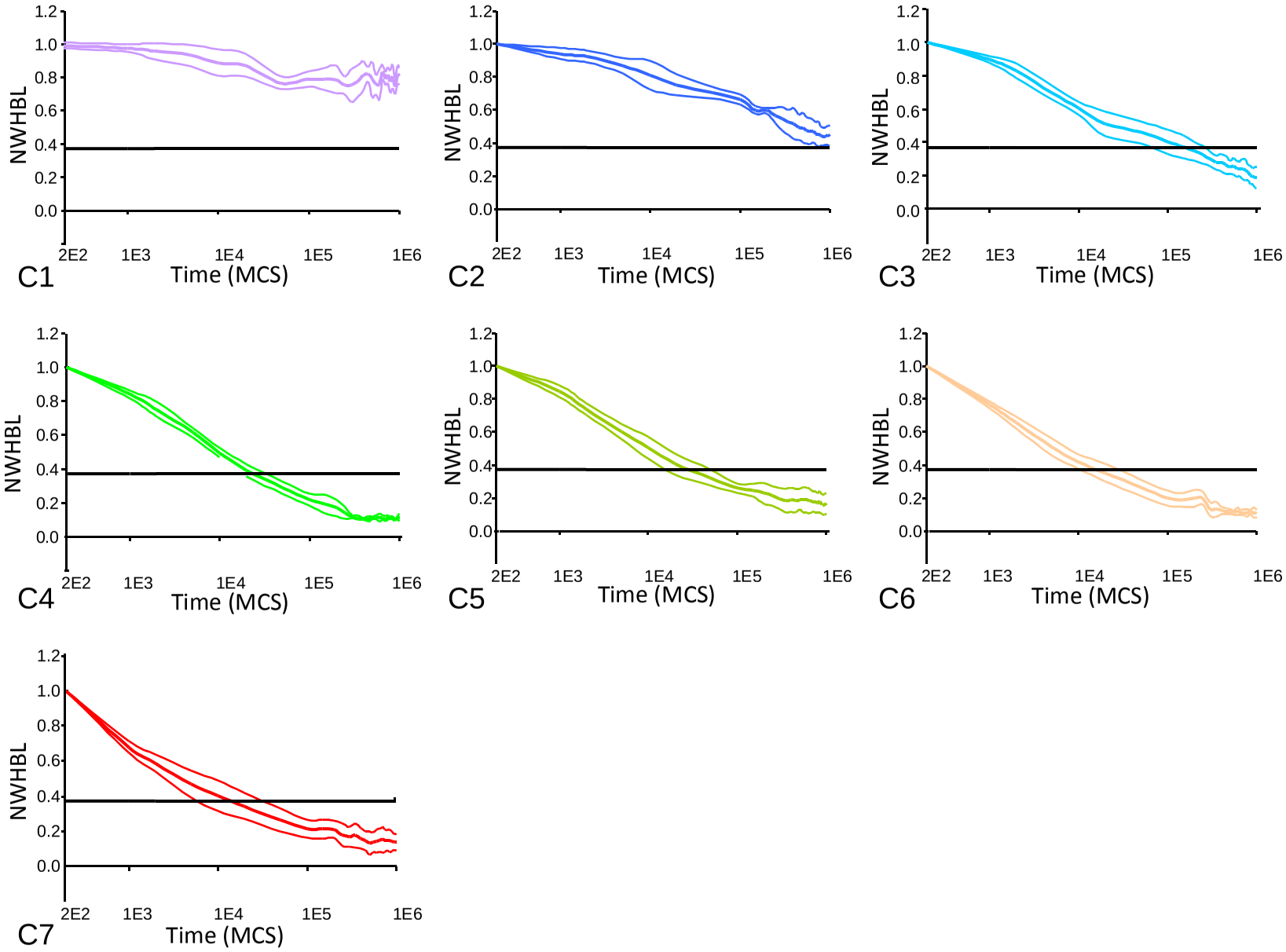
C1
C2
C3
C4
C5
C6
C7
NWHBL
Time (MCS)
1.2
1.0
0.8
0.6
0.4
0.2
0.0
2E2
1E3
1E4
1E5
1E6

Figure 3.3: Time evolution of Effective Energies and Normalized (Weighted) Heterotypic Boundary Lengths for aggregates with differing numbers of cadherins for the trans-homophilic-bond model. Expression ranges: **Dark blue**, [1, 12]. **Light blue**, [1, 14.75]. **Yellow**, [1, 17.50]. **Orange/Pink**, [1, 20.25]. **Red**, [1, 23]. **Green**, [12, 23]. **Purple**, [19.62, 23]. Thick lines show mean values. Thin lines show mean ± standard deviation. Heavy solid horizontal lines mark $1/e$. **A.** Time evolution of the Effective Energy. **B-C.** Time evolution of the Normalized Heterotypic Boundary Length for the same simulations as in A. with: **B.** $L_{min} = L_k$. **C.** $L_{min} = L_{sm}$. **D.** Relaxation time *vs*. interfacial tension. **Dots**, simulation. **Lines**, fitting curves ax^b. **Blue**, $L_{min} = L_k$. **Red**, $L_{min} = L_{sm}$. **B1-B7**. Individual curves for B. **C1-C7**. Individual curves for C.

Last, I explored the effect of cell motility on the time evolution of the Effective Energy and normalized (W)HBL for aggregates with two cadherin levels using the trans-homophilic-bond model. Fig. 3.5A shows the time evolution of the Effective Energy. If the motility is too low ($T = 5$), cells pin before reaching their lowest-energy positions and the Effective Energy remains high. For larger cell motilities, aggregates sort fully. If the motility is too large ($T = 60$ and 80), sorting is rapid but remains incomplete (Figs. 3.5C and D).

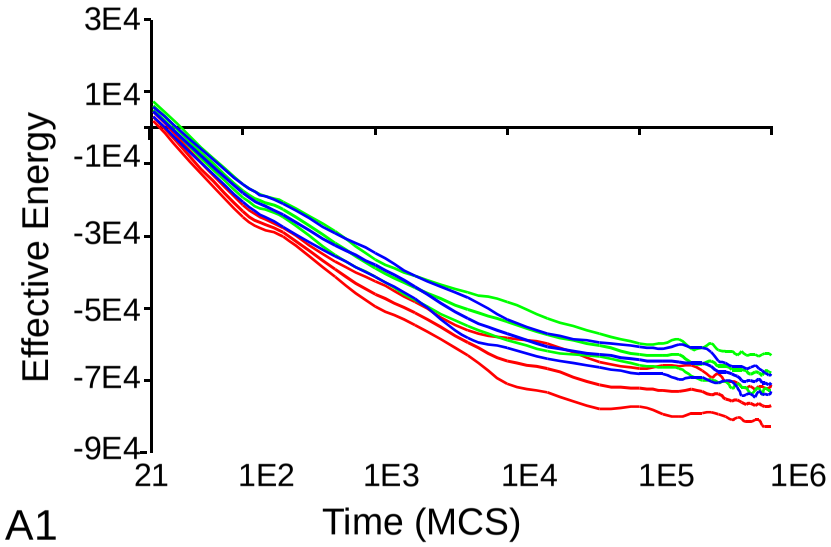
3E4
1E4
-1E4
-3E4
-5E4
-7E4
-9E4
Effective Energy
21
1E2
1E3
1E4
1E5
1E6
Time (MCS)
A1

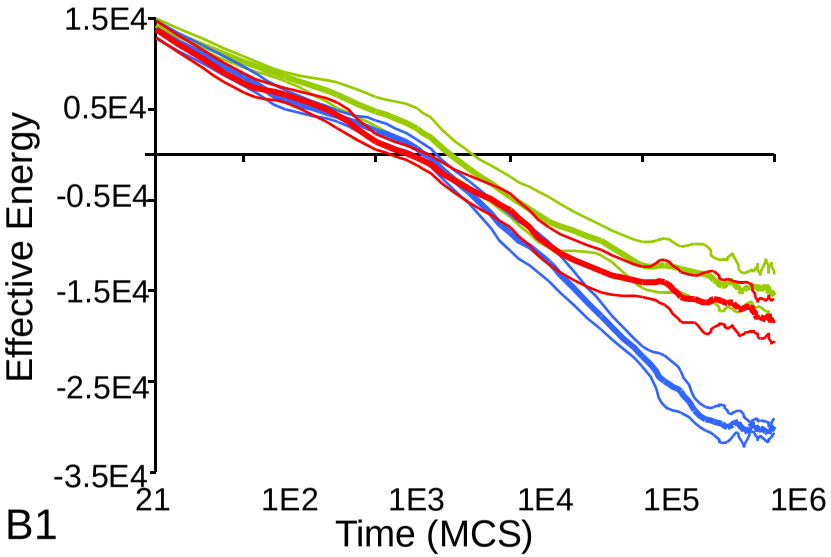
1.5E4
0.5E4
-0.5E4
-1.5E4
-2.5E4
-3.5E4
Effective Energy
21
1E2
1E3
1E4
1E5
1E6
Time (MCS)
B1

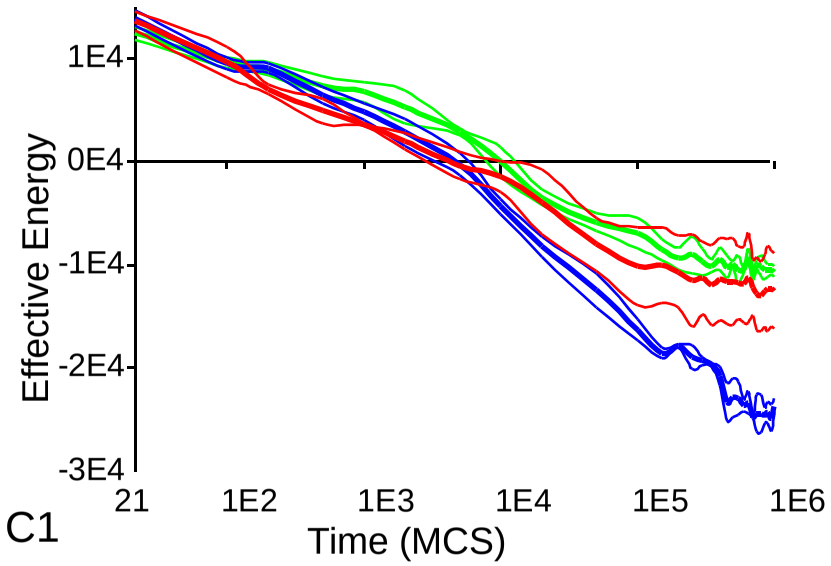
1E4
0E4
-1E4
-2E4
-3E4
Effective Energy
21
1E2
1E3
1E4
1E5
1E6
Time (MCS)
C1

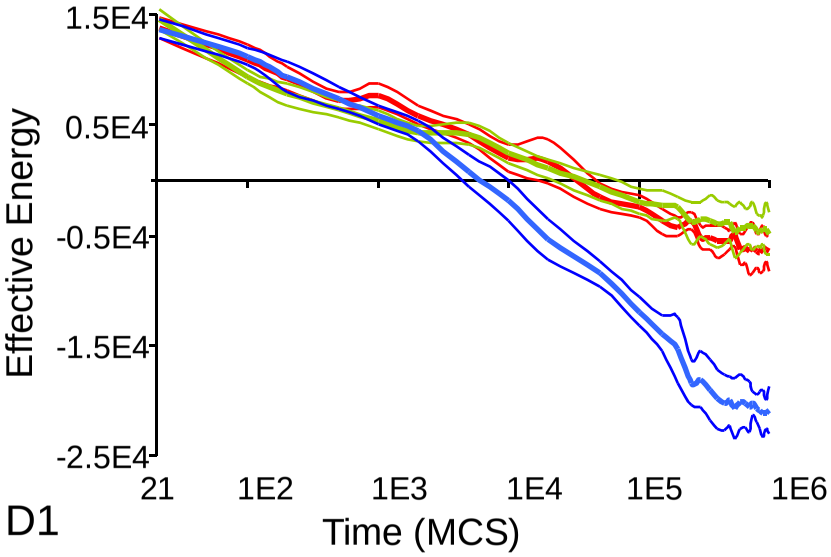
1.5E4
0.5E4
-0.5E4
-1.5E4
-2.5E4
Effective Energy
21
1E2
1E3
1E4
1E5
1E6
Time (MCS)
D1

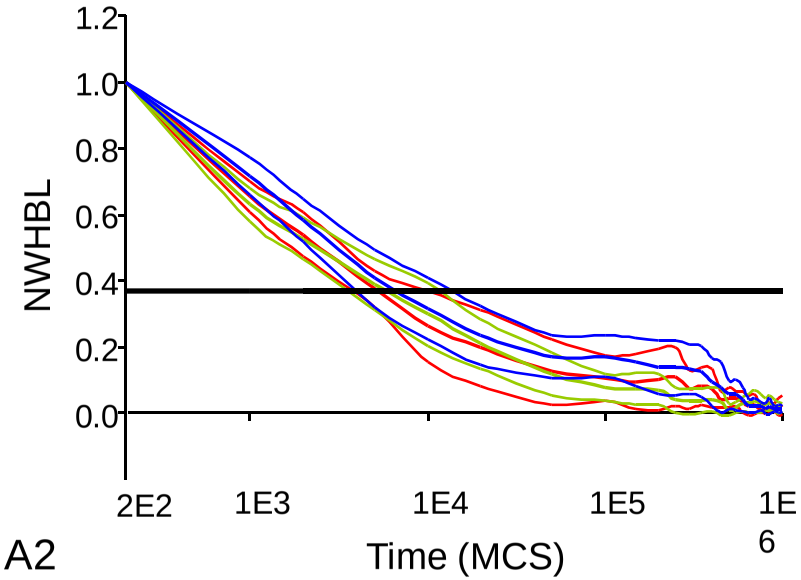
1.2
1.0
0.8
0.6
0.4
0.2
0.0
NWHBL
2E2
1E3
1E4
1E5
1E
6
Time (MCS)

A2

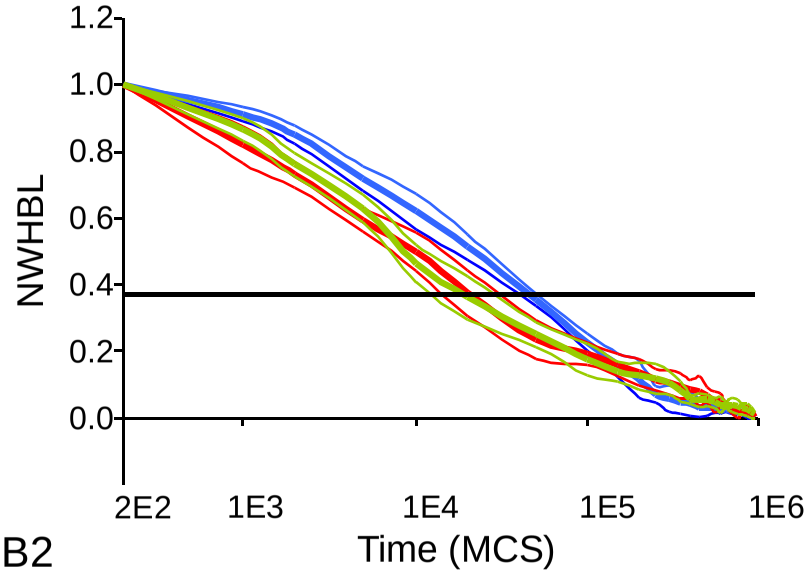
1.2
1.0
0.8
0.6
0.4
0.2
0.0
NWHBL
2E2
1E3
1E4
1E5
1E6
Time (MCS)

B2

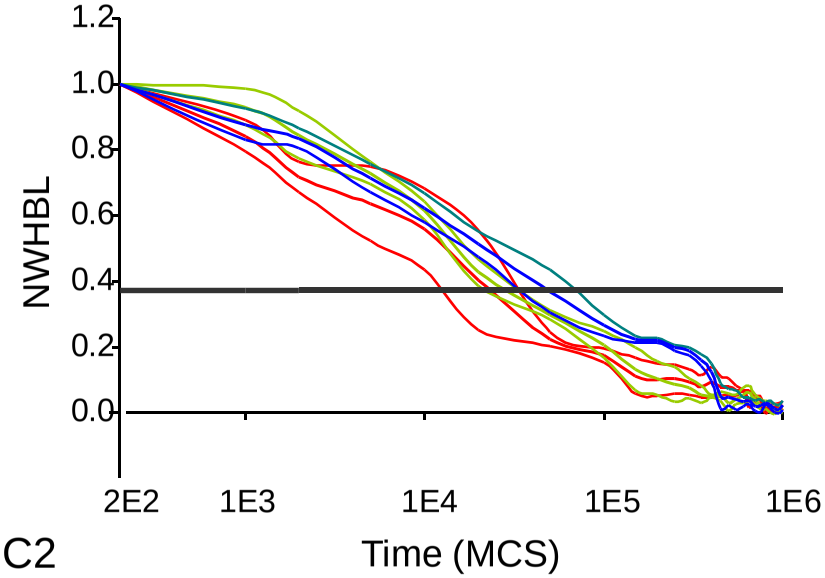
1.2
1.0
0.8
0.6
0.4
0.2
0.0
NWHBL
2E2
1E3
1E4
1E5
1E6
Time (MCS)

C2

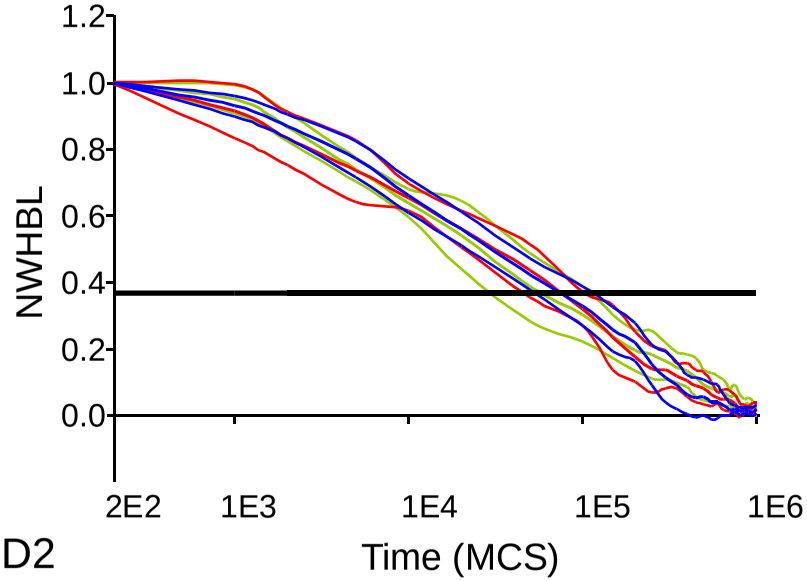
1.2
1.0
0.8
0.6
0.4
0.2
0.0
NWHBL
2E2
1E3
1E4
1E5
1E6
Time (MCS)

D2

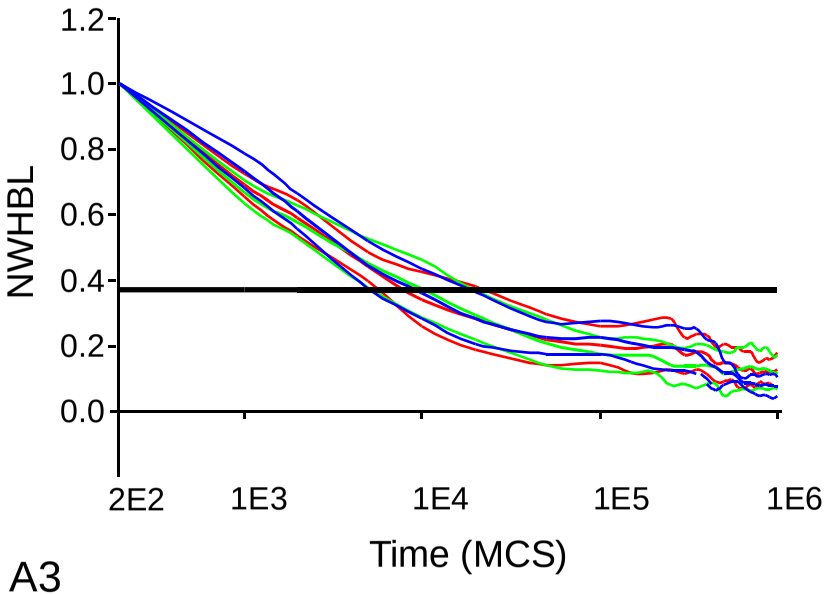
1.2
1.0
0.8
0.6
0.4
0.2
0.0
NWHBL
2E2
1E3
1E4
1E5
1E6
Time (MCS)

A3

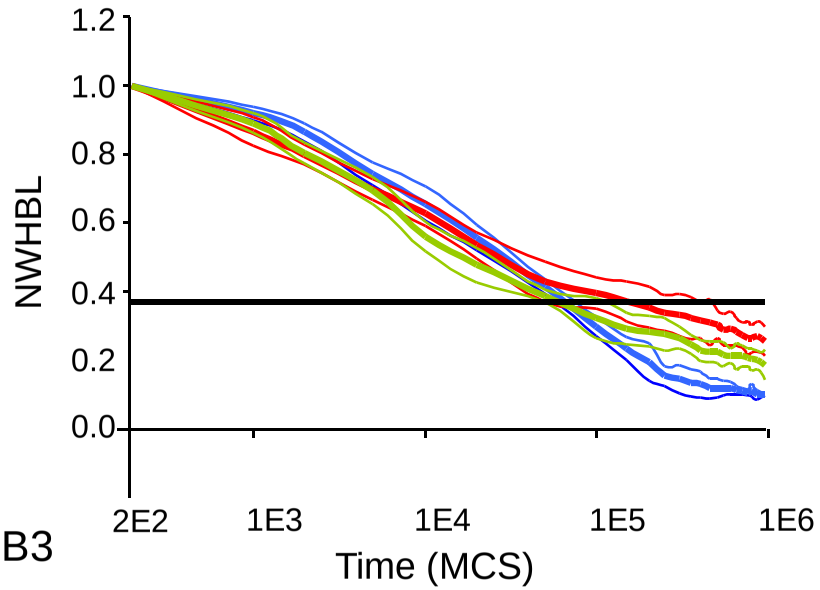
1.2
1.0
0.8
0.6
0.4
0.2
0.0
NWHBL
2E2
1E3
1E4
1E5
1E6
Time (MCS)

B3

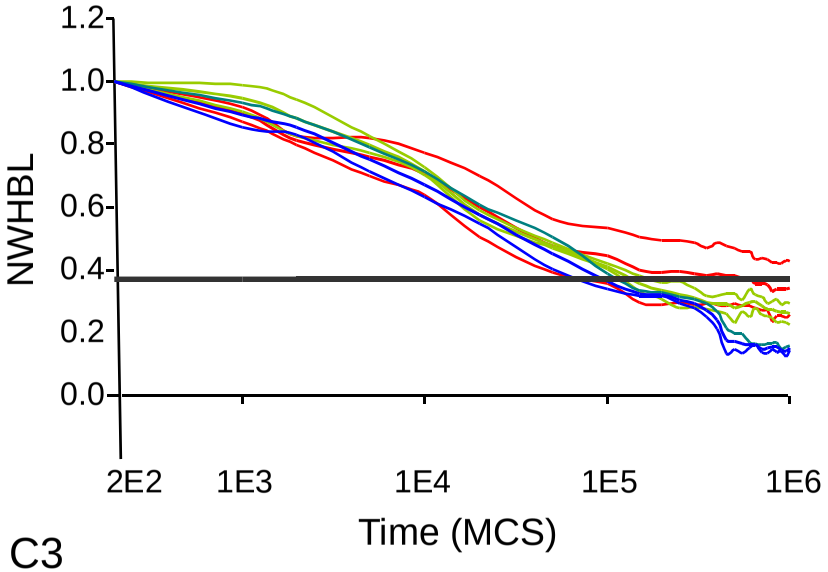
1.2
1.0
0.8
0.6
0.4
0.2
0.0
NWHBL
2E2
1E3
1E4
1E5
1E6
Time (MCS)

C3

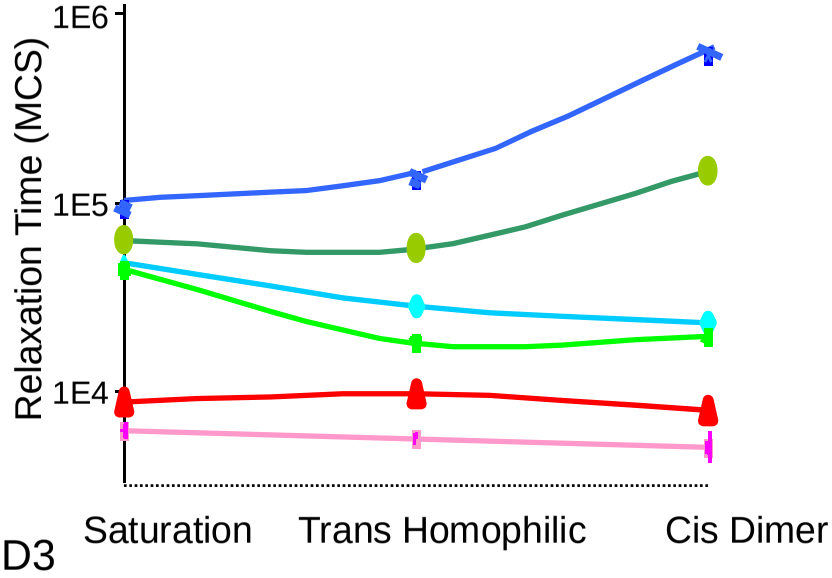
1E6
1E5
1E4
Relaxation Time (MCS)
Saturation
Trans Homophilic
Cis Dimer

D3

Figure 3.4: Time evolution of the Effective Energies and Normalized (Weighted) Heterotypic Boundary Lengths for aggregates with differing numbers of cadherin levels and binding models. The expression range is [1, 23] in all cases. In A1-3, B1-3, C1-3 and D1-2: **Red**, cis-dimer model. **Green**, trans-homophilic-bond model. **Blue**, saturation model. Thick lines show mean values. Thin lines show mean ± standard deviation. Heavy horizontal lines mark $1/e$. In A2, B2, C2 and D2, $L_{min} = L_k$. In A3, B3, and C3, $L_{min} = L_{sm}$. **A1, B1, C1 and D1.** Time evolution of the Effective Energy for aggregates with cells expressing cadherins at two, five, nine and continuous levels, respectively. **A2, B2, C2 and D2.** Time evolution of the Normalized Weighted Heterotypic Boundary Length for the same simulations as A1, B1, C1 and D1, respectively, with $L_{min} = L_k$. **A3, B3, and C3.** Time evolution of the Normalized Heterotypic Boundary Length for the same simulations as A1, B1, C1 and D1, respectively, with $L_{min} = L_{sm}$. **D3.** The relaxation times for different bond models with different levels of cadherin expression. **Red**, two levels with $L_{min} = L_{sm}$. **Pink**, two levels with $L_{min} = L_k$. **Light Green**, five levels with $L_{min} = L_{sm}$. **Green**, five levels with $L_{min} = L_k$. **Dark Blue**, nine levels with $L_{min} = L_{sm}$. **Light Blue**, nine levels with $L_{min} = L_k$.

3.4 Discussion

The framework I have developed allows the quantitative exploration of the dependence of cell sorting on cadherin expression and interaction models. When cells' expression of cadherin varies continuously, sorting still occurs, but more slowly than for discrete

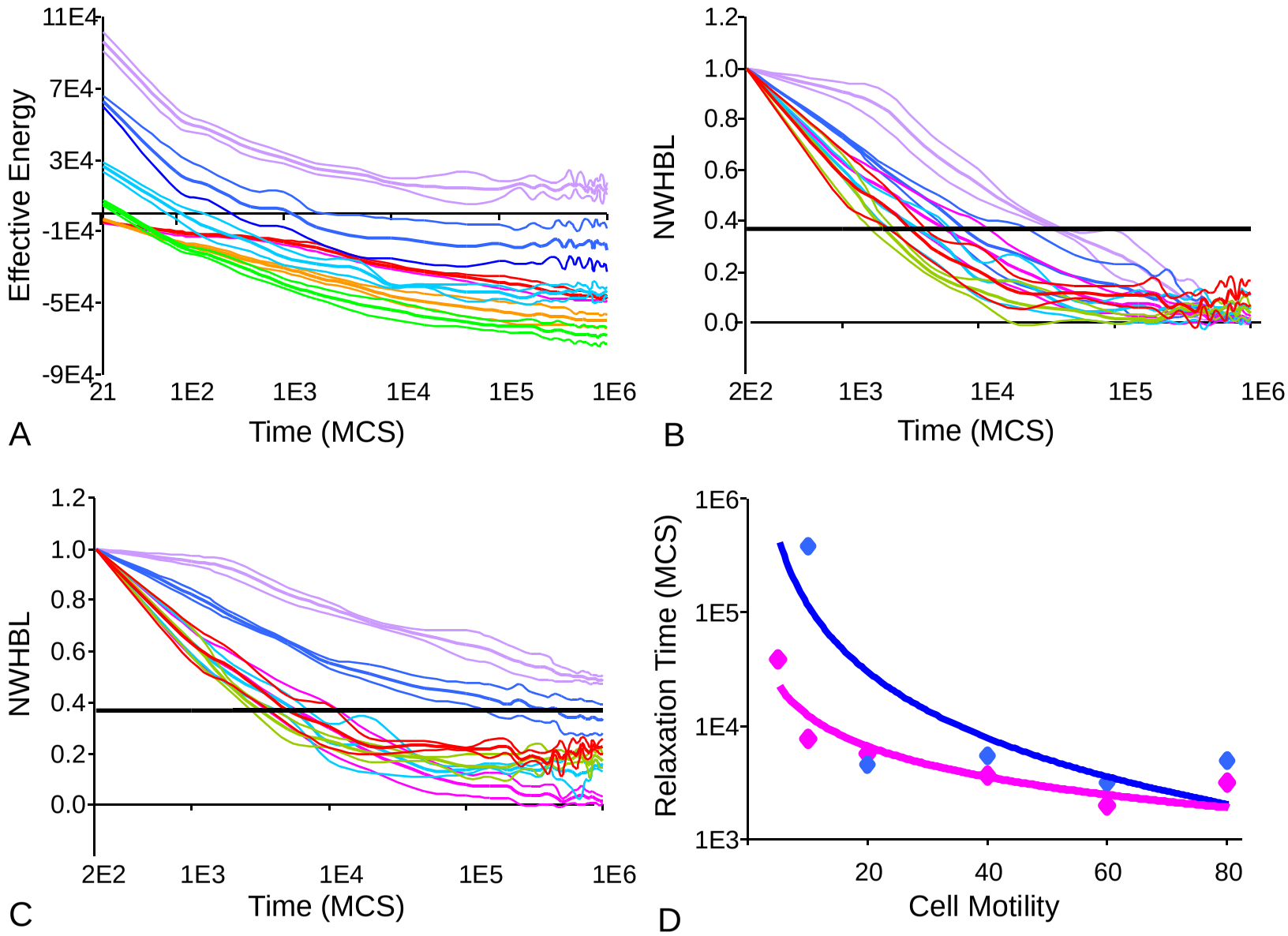
11E4
7E4
3E4
-1E4
-5E4
-9E4
Effective Energy
21
1E2
1E3
1E4
1E5
1E6
Time (MCS)
A
1.2
1.0
0.8
0.6
0.4
0.2
0.0
NWHBL
2E2
1E3
1E4
1E5
1E6
Time (MCS)
B
1.2
1.0
0.8
0.6
0.4
0.2
0.0
NWHBL
2E2
1E3
1E4
1E5
1E6
Time (MCS)
C
1E6
1E5
1E4
1E3
Relaxation Time (MCS)
20
40
60
80
Cell Motility
D

Figure 3.5: Time evolution of the Effective Energies and Normalized (Weighted) Heterotypic Boundary Lengths for aggregates with two cadherin levels for the trans-homophilic-bond model with different motilities. The cadherin expression range is [1, 23]. **Red**, $T = 80$. **Green**, $T = 60$. **Light Blue**, $T = 40$. **Pink**, $T = 20$. **Dark Blue**, $T = 10$. **Purple**, $T = 5$. Thick lines show mean values. Thin lines show mean ± standard deviation. Heavy solid horizontal lines mark $1/e$. **A.** Time evolution of the Effective Energy. **B-C.** Time evolution of the NWHLs, with $L_{min} = L_k$ (**B**) and $L_{min} = L_{sm}$ (**C**). **D.** Relaxation time *vs.* cell motility. **Red**, $L_{min} = L_k$. **Blue**, $L_{min} = L_{sm}$. **Dots**, simulation. **Lines**, fits to at^{-b}.

expression levels. The sorting rate depends on the interfacial tension rather than directly on the expression levels or the cadherin-binding model. Insufficient or excessive motility prevents complete sorting.

Why does sorting occur under most conditions that I considered? For two cadherin levels with $N_A > N_B$, complete sorting requires that (Glazier and Graner, 1993):

$$J(N_A, N_A) < [J(N_A, N_A) + J(N_B, N_B)]/2 < J(N_A, N_B) < J(N_B, N_B). \quad (3.16)$$

Since $-\frac{N_A^2+N_B^2}{2} < -N_A N_B$ for the trans-homophilic-bond model, $-\frac{N_A^4+N_B^4}{2} < -N_A^2 N_B^2$ for the cis-dimer model and $-\frac{N_A+N_B}{2} < -\text{Minimum}(N_A, N_B)$ for the saturation model, the energies all satisfy the sorting condition. Therefore, cells should sort for all three binding models.

Even cells with a continuous distribution of cadherin levels satisfy the sorting inequality, so cells with fewer adhesion molecules envelop cells with more adhesion molecules, which sort

towards the center of the aggregate, creating an adhesion gradient, decreasing from the center to the periphery (Fig. 3.1E). ***Such sorting could be a simple mechanism for cells to reach and maintain their positions during morphogenesis***. I discuss one biologically-significant example of this mechanism in section 4.5.4.

The sorting rate and hence the rate of patterning depend on interfacial tension, which in turn depends on the range of cadherin expression, equilibrium constants and free energies of cadherin bonds (see Eqs. (3.7), (3.7′) and (3.7″)).

Patterns of gene expression are often fuzzy initially, then gradually become distinct. Both changing cell identity and cell movement are possible mechanisms for refining initially-fuzzy expression patterns or for fixing transient patterns of morphogens. These mechanisms may act in parallel with, or coordinate with, other morphogenic mechanisms, such as Turing-type reaction-diffusion instabilities or Wolpertian threshold-based positional coding. *E.g.,* if a transient gradient formed by diffusion, decay and reaction determines a cadherin-expression gradient, differential adhesion can maintain the morphogen profile. If an intracellular morphogen controls cell adhesion, sorting can create a morphogen gradient, reversing the standard hierarchy. The speed of morphogen gradient formation will depend on the interfacial tension.

During development, signaling cascades modulate cadherin expression. Because cell sorting is slow compared to fluctuations in gene-expression levels and because sorting reifies noise into a stable gradient, transient fluctuations in cadherin expression will not change

morphology, increasing developmental robustness. I discuss these issues in more detail in section 4.5.4.

CHAPTER FOUR

COORDINATED ACTION OF N-CAM, N-CADHERIN, EPHA4 AND EPHRINB2 TRANSLATES GENETIC PREPATTERNS INTO STRUCTURE DURING SOMITOGENESIS IN CHICK[1]

Abstract

During gastrulation in vertebrates, mesenchymal cells at the anterior end of the presomitic mesoderm (*PSM*) periodically compact, transiently epithelialize and detach from the posterior PSM to form somites. In the prevailing *clock-and-wavefront* model of somitogenesis, periodic gene expression, particularly of Notch and Wnt, interacts with an FGF8-based thresholding mechanism to determine cell fates. However, this model does not explain how cell determination and subsequent differentiation translate into somite morphology. In this chapter, I use computer simulations of chick somitogenesis to show that experimentally-observed temporal and spatial patterns of adhesive N-CAM and N-cadherin and repulsive EphA4-ephrinB2 pairs suffice to reproduce the complex dynamic morphological changes of somitogenesis in wild-type and N-cadherin (-/-) chick, including intersomitic separation, boundary shape evolution and sorting of misdifferentiated cells across compartment boundaries. Since different models of determination yield the same,

[1] This chapter has been published as Glazier *et al.,* 2007.

experimentally-observed distribution of adhesion and repulsion molecules, the patterning is independent of the details of this mechanism.

4.1 Introduction

Somitogenesis, during which initially-continuous anterior-posterior (*AP*) bands of loosely-bound cells on either side of the medial primitive streak, the pre-somitic mesoderms (*PSM*), break apart sequentially and periodically (at intervals of ~90 minutes in chick) in AP sequence into a spatially-regular series of separated, tightly-bound *somites* is the classical example of *segmentation* during vertebrate embryogenesis. In vertebrates, somites are the precursors of vertebrae, muscle and skin derivatives, and provide a scaffold for assembly of the peripheral vasculature and nervous system (Gossler and Hrabe de Angelis, 1998).

Somite formation requires: (i) Physical separation of somitic tissue from the initially-continuous PSM, (ii) Coalescence of cells in the forming somite, and (iii) The establishment of a stable border between the somite and the PSM.

Experimentally, animal species differ in the cell rearrangements which create the somite-PSM border and how aggressively new somites pull apart from the PSM (Kulesa *et al.,* 2007). In *Xenopus* embryos, two short, discrete fissures start from both the medial and lateral edges of the PSM and expand gradually towards the middle of the PSM to form a stable somite-PSM border (Afonin *et al.*, 2006). In zebrafish embryos, cell rearrangements within

forming somites are minimal and the forming-somite-PSM border develops when cells in the forming somite gently detach from their PSM neighbors, forming a medial notch which spreads laterally (Wood and Thorogood, 1994; Henry *et al.,* 2000; Jiang *et al.,* 2000). In both animals, the cells then retract towards the center of the forming somite or towards the PSM, depending on the side of the somite-PSM boundary.

In chick embryos, cell rearrangements during somite-PSM border formation are more dramatic. Somitogenesis occurs in a complex spatio-temporal pattern, not *via* simple cleavage of the PSM (Kulesa and Fraser, 2002). Time-lapse analyses reveal that the forming somite-PSM boundary develops a dynamic *ball-and-socket* shape and that some cells cross the presumptive somite-PSM boundary (Kulesa and Fraser, 2002). Tissue transplantation studies have shown that cells in the region near the posterior border of the forming somite possess border-forming signals mediated by Notch and reinforced by Lunatic Fringe (Sato *et al.,* 2002). Transplantation of the ventral–most cells in the posterior of the forming somite induces formation of ectopic borders and somite subdivisions in more dorsal PSM tissues (Sato and Takahashi, 2005). Thus, in chick, the initial separation of a forming somite from the PSM appears to occur in a ventral-to-dorsal (*VD*) direction. However, in line with most experimental and computational studies, this chapter will treat the PSM and somites as essentially two-dimensional, neglecting VD and medial-to-lateral (*ML*) variation.

To explain the complex cell rearrangements in chick somitogenesis I employ computer simulations, which allow me to study how previously-determined spatio-temporal variations in gene expression (*prepatterns*) lead to variations in cell adhesion and local

microenviroment, which induce cell rearrangement into coherent somites. The rearrangements, in turn, can further affect gene expression (*feedback*).

Essentially all models of somitogenesis to date have neglected the properties and movement of individual cells, and concentrated on mechanisms to generate periodic patterns of gene expression in the PSM, *i.e*., *somite specification*. This focus on early gene expression seemed reasonable, because determination of cell fate occurs early, about three somitic-clock cycles (about 4½ hours) before physical segmentation (Dubrulle and Pourquié, 2004). The existence of a prepattern is consistent with the finding that reversal of the AP axis of the PSM leads to reversed somites (Keynes and Stern, 1988). The numerous theoretical models of gene-expression patterning include (Schnell and Maini, 2000; Baker *et al.,* 2003, 2006), the *clock-and-wavefront* model (Cooke and Zeeman, 1976; Dubrulle *et al.,* 2001) *reaction-diffusion* models (Meinhardt, 1996), *cell-cycle* models (Primmett *et al.,* 1988, 1989; Stern *et al.,* 1988; Collier *et al.,* 2000), and the *clock-and-induction* model (Schnell and Maini, 2000). Each of these models includes certain key features of the underlying biology and predicts that the PSM develops spatially-periodic patterns of gene expression in tissue blocks, but fails to explain some experimental observations. Pourquié and co-workers' version of the clock-and-wavefront model (Durbrulle and Pourquié, 2002; Pourquié, 2004) is, perhaps, the most successful (Baker *et al.,* 2006).

The actual process of somite formation–how a somite pulls apart from the PSM and the ensuing morphological changes–is not well understood. The only mathematical model attempting to describe the bulk movement of somitic cells to form a somite (Schnell *et al.,*

2002) does not account for the intercellular mechanical forces involved in somite formation. Grima and Schnell (Grima and Schnell, 2007) have investigated the possibility that minimization of tissue surface tension drives the subsequent morphological changes leading to rounded somites. This chapter addresses another question—**given a prepattern of gene expression, can known biological mechanisms give rise to the patterns of cell movement and morphological changes observed in both wild-type and gene-knock-out experiments**? My model is completely agnostic about the origin of this pattern of gene expression (it works equally well with any of the somite-specification models in the preceding paragraph).

4.1.1 Nomenclature

Because somitogenesis proceeds in a temporally-periodic and spatially-progressive fashion, the identity of groups of cells changes in time, making nomenclature somewhat confusing (See Fig. 4.2). I use the nomenclature most common in the experimental community. At the beginning of a 90-minute cycle of somite formation, the anterior-most portion of the PSM becomes the site of a newly forming somite, which I refer to as S_0; I will then refer to the portion of PSM immediately posterior to the region which contains the forming somite as the *anterior PSM* or S_{-1}. Initially, these two regions are contiguous; the forming somite S_0 then gradually separates from the remaining PSM along the *presumptive somite-PSM boundary*. When somite separation is complete, the forming somite S_0 becomes somite S_1, the anterior portion of the remaining PSM, S_{-1}, becomes S_0 and the cycle repeats (Ordahl, 1993; Pourquié

and Tam, 2001). I call the regions of the PSM successive somite lengths behind S_{-1}, S_{-2}, S_{-3}, ... Each somite also has an anterior and posterior compartment, which I will denote S_{-1A} and S_{-1P}, respectively, and a central (or core) and peripheral region.

4.2 Patterns of Gene Expression and Protein Distribution during Somitogenesis

To understand how the gene expression prepattern translates into changes in tissue morphology, I first review the functions of key molecules and their expression patterns.

4.2.1 Cell Adhesion Molecules

N-CAM and N-cadherin are homophilic membrane-bound proteins which contribute to contact adhesion between cells. The strength of adhesion increases with protein density and type on each cell, though, as I have addressed in Chapters Two and Three, the form of the dependence is not completely clear (Foty and Steinberg, 2005). While both molecules are homotypically adhesive as isolated monomers, they normally associate into groups which then aggregate in the cell membrane to form clusters (*e.g.*, clusters of trimers of dimers) which increases the effective binding-strength per molecule. Both molecules bind to the actin cytoskeleton *via* β-catenin. This binding affects their effective adhesivity directly, possibly through changes in conformation of their extracellular domain, and indirectly, because a

functional actin cytoskeleton is necessary for their clustering. In general, for a given receptor density, N-CAM results in weaker adhesion than N-cadherin.

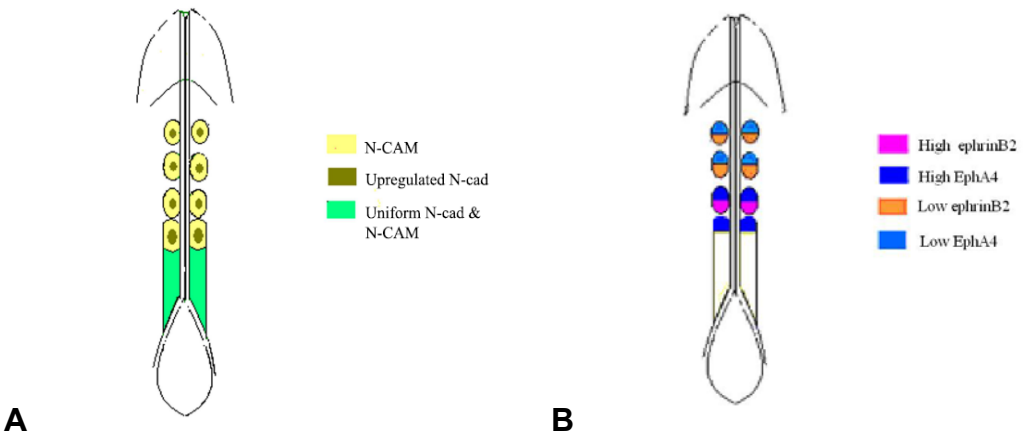

Figure 4.1: Schematic diagram of the distribution of adhesion and repulsion molecules within the segmenting tissue during chick somitogenesis. A. N-cadherin and N-CAM protein distributions based on immunocytochemistry experiments (Linask *et al.,* 1998). The PSM has a uniform low background level of N-cadherin and N-CAM. N-CAM levels do not change significantly during segmentation, while N-cadherin levels increase in the inner core of the forming somite. **B.** EphA4 and ephrinB2 levels based on *in situ* hybridization experiments (Baker and Antin, 2003; Aulehla and Pourquié, 2006). During segmentation EphA4 expresses in the anterior compartment of the forming somite and the anterior of the PSM; ephrinB2 expresses in the posterior compartment of forming somite. Both EphA4 and ephrinB2 mRNA levels decrease after the somite has separated from the PSM.

In avian and mouse embryos, somite formation follows compaction (*i.e.*, a reduction in the intercellular space between cells) and the heightened expression of N-CAM and N-cadherin (Duband *et al.,* 1987; Linask *et al.,* 1998), which are expressed at lower levels in the rest of the PSM (Fig. 4.1A). In mice (Kimura *et al.,* 1995), cadherin-11 strictly correlates with S_0; it is not expressed in other parts of the PSM. Fig. 4.1A schematically illustrates the dynamic changes of cell-adhesion molecule types and concentrations during somite segmentation in chick embryos. Before segmentation, mesenchymal cells in the PSM weakly express N-CAM and N-cadherin. During segmentation, the condensing cells in S_0 significantly increase their N-CAM and N-cadherin expression.

Before and during somite separation, the cells at the periphery of S_0 epithelialize (Dubrulle and Pourquié, 2004). During this epithelialization, N-CAM remains uniformly distributed over the entire surfaces of epithelial cells, whereas N-cadherins concentrate predominantly on the apical surfaces (which somewhat counter-intuitively face towards the center of the somite)**.** Cells located in the core of the somite remain mesenchymal and continue to have essentially uniform surface distributions of both N-CAM and N-cadherin (Duband *et al.,* 1987; Linask *et al.,* 1998).

4.2.2 Eph/ephrin-Induced Cell "Repulsion"

Ephs and ephrins are families of heterotypically-active cell-surface receptors that can lead to effective "repulsion" between a cell expressing an Eph and a cell expressing the

corresponding ephrin. How contact leads to effective repulsion is still under active investigation. A plausible mechanism is that pairing of complementary Ephs and ephrins on apposing cells triggers bidirectional signaling, which results in the local collapse of the actin cytoskeleton in both cells near their point of contact (Harbott and Nobes, 2005). This collapse then locally disrupts the condensation and pairing of cell adhesion molecules like N-CAM and N-cadherin, which reduces, but need not completely eliminate, the strength of their homotypic intercellular binding (as suggested in Kasemeier-Kulesa *et al.,* 2006 and Cooke *et al.,* 2005). Thus EphA4-ephrinB2 "repulsion" in somites may actually result from a reduction in effective cell-cell adhesion. Since Eph-Eph and ephrin-ephrin apposition has no effect on the cytoskeleton, cell adhesion molecules remain fully functional within the interior of an Eph-expressing or ephrin-expressing domain. Thus boundaries between domains expressing an Eph and its complementary ephrin are structurally weak, while the domains themselves can be strong, allowing tissue to pull apart along Eph/ephrin contact lines. Collapse of the actin cytoskeleton also destroys the pseudopods or leading edges which cells use to move in a particular direction (Mellitzer *et al.,* 1999; Xu *et al.,* 1999; Poliakov *et al.,* 2004), preventing a cell expressing Eph from moving into a cluster of cells expressing the corresponding ephrin and *vice versa* (*contact inhibition*). The net effect is to establish compartmental boundaries between clusters of cells expressing Eph and clusters of cells expressing the complementary ephrin. Such boundaries are clearly visible using ordinary microscopy.

Eph/ephrin signaling is responsible for boundary formation in the developing hindbrain (Mellitzer *et al.,* 1999; Xu *et al.,* 2000) and is necessary for the formation of intersomitic

boundaries and subsequent epithelialization (Durbin *et al.,* 1998). During somite segmentation, EphA4 expresses in the anterior half of somites (S_{0A}) and in the anterior tip of the PSM (S_{-1A}), while ephrinB2 expresses in the posterior half of somites (S_{0P}) (Fig. 4.1B) (Nieto *et al.,* 1992; Bergemann *et al.,* 1995; Durbin *et al.,* 1998; Baker and Antin, 2003; Baker *et al.,* 2003). EphA4/ephrinB2 signaling also regulates the mesenchymal-to-epithelial transition of the PSM during somitogenesis (Barrios *et al.,* 2003).

4.2.3 Interaction between Adhesion and Repulsion during Somitogenesis

That the adhesive interactions of N-CAM and N-cadherin are homophilic while EphA4 and ephrinB2 produce an effective *heterorepulsion* (repulsion between cells of two complementary types) is crucial to the observed mechanics of somite formation. Cells expressing EphA4 and cells expressing ephrinB2 meet both at the presumptive somitic boundary (S_{0P} to S_{-1A}) and inside each somite (at the center of S_0, *i.e.*, S_{0A} to S_{0P}). If contact between cells expressing EphA4 and cells expressing ephrinB2 causes the separation of the posterior end of S_0 (S_{0P}) from the anterior end of the PSM (S_{-1A}), why does it not cause a similar boundary to form inside S_0 (between S_{0A} and S_{0P}) subdividing it into two non-contacting smaller somites? N-cadherin in the center of the somite seems to be essential, since, in mouse, knocking out N-cadherin results in segmentation of normal somites into two separated sub-somites (Kimura *et al.,* 1995; Radice *et al.,* 1997; Horikawa *et al.,* 1999). One question I will investigate through simulation is what interactions of adhesion and repulsion lead to segmentation without fragmentation of individual somites.

4.2.4 From Genetic Oscillators to Adhesion/Repulsion-Protein Patterns

Molecular signaling during segmentation prepattern specification is still a subject of intensive research. The following highly simplified and speculative description provides at least a working hypothesis for these mechanisms. The embryo elongates primarily through division of cells in the extreme posterior of the PSM and in the tail bud. Cells leave the tail bud then cease to transcribe fgf8 mRNA. fgf8 mRNA slowly degrades, but continues to be translated into FGF8 protein (Dubrulle and Pourquié, 2004); thus the average level of FGF8 in more anterior PSM cells is lower than in more posterior cells. In addition, the precursor to retinoic acid (*RA*), RALDH2 diffuses into the PSM from the anterior of the embryo. FGF8 and RA couple antagonistically within cells to select either high-RA or high-FGF8 states in a bistable manner (Diez del Corral *et al.,* 2003; Goldbeter *et al.,* 2007). Above a threshold level of FGF8, individual cells in the PSM exhibit spontaneous oscillations in expression levels of many genes, especially those belonging to the Notch, Wnt and FGF signaling cascades (Palmeirim *et al.,* 1997, Dequeant *et al.,* 2006; Kulesa *et al.,* 2007), with a period which depends on cytoplasmic FGF8 levels. Neighboring cells' oscillators synchronize *via* Delta-Notch signaling (Horikawa *et al.,* 2006). The oscillation of FGF8 activity is superimposed on the background decrease of FGF8, a somewhat unusual circuit that results in a whole block of cells (the size of one somite, or about 200 microns in chick) switching to the high-RA state nearly simultaneously. The combination of this switch with the local phase of the oscillation determines the cell's later differentiation (Aulehla *et al.,* 2003; Aulehla and Herrmann, 2004). Oscillations cease some time after this switch, but their persistence has no known effect on cell differentiation.

The phase read-out during cell determination seems to depend on Wnt signaling (Aulehla and Pourquié, 2006), though the full regulatory cascades are not known. Fig. 4.2 summarizes regulatory interactions (bottom) and AP expression patterns (top). The fundamental prepatterning mechanism is the inhibitory coupling from Notch to Wnt, *via* Axin2, Nkd1 and other pathways, which leads to elevated levels of Wnt in the centers of presumptive somites and of Notch at presumptive somite boundaries. The expression domains are fairly broad, with substantial overlap in the regions midway between a presumptive somite's center and its boundaries. Wnt stabilizes cytoplasmic β-catenin, which acts as a transcription factor increasing expression of N-cadherin, which accumulates in a broad area around the presumptive somite core (Nelson *et al.,* 2004). Notch similarly transiently upregulates Eph/ephrin expression and activity at the presumptive somite boundaries. The selective expression of the transcription factor Mesp2 activated by RA (Moreno and Kintner, 2004) in the anterior half of each presumptive somite defines anterior and posterior compartments by inhibiting DLL1 expression in the anterior compartments (Takahashi *et al.,* 2003). Mesp2 further leads to transient expression of EphA4 in the anterior compartments (Nakajima *et al.,* 2006), which peaks near the presumptive anterior boundary. In the posterior compartments, DLL1 maintains ephrinB2 expression (De Bellard *et al.,* 2002), peaking near the presumptive boundary. Other protein level changes result from unknown mechanisms. The time lag from determination to segmentation seems primarily to result from transcriptional and translational delays and the time required for EphA4, ephrinB2, N-CAM and N-cadherin to reach functional levels (Kulesa, 2007). ephrinB2 levels seems to increase more slowly than do the levels of the other molecules. I have included this difference in the timing of molecular level changes in my simulations; however, the exact sequence is not crucial to my results.

4.2.5 From Adhesion-Protein Patterns to Segmentation

Based on experiments that show that cells in the PSM condense into somites by changing their adhesive and migratory properties (Gossler and Hrabe de Angelis, 1998), my key hypothesis is that the primary ways that the cells' internal differentiation states translate into mechanical activity are through:

1) Differential expression and binding of the cell-adhesion molecules N-CAM and N-cadherin.
2) Differential expression and bidirectional activation of EphA4 receptors and ephrinB2 proteins.

Segmentation then results from the spatio-temporal coordination of N-CAM, N-cadherin and Eph/ephrin expression.

4.3 Segmentation Model

I use a two-dimensional approximation, neglecting DV variations. I also neglect medio-lateral (*ML*) variations in cell properties (which may be quite important in many cases), assume that the intrinsic level of cytoskeletal cell motility is constant in all cells and that cells do not divide or die.

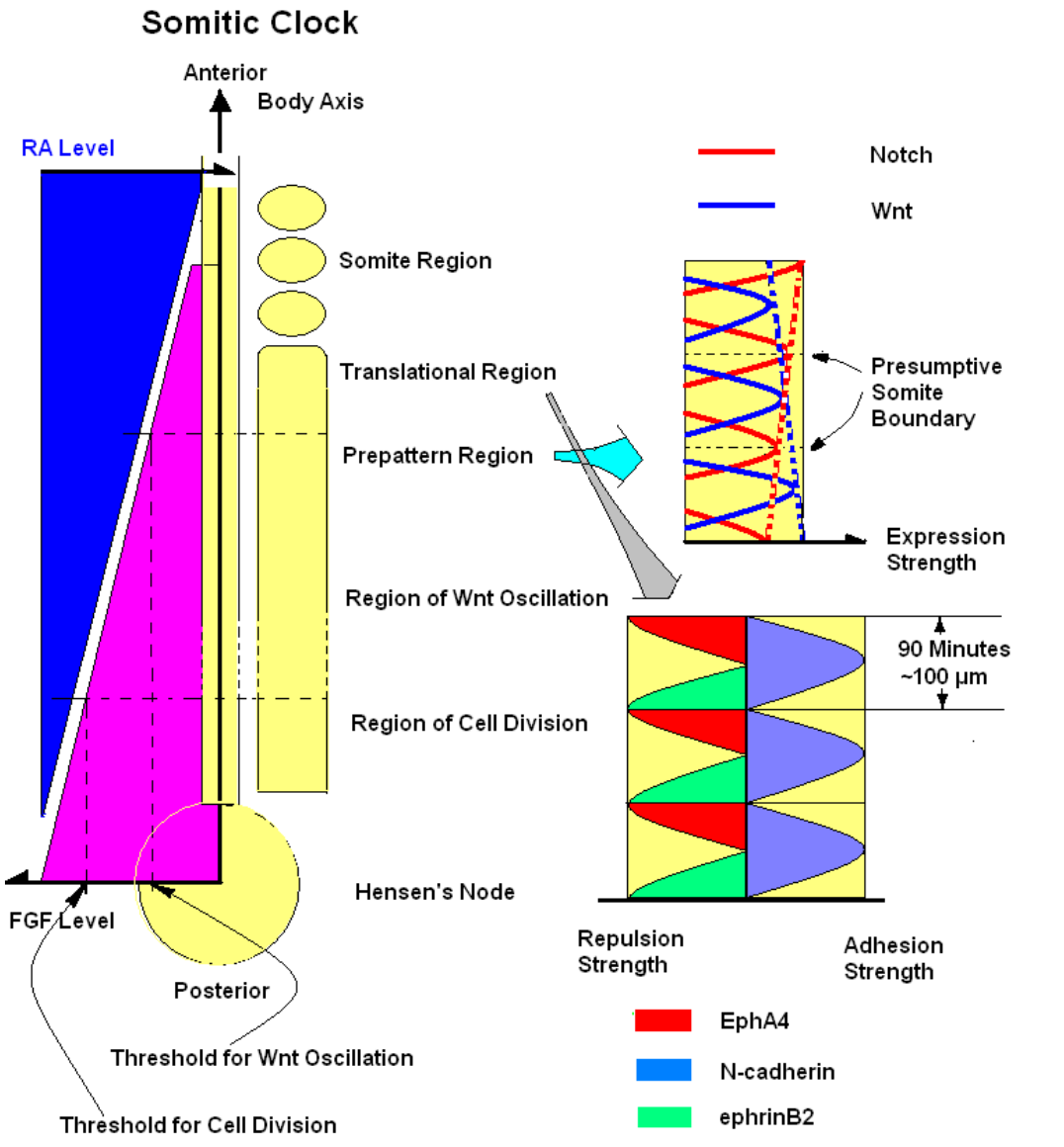
Somitic Clock
Anterior
Body Axis
RA Level
Somite Region
Translational Region
Prepattern Region
Region of Wnt Oscillation
Region of Cell Division
Hensen's Node
FGF Level
Posterior
Threshold for Wnt Oscillation
Threshold for Cell Division
Notch
Wnt
Presumptive Somite Boundary
Expression Strength
90 Minutes
~100 µm
Repulsion Strength
Adhesion Strength
EphA4
N-cadherin
ephrinB2

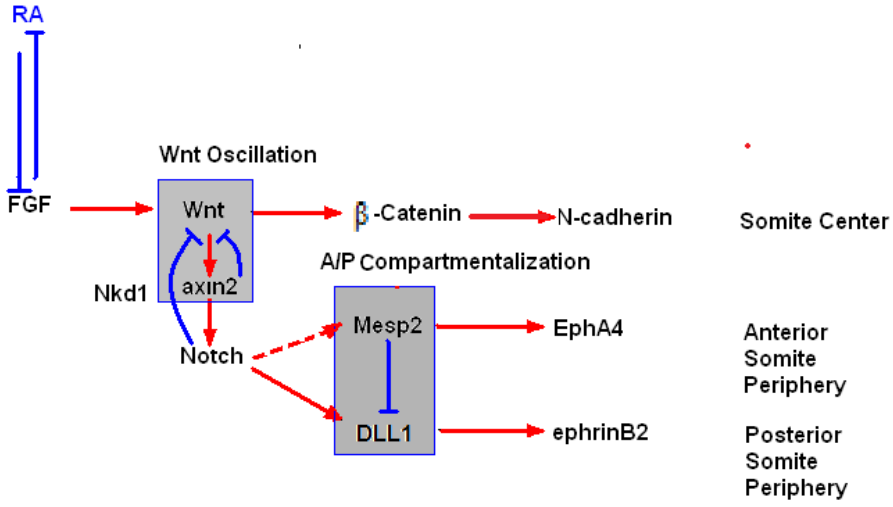
RA
FGF
Wnt Oscillation
Wnt
β-Catenin
N-cadherin
Somite Center
Nkd1
axin2
A/P Compartmentalization
Notch
Mesp2
DLL1
EphA4
ephrinB2
Anterior Somite Periphery
Posterior Somite Periphery

Figure 4.2: Schematic diagram of the translation of FGF8, Wnt and Notch cyclic expression into spatially-periodic patterns of N-cadherin, EphA4 and ephrinB2. Top Left. Within the PSM, fgf8 mRNA decay decreases FGF8 protein levels. Above a threshold FGF8 concentration, intracellular Wnt concentration oscillates with a period of ~90 minutes. Intercellular Delta-Notch signaling (not shown) synchronizes neighboring cells, producing coherent oscillations in Wnt concentration. **Top Right**. When the FGF8 concentration falls below a threshold, Wnt oscillations cease, creating a spatial oscillation in Wnt levels. The inhibitory interaction between Wnt and Notch leads to out-of-phase expression of Wnt and Notch. **Middle Right**. N-cadherin, EphA4 and ephrinB2 levels. N-cadherin expression is maximal at the cores of somites. EphA4 is expressed in anterior somite compartments and ephrinB2 in posterior compartments. Both are maximal at somite boundaries. **Bottom**. Plausible regulatory links from Wnt and Notch to N-cadherin, EphA4 and ephrinB2. The mutual inhibition of Wnt and Notch by axin2 and Nkd1 causes the Wnt and Notch oscillation. In the anterior somite, Notch signaling is suppressed by Mesp2, which also induces EphA4 expression. In the posterior somite, EphrinB2 is maintained by DLL1.

Based on the biological observations I described above, my model assumes that somitogenesis depends predominantly on four molecular species: N-CAM, N-cadherin, EphA4 and ephrinB2. I make a number of simplifying assumptions concerning the behavior and spatiotemporal expression patterns of these molecules. I assume that the distribution of these adhesive and repulsive species is uniform over cell membranes and that the primary

effect of peripheral epithelialization is to change the relative cell sizes and adhesions in the somite core and periphery rather than redistributing adhesion molecules over the cell surface.

I assume that binding of EphA4 and ephrinB2 on apposing cells reduces their effective adhesion due to their cell-adhesion molecules. However, I do include the variation in levels of molecular expression between the core and periphery of each somite and between the anterior and posterior halves of each somite compartment.

I assume the following temporal sequence of molecular distributions (see Fig. 4.3). All molecular levels turn on abruptly at the beginning of a segmentation cycle (times t_0, t_1, t_2, t_3,…) and remain the same until the end of the simulation. In reality, these levels would change further as the somites matured, but the chief focus of this chapter is the initial formation of the somites rather than their later maturation. I do not attempt to model the origin of the somite-cycle timing. Within the posterior PSM (S_{-2}, S_{-3},…), all cells express a uniform background level of N-CAM and N-cadherin, keeping the cells loosely connected. At the beginning of each segmentation cycle, N-cadherin levels in the cells at the core of S_{-1} (the somite posterior to the forming somite) increase substantially, N-cadherin levels in cells at the periphery of S_{-1} decrease, high levels of EphA4 appear in the anterior half of the anterior compartment (S_{-1A}) and low levels in the posterior half of the anterior compartment (S_{-1A}). To represent the delayed appearance of ephrinB2, I also turn on a low level of ephrinB2 in the anterior half of S_{0P}, and a higher level in the anterior half of S_{0P}.

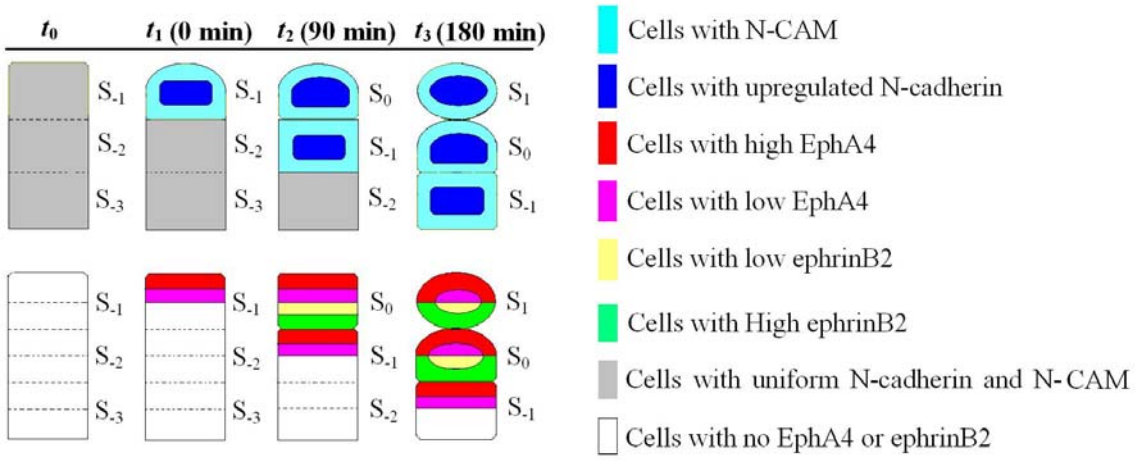

Figure 4.3: Schematic diagram of the spatio-temporal activation of N-cadherin, N-CAM, EphA4 and ephrinB2 during somite segmentation. Upper Panels. At t_0, all cells have uniform N-cadherin and N-CAM levels. At t_1, N-cadherin levels increase in the core of the anterior domain of the PSM (the new somite S_{-1}). At t_2, when the somitic boundary between S_{-3} and S_{-1} starts to form, N-cadherin levels increase in the core of somite S_{-1}. **Lower Panels.** At t_0, no cells have EphA4 or ephrinB2. At t_1 the cells in the anterior compartment of S_{-1} increase their EphA4 level, with a high level in the anterior half of the compartment and a low level in the posterior half. At t_2 the cells in the anterior compartment of the new S_{-1} increase their EphA4 level, with a high level in the anterior half of the compartment and a low level in the posterior half, while the cells in the posterior compartment of S_0 increase their levels of ephrinB2, with a high level in the posterior half of the compartment and a low level in the anterior half. **Both Panels.** At t_3, the somitic boundary forms between S_0 and S_{-1}, and the expression of N-cadherin, EphA4 and ephrinB2 reiterates caudally.

I assume that cells in the PSM initially have the same size. I represent the epithelialization and compaction of the peripheral cells into *epithelial cells*, by increasing the size of peripheral cells and decreasing the size of core cells slightly when a given compartment begins to express either EphA4 or ephrinB2.

At the following cycle (t_2, t_3,…), this entire pattern repeats, shifted posteriorly by one somite length.

4.4 Computer Simulation of Segmentation

4.4.1 Additions to the Glazier-Graner-Hogeweg Model

I implemented my somite segmentation model using the *Glazier-Graner-Hogeweg model* (*GGH*) (see Chapter Three, Section 3.2.2)

In this simulation, the Effective Energy is:

$$H = \sum_{\substack{\vec{\imath},\vec{\imath}' \\ \text{neighbors}}} J\left(\tau(\sigma(\vec{\imath})),\tau(\sigma(\vec{\imath}'))\right)\left(1-\delta(\sigma(\vec{\imath}),\sigma(\vec{\imath}'))\right)+\sum_{\sigma}\lambda\left(V(\sigma(\vec{\imath}))-V_t\left(\tau(\sigma(\vec{\imath}))\right)\right)^2$$

$$+\sum_{\sigma}\beta\left(S(\sigma(\vec{\imath}))-S_t\left(\tau(\sigma(\vec{\imath}))\right)\right)^2, \qquad (4.1)$$

where J is the total adhesion energy per unit surface area between cells of type $\tau(\sigma)$ and $\tau(\sigma')$ (negative for adhesion), V_t the target volume of cells of type τ, V the actual volume of each

cell, λ the strength of the volume constraint (the bigger λ, the smaller the cells' volume fluctuations), S_t the target membrane area for cells of type τ, S the actual membrane area of each cell, and β the membrane elasticity.

I discuss the conversion between MCS and experimental time below.

4.4.2 GGH Somitogenesis Simulation

To translate my model into a GGH simulation, I must define the GGH parameters and their temporal changes for each cell.

Fig. 4.4 shows the initial condition of my two-dimensional rectangular lattice (170 x 450 pixels). I begin with a segment of PSM, with ECM surrounding the PSM in the anterior and lateral directions. The segment of PSM, which extends to the bottom of the lattice, is long enough to allow more than three somites to form and the ECM layer is thick enough that the cells do not interact with the lattice edges in the region of somite formation. The long axis of the rectangle corresponds to the AP axis in the embryo and the short axis to the ML axis. Each cell initially occupies 5 × 5 pixels and each somite contains 20 × 20 cells, which corresponds to the approximately 400 cells in chick somites (Kulesa and Fraser, 2002).

Fig. 4.4 shows the 10 cell types:

1. ECM substrate (a single large generalized cell with unconstrained volume), $\tau = \mathrm{ECM}$.

2. Mesenchymal cells in the posterior PSM with uniform volumes and low background levels of N-cadherin and N-CAM, $\tau = \mathrm{cPSM}$.
3. Epithelial cells in the periphery of the anterior half of the anterior compartments of somites, with increased volumes, high levels of EphA4, background levels of N-CAM and low levels of N-cadherin, $\tau = \mathrm{NCAM}, \mathrm{Eph}_{\mathrm{H}}$.
4. Epithelial cells in the periphery of the posterior half of the anterior compartments of somites, with increased volumes, low levels of EphA4, background levels of N-CAM and low levels of N-cadherin, $\tau = \mathrm{NCAM}, \mathrm{Eph}_{\mathrm{L}}$.
5. Mesenchymal cells in the core of the posterior half of the anterior compartments of somites, with decreased volumes, low levels of EphA4, background levels of N-CAM and high levels of N-cadherin, $\tau = \mathrm{Ncadherin}, \mathrm{Eph}_{\mathrm{L}}$.
6. Epithelial cells in the periphery of the posterior half of the posterior compartments of somites, with increased volumes, high levels of ephrinB2, background levels of N-CAM and low levels of N-cadherin, $\tau = \mathrm{NCAM}, \mathrm{ephrin}_{\mathrm{H}}$.
7. Epithelial cells in the periphery of the anterior half of the posterior compartments of somites, with increased volumes, low levels of ephrinB2, background levels of N-CAM and low levels of N-cadherin $\tau = \mathrm{NCAM}, \mathrm{ephrin}_{\mathrm{L}}$.
8. Mesenchymal cells in the core of the anterior half of the posterior compartments of somites, with decreased volumes, low levels of ephrinB2, background levels of N-CAM and high levels of N-cadherin, $\tau = \mathrm{Ncadherin}, \mathrm{ephrin}_{\mathrm{L}}$.
9. Mesenchymal cells in the anterior region of the PSM corresponding to the core of somite S_{-1}, with their original volumes, background levels of N-CAM and high levels of N-cadherin, $\tau = \mathrm{Ncadherin}$.

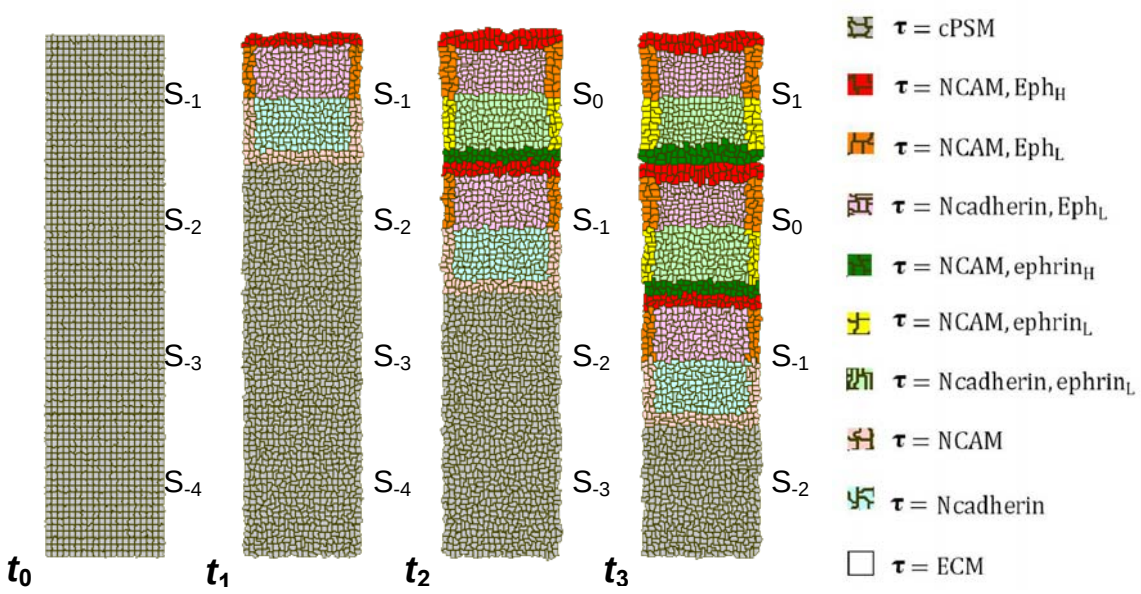

Figure 4.4: Simulated spatio-temporal levels of N-cadherin, N-CAM, EphA4, and ephrinB2 during somitogenesis. At t_0 = 0 MCS, the simulation begins with a regular array of PSM cells expressing background levels of N-CAM and N-cadherin, and surrounded by ECM. At t_1 = 5000 MCS, the N-cadherin level increases in the core of S_{-1} and the N-CAM level increases at the periphery. EphA4 levels increase to High in the anterior half of S_{-1A} and to Low in the posterior half, while the peripheral cells in S_{-1A} grow slightly in volume and the core cells shrink slightly in volume. At t_2 = 7000 MCS this process repeats in the new S_{-1} and the ephrinB2 level increases to High in the posterior half of S_{-0P} and to Low in the anterior half, while the peripheral cells in S_{-0P} grow slightly in volume and the core cells shrink slightly in volume. At t_3 = 9000 MCS, the process repeats for the new S_0 and S_{-1} somites.

10. Mesenchymal cells in the anterior region of the PSM which will correspond to the periphery of somite S_{-1}, with their original volumes, background levels of N-CAM

and low levels of N-cadherin, $\tau = \text{NCAM}$.

A clock controls the temporal distribution of cell types. All cells except the ECM begin as type cPSM. At the beginning of the first somite cycle in the simulation, at t_1, cells in the anterior region of the PSM which I define as beginning as S_{-1A}, change their types from type cPSM to type NCAM, Eph_H, NCAM, Eph_L, or Ncadherin, Eph_L and those in S_{-1P}, change their types from type cPSM to type Ncadherin or NCAM. At the beginning of each succeeding somite cycle, the cells in the new S_{0P} change their types from types Ncadherin or NCAM to types NCAM, ephrin_H, NCAM, ephrin_L, Ncadherin, ephrin_L, cells in S_{-1A} change from type cPSM to type NCAM, Eph_H, NCAM, Eph_L, or Ncadherin, Eph_L and cells in S_{-1P}, change from type cPSM to type Ncadherin or NCAM. Fig. 4.4 shows the spatio-temporal activation of NCAM, N-cadherin, Eph, and ephrin during the simulation, which schematically reproduces the biological pattern in Fig. 4.3.

4.4.2.1 Simulation Implementation

I implemented my simulations using CompuCell3D (see Chapter Three, Section 3.2.3). I provide my simulation code in Appendix 7.G.

4.4.2.2 Parameter Values

My simulation has a substantial number of parameters, most of which are not known quantitatively from experiments. Fortunately, the patterning depends primarily on the

hierarchy of the adhesion energies. Since my primary goals in this chapter are qualitative reproduction of experiments, I retain a good deal of flexibility in choosing parameter values.

4.4.2.3 Global parameters

The parameter T_m determines the intrinsic cell motility and rescales all of the other parameters in the Effective Energy. I am therefore free to fix it and vary the scale of my other parameters or *vice versa*. In this case I fix $T_m = 100$ unless I specify otherwise. I then chose the remaining parameters so that $\Delta H/T_m$ in Eq. (3.8) is neither too large nor too small (typically between about 0.05 and 0.5). If $\Delta H/T_m$ is too small, the cells will not move. If $\Delta H/T_m$ is too large, cells will interact with the lattice, producing unnatural shapes or even falling apart. In principle, I can calculate T_m from experiments measuring the diffusion-constants of cells in the tissue, but these measurements are not yet available for somites. I chose the values of $\beta = 20$ and $\lambda = 20$ for the cell-volume and surface-area constraints to keep surface and volume fluctuations relatively small, without causing cells to stop moving. I present the parameters in Tables 4.1, 4.2 and 4.3.

4.4.2.4 Cell-adhesion energies

I have two types of adhesion in my simulations: cell-ECM adhesion and cell-cell adhesion.

The biology of the somite largely determines my adhesion hierarchy (where I have no information at all, I generally set parameters equal to a default value).

I assume that adhesion between cells with higher levels of N-CAM or N-cadherin is stronger and that both N-CAM and N-cadherin are homotypically adhesive and that N-cadherin is more cohesive than N-CAM:

Table 4.1: Initial and target values for surface areas and volumes of specific cell types in my somitogenesis simulations.

τ	λ	Initial V	Biological Value (μm^2)	V_t	Biological Value (μm^2)	β	S	S_t
ECM	0	N/A	N/A	N/A	N/A	0	N/A	N/A
NCAM	20	25	100	25	100	20	20	20
Ncadherin	20	25	100	25	100	20	20	20
NCAM, Eph_H	20	25	100	36	144	20	20	24
NCAM, Eph_L	20	25	100	36	144	20	20	24
Ncadherin, Eph_L	20	25	100	16	64	20	20	16
NCAM, $ephrin_H$	20	25	100	36	144	20	20	24
Ncadherin, $ephrin_L$	20	25	100	16	64	20	20	16
NCAM, $ephrin_L$	20	25	100	36	144	20	20	24
cPSM	20	25	100	25	100	20	20	20

Table 4.2: Global parameters in my somitogenesis simulations.

	Simulation Value	Biological Value
T_m	100 MCS	(no comparable value)
t_1	5000 MCS	0 minutes
t_2	7000 MCS	90 minutes
t_3	9000 MCS	180 minutes
t_{total}	15,000 MCS	(no comparable value)
Δ	7.0	14 μm

Table 4.3: Initial adhesion energies for mesenchymal and epithelial cell sorting during somitogenesis. *m*, mesenchymal cell class, *e*, epithelial cell class.

τ	ECM	NCAM	Ncadherin	NCAM, Eph_H	NCAM, Eph_L	Ncadherin, Eph_L	NCAM, $ephrin_H$	Ncadherin, $ephrin_L$	NCAM, $ephrin_L$	cPSM
τ ***Class***		*m*	*m*	*e*	*e*	*e*	*e*	*e*	*e*	*m*
ECM	0	15	15	15	15	15	15	15	15	15
NCAM		-20.25	-24	-20.25	-20.25	-24	-20.25	-24	-20.25	-20.25
Ncadherin			-38.44	-24	-24	-38.44	-24	-38.44	-24	-38.44
NCAM, Eph_H				-20.25	-20.25	-24	-20.25	-24	-20.25	-20.25
NCAM, Eph_L					-20.25	-24	-20.25	-24	-20.25	-20.25
Ncadherin, Eph_L						-38.44	-24	-38.44	-20.25	-38.44
NCAM, $ephrin_H$							-20.25	-24	-20.25	-20.25
Ncadherin, $ephrin_L$								-38.44	-24	-38.44
NCAM, $ephrin_L$									-20.25	-20.25
cPSM										-20.25

For my two classes of *epithelial* (*e*) and *mesenchymal* (*m*) cells surrounded by ECM, I need an initially-random mixture of the two cell types to sort stably, with the epithelial cells at the surface and mesenchymal cells condensing in the core, which requires the following relations among the adhesion energies (Glazier and Graner, 1993):

$$J(\mathrm{m},\mathrm{m}) < \frac{J(\mathrm{m},\mathrm{m}) + J(\mathrm{e},\mathrm{e})}{2} < J(\mathrm{m},\mathrm{e}) < J(\mathrm{e},\mathrm{e}), \tag{4.2}$$

To prevent cells dispersing into the ECM, rather than sticking together, requires that (Glazier and Graner, 1993):

$$J(\mathrm{e},\mathrm{e}) < J(\mathrm{e},\mathrm{ECM}) \leq J(\mathrm{m},\mathrm{ECM}), \tag{4.3}$$

to prevent cells from dispersing into the ECM, I set J(cell, ECM) = 15 initially. The interaction energy per unit contact length between cells includes both adhesion and effective repulsion. Binding between EphA4 and ephrinB2 on apposing cells reduces the effective adhesion (increases J) by an *Effective Repulsion Energy*, J_r, compared to the adhesion energy, J_a, which I would predict based on the number and type of cell-adhesion molecules. The decrease in adhesion need not scale linearly with the number of bound Eph/ephrin pairs. The simplest approximation to such an effect is to write the net adhesion, J, as a sum of the adhesion and repulsion alone plus a bilinear perturbation of strength c:

$$J(\tau_1,\tau_2) = J_a(\tau_1,\tau_2) + J_r(\tau_1,\tau_2) + cJ_a(\tau_1,\tau_2)J_r(\tau_1,\tau_2). \tag{4.4}$$

When c is positive, the interaction weakens adhesion compared to the additive case. When c is negative, the interaction strengthens adhesion compared to the additive case.

Additionally, cells expressing EphA4 should not mix with cells expressing ephrinB2. In this case, the energy for cell-cell interaction with repulsion must be larger than cell-cell interaction with adhesion:

$$J(\mathrm{Eph},\mathrm{cadherin},\mathrm{ephrin},\mathrm{cadherin}) > \frac{J(\mathrm{Eph},\ \mathrm{cadherin},\mathrm{ECM}) + J(\mathrm{ephrin},\ \mathrm{cadherin},\mathrm{ECM})}{2} = \frac{J(\mathrm{cadherin},\mathrm{ECM}) + J(\mathrm{cadherin},\mathrm{ECM})}{2}. \tag{4.5}$$

Since domains of EphA4 and ephrinB2 separate but remain compact as the ECM furrow forms between them, the ECM must engulf both domains:

$$J(\text{Eph}, \text{cadherin}, \text{Eph}, \text{cadherin}) < J(\text{Eph}, \text{cadherin}, \text{ECM}),$$

$$J(\text{ephrin}, \text{cadherin}, \text{ephrin}, \text{cadherin}) < J(\text{ephrin}, \text{cadherin}, \text{ECM}). \quad (4.6)$$

4.4.2.5 Target areas and volumes

In two dimensions, the ratio of a cell's target membrane area squared to its target volume determines how "floppy" the cell is. If the ratio is small, cells will be round and stiff; in the opposite limit, cells will be floppy and extended like an uninflated beach ball.

4.4.2.6 Time

The conversion between MCS and experimental time depends on the average values of $\Delta H/T_m$, and hence on the choices of parameters. I make this assignment empirically, by observing the time in MCS that somite reorganization takes after I switch on the pattern of N-CAM, N-cadherin, EphA4 and ephrinB2 and set it to the corresponding experimental time. For the values of parameters I have chosen, 2000 MCS = 90 minutes (or 1 MCS = 2.7 seconds).

Because my initial configuration uses non-biological, rectangular cells, I set t_0 = 5000 MCS to allow the PSM to relax before I turn on the initial pattern of N-CAM and N-cadherin. Since the somitic clock interval is 2000 MCS, t_1 = 7000 MCS, t_2 = 9000 MCS, and so on.

4.5 Results and Discussion

4.5.1 Parameter Choices

All viable developmental mechanisms must be relatively insensitive to fluctuations in key parameters. Biochemical redundancy is one source of such robustness. My model lacks such redundancy. However, even reasonable agreement with experiment would be unsatisfactory if it required very tight parameter tuning. Instead, I expect that a viable model will have a relatively broad range over which parameters have relatively little effect on segmentation. I therefore conducted parameter sweeps to explore parameter dependencies and optimize my choices.

Fig. 4.5 shows the long-time morphologies (t = 10,000 MCS) for cell motility T_m between 50 and 200 and repulsion energy J_r between 20 and 60. For very high cell motility $T_m \geq 150$ (Figs. 4.5A1-A5), coherent somites fail to form. Similarly, if the effect of EphA4/ephrinB2 binding is too weak ($J_r < 50$), the simulation does not form a clear intersomitic boundary. Only for strong repulsion ($J_r = 60$) and low motility ($T_m \leq 100$) does the somitic furrow form (Figs. 4.5C5 and 4.5D5). Thus, the sensitivity to motility is fairly low (I can vary T_m by a factor of 2), but the sensitivity to variations in repulsion strength requires further study.

4.5.2 Segmentation Requires EphA4/ephrinB2 Repulsion

Fig. 4.6A shows the long-time configuration (t = 10,000 MCS) of a simulation in the absence of EphA4 and ephrinB2. The epithelial cells from different somites and mesenchymal cells from the anterior and posterior domains of each somite mix. Segmentation fails, as is observed in experiments in zebrafish which lack EphA4 (Barrios *et al.,* 2003).

4.5.3 Segmentation Requires Multiple Levels of EphA4/ephrinB2 Expression

I now explore the effect of EphA4/ephrinB2 repulsion on segmentation.

My model includes two non-zero levels of EphA4 and ephrinB2: *High* and *Low*. I define J_{rHH} to be the repulsion energy between a cell with a high level of EphA4 and a cell with a high level of ephrinB2, J_{rHL} to be the repulsion energy between a cell with a high level of EphA4 and a cell with a low level of ephrinB2 or between a cell with a low level of EphA4 and a cell with a high level of ephrinB2, and J_{rLL} to be the repulsion energy between a cell with a low level of EphA4 and a cell with a low level of ephrinB2.

First, I test whether correct segmentation requires two levels of EphA4 and ephrinB2 expression within each somite compartment. I assume an additive relation between adhesion and repulsion (c = 0 in Eq. (4.4)) and that levels of EphA4 and ephrinB2 are uniform, $J_{\mathrm{rHH}} = J_{\mathrm{rLL}} = J_{\mathrm{rHL}} = 60$. Fig. 4.6B shows that an intersomitic furrow (⇨) forms correctly. However

an obvious intrasomitic notch (→) develops between the anterior and posterior somite compartments, which does not occur in normal somite segmentation. Therefore, correct segmentation appears to require multiple levels of EphA4 and ephrinB2.

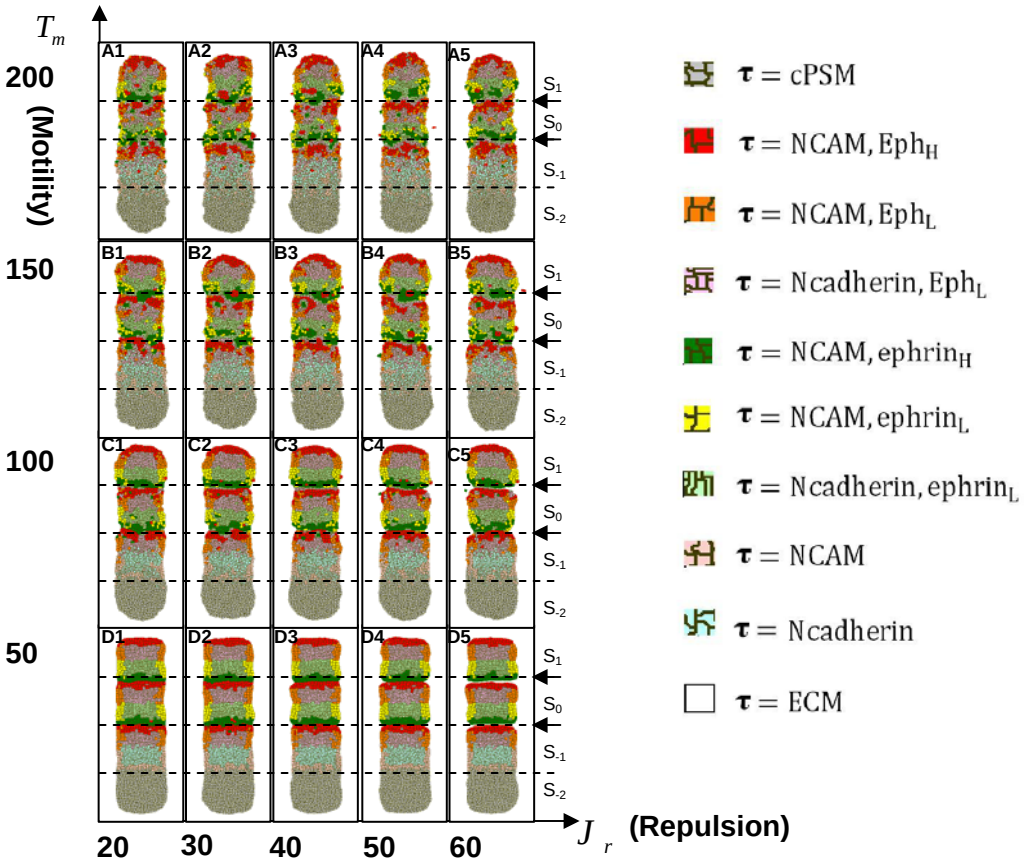

Figure 4.5: Morphologies of somites for different cell motilities and EphA4/ephrinB2 repulsion strengths. Arrows (→) mark intersomitic boundaries. **A1-A5**, **B1-B5.** For very high motilities, coherent somites do not form. **C1-C3, D1-D2.** Weak repulsion does not produce sharp intersomitic boundaries. **C5, D5.** Segmentation with somite separation requires strong repulsion and limited cell motility. All simulations are shown after 15,000 MCS.

Next, I assume that the effect of the higher level of expression of EphA4 and ephrinB2 in the somite and PSM periphery results in effective repulsion energies of $J_{rHH} = J_{rHL} = 3J_{rLL} = 60$, still assuming an additive relation between adhesion and repulsion ($c = 0$ in Eq. (4.4)). Fig. 4.6C shows that an intersomitic furrow (⇨) forms correctly. A very small intrasomitic notch (➔) develops between the anterior and posterior somite compartments, as is observed experimentally. The resulting morphology is very close to normal somite segmentation.

Now I examine the effect of the bilinear term on the final pattern morphology. I assume a cooperative relation between adhesion and repulsion ($c = 1/50$ in Eq. (4.4)) and assume that high and low levels of EphA4 and ephrinB2 are equal: $J_{rHH} = J_{rLL} = J_{rHL} = 60$. Even this small perturbation greatly changes the morphology from Fig. 4.6B. Fig. 4.6D shows that an intersomitic notch forms (⇨) but the somites do not separate. Somewhat surprisingly, the size of the intrasomitic notch (➔) is much smaller. Again, correct somite formation seems to require multiple levels of EphA4 and ephrinB2.

Finally, I assume a cooperative relation between adhesion and repulsion ($c = 1/50$ in Eq. (4.4)) and that the effect of the higher level of expression of EphA4 and ephrinB2 in the somite and PSM periphery results in effective repulsion energies of $J_{rHH} = J_{rHL} = 3J_{rLL} = 60$, as in Fig. 4.6C. Fig. 4.6E shows only a slight intersomitic notch (⇨) and no intrasomitic notch (➔). As in Figs. 4.6A and 4.6D, the somites do not separate.

Thus I will use additive repulsion ($c = 0$) at two levels, with $J_{rHH} = J_{rHL} = 3J_{rLL} = 60$ for my remaining simulations if I do not specify otherwise.

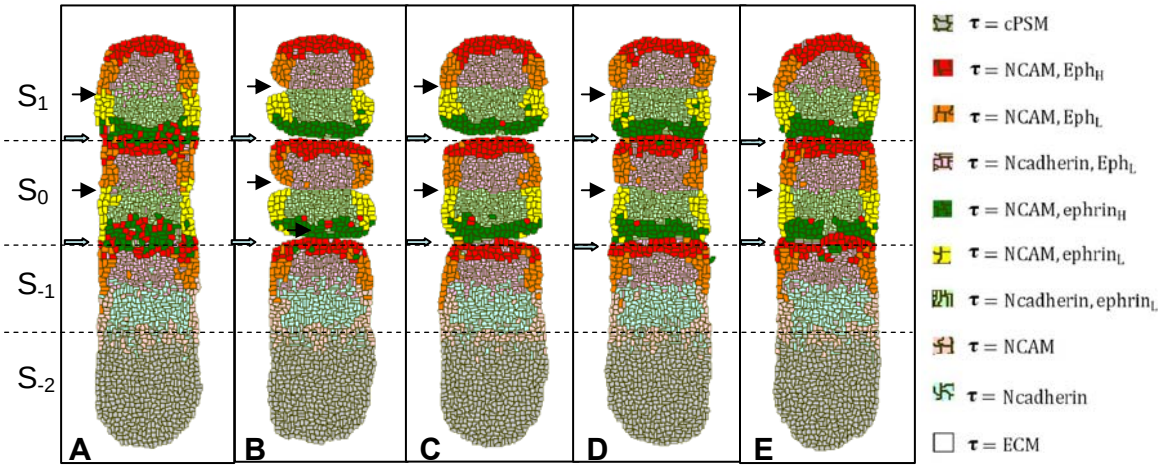

Figure 4.6: Effects of adhesion/repulsion coordination on somite morphology. Heavy arrows (⇨) mark intersomitic boundaries. Light arrows (→) mark intrasomitic compartment boundaries. **A.** Without EphA4 and ephrinB2, cells mix between the posterior of a somite and the anterior of the following somite. **B.** Linear interaction of adhesion and repulsion with uniform repulsion results in both intersomitic and intrasomitic separation. **C.** Linear interaction of adhesion and repulsion with graded repulsion results in intersomitic separation without intrasomitic separation. **D.** Weak nonlinear interaction of adhesion and repulsion with uniform repulsion results in both intersomitic and intrasomitic segmentation. **E.** Nonlinear interaction of adhesion and repulsion with graded repulsion results in intersomitic segmentation without intrasomitic segmentation. All simulations are shown after 15,000 MCS

The Takeichi group (Horikawa *et al.,* 1999) has observed the separation of the anterior and posterior somite compartments during somite formation in N-cadherin (-/-) mouse embryos. I removing N-cadherin from my simulation. I kept the repulsion at the same levels as the

simulated this experiment by setting the adhesion energy for cell types expressing N-cadherin equal to the adhesion energy for the corresponding cell type expressing N-CAM, effectively values used for Fig. 4.6B. I observed both intersomitic (⇨) and intrasomitic (→) furrows as seen in Fig. 4.7D. Thus N-cadherins seem essential to keeping the two compartments of a somite fused during segmentation.

4.5.4 Dynamic Morphological Changes and Error Correction during Segmentation

Time-lapse movies of shape changes during segmentation show intriguing effects (Kulesa and Fraser 2002) (Figs. 4.8A-F). In particular, the boundary between S_0 and S_{-1} forms a characteristic *ball-and-socket* or *W* shape (Fig. 4.8C), with the groove between S_0 and S_{-1} first opening up at the dips of the W, followed by the arms of the W retracting and sometimes folding inwards. Initially, the PSM envelops the forming somite, forming a *sleeve*. During segmentation, the sleeve cells fold back into the PSM along the S_0-S_{-1} boundary and the somite eventually rounds up.

One way to reproduce this dynamics would be for the PSM to cohere more to ECM than other cell types, *i.e.*, J(cPSM, ECM) < J(other cell type, ECM), in which case I expect that PSM cells will partially surround the S_0 somite. A possible mechanism for such behavior would be a reduction in membrane levels of integrins in the posterior compartments of S_{-1} and later (S_0, S_1,…) somites.

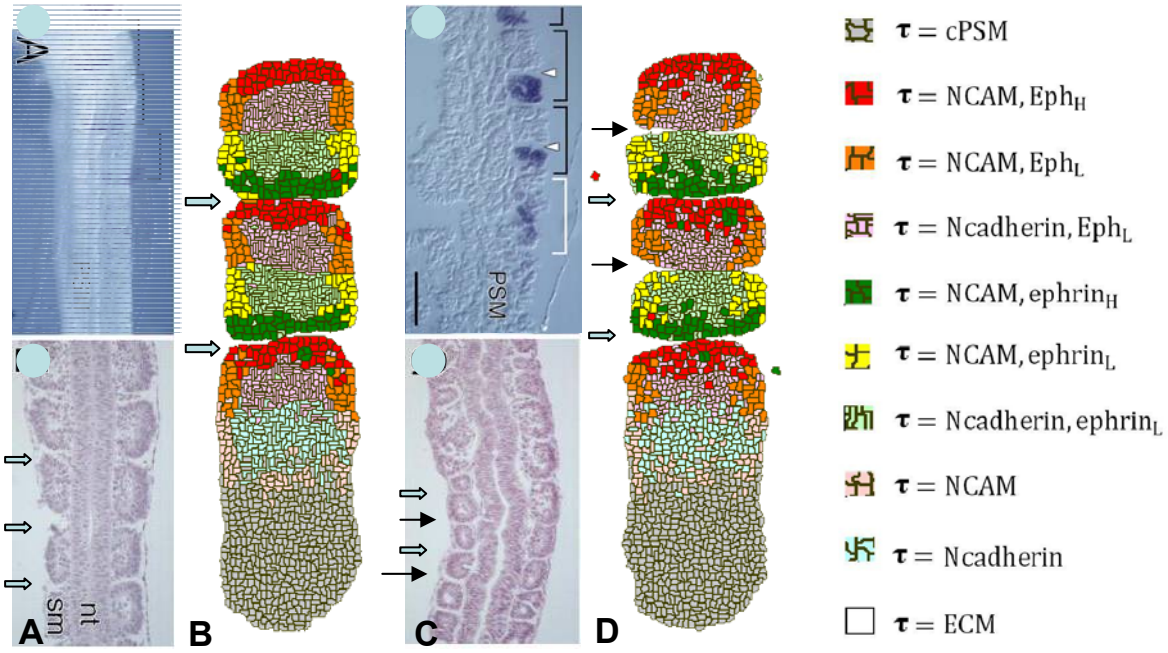

Figure 4.7: Comparison of somite structures in wild-type and N-cadherin-knockout experiments and simulations. Heavy arrows (⇨) mark intersomitic boundaries. Light arrows (→) mark intrasomitic compartment boundaries. **A.** Experimental wild phenotype (adapted from Horikawa *et al.,* 1999). **B.** Simulated wild phenotype after 15,000 MCS. **C.** Experimental N-cadherin-double-knockout phenotype (adapted from Horikawa *et al.,* 1999). The somites separate into *Uncx4.1*[2]-positive and *Uncx4.1*-negative regions. *Uncx4.1* is a specific marker for the posterior compartments of somites. **D.** Simulated N-cadherin-double-knockout phenotype at 10,000 MCS. Both somites and somite compartments separate.

[2] Gene names are given in italics.

In Figs. 4.8G-L, a black arrow (→) marks intersomitic boundaries (corresponding to the white arrow in Figs. 4.8A-B). During the clock cycle before segmentation proper, and thus before the initiation of ephrinB2 expression in S_{-1} (Figs. 4.8G-H), as in the experiment, I observe anterior cells at the sides of S_{-2} move anteriorly and wrap around the posterior end of S_{-1}. During the following clock cycle (Figs. 4.8I-J), the appearance of ephrinB2 in S_{0P} (formerly S_{-1P}) causes the formation of a W-shaped intersomitic furrow between S_0 and S_{-1}, as in Figs. 4.8C-D. During the following cycle, the wings of the W retract and the somite rounds up (Figs. 8K-L and 8E-F). The details of the retraction differ somewhat from the experiment, with the wings of the W retracting but not folding inwards, as is seen in some experiments.

Because biological signaling is noisy, some cells will slightly misread the somitic clock during determination. As a result they will differentiate inappropriately for their location (*misdifferentiate*). Such misdifferentiation occurs primarily near compartment boundaries, where cells are near a biological threshold between differentiation states and a small amount of noise can throw the switch. Kulesa and Fraser may have observed such effects in their movies, where cells initially on one side of the presumptive intersomitic boundary cross the boundary during segmentation (Kulesa and Fraser, 2002). The white and black dots in Figs. 4.8A-F denote cells that are not simply carried along as the W extends and retracts, but actually cross from S_{-2} to S_{-1} and from S_{-1} to S_{-2} respectively.

My simulations show that adhesion-based cell-sorting provides a viable mechanism for the correction of minor errors in differentiation. In my simulation in Figs. 4.8G-L, I have allowed

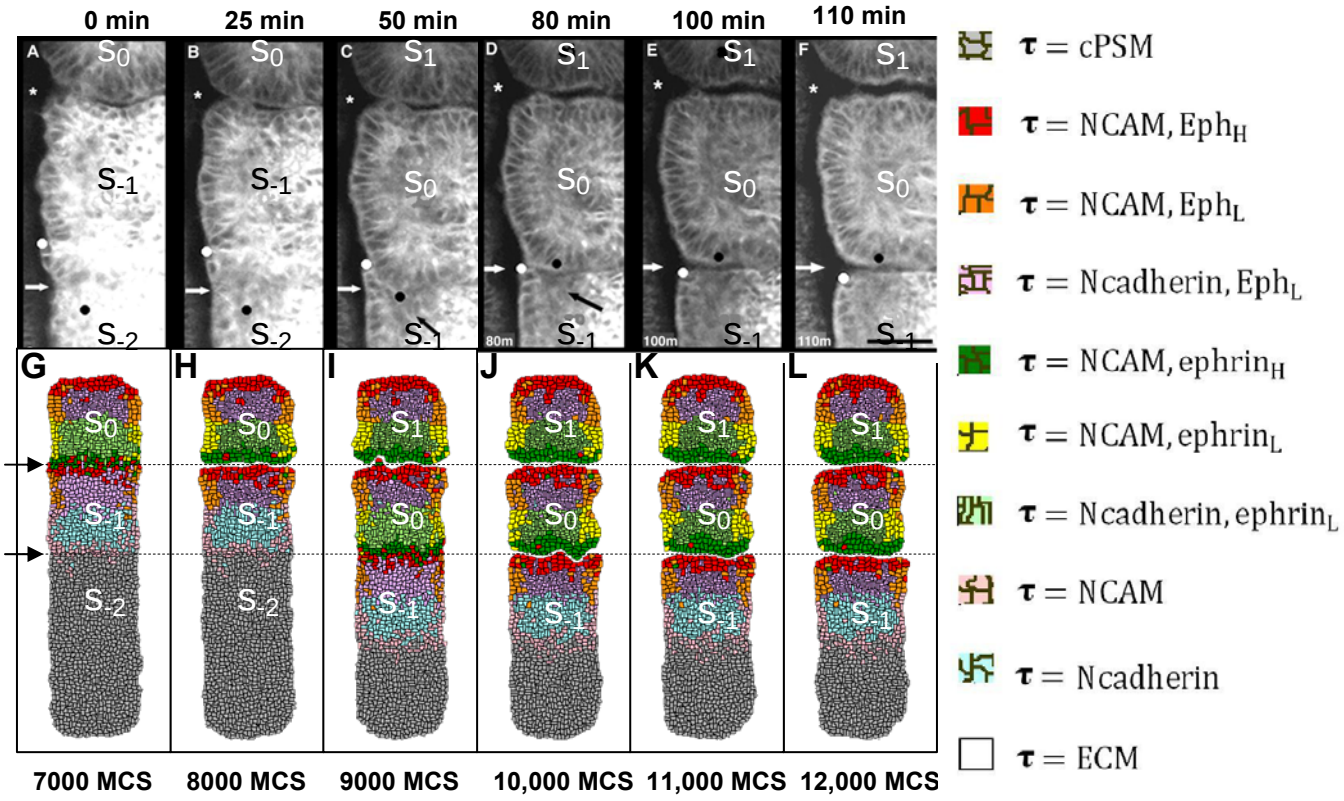

Figure 4.8: Simulated and experimental somite segmentation dynamics. A-F. Confocal time-lapse images of vitally-stained tissue (adapted from Kulesa and Fraser, 2002). White arrows indicate intersomitic boundaries. The white and black dots label cells which cross the presumptive boundary. **G-L.** Simulated somite segmentation with preferential adhesion between PSM and ECM and AP indeterminacy of somite differentiation. Black Arrows (→) mark intersomitic boundaries. Scale bar in experimental image 8F is 50 μm and $J_{rHH} = J_{rHL} = 3J_{rLL} = 80$.

for misdifferentiation by having each cell read its AP position with a small error chosen from a Gaussian distribution with a *width*, Δ, of 14 microns when it selects its type, making the

initial compartment boundaries blurry. Thus, some cells in S_{0P} assume types (red) that should be in S_{-1A}, *etc*... If I follow these red cells during their subsequent time evolution (Figs. 4.9 A-C), I find that adhesion-driven cell sorting causes most (though not all) of them to cross into the correct compartment, in a manner identical to that in the experiments. The greater the cell motility compared to the rate of furrow formation, the more complete the correction.

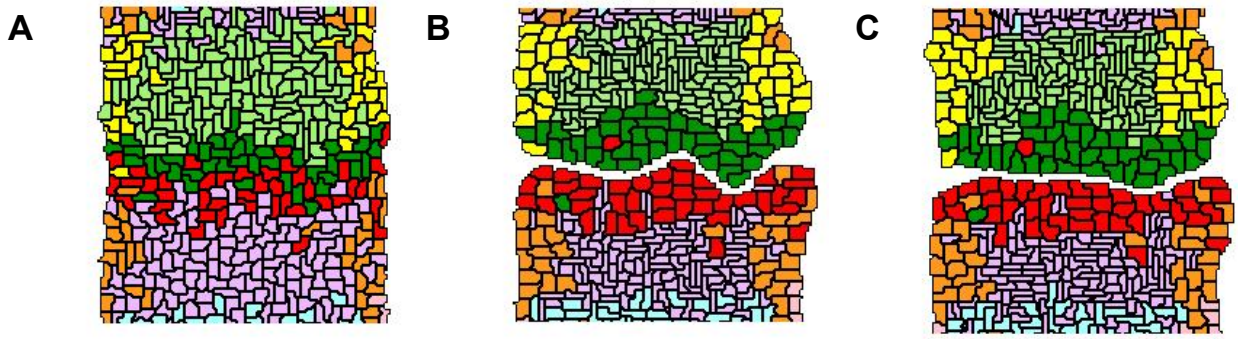

Figure 4.9: Detail of boundary crossing of misdifferentiated cells from Fig. 4.8. A. 9000 MCS. **B.** 10,000 MCS. **C.** 11,000 MCS.

4.6 Conclusion

In this chapter, I have shown that multilevel homotypic adhesion and heterotypic repulsion can reproduce many of the phenomena of normal somite segmentation, including the ball-

and-socket dynamics and compartment crossing by misdifferentiated cells. Simulated N-cadherin knockouts produce an intrasomitic furrow as observed in experiments.

CHAPTER FIVE

EFFECTS OF FGF4 AND FGF8 ON CHONDROGENIC PERIODICITY AND CELL DIVISION IN CHICK-FORELIMB MICROMASS CULTURE

Abstract

During vertebrate limb development, multiple fibroblast growth factors (*FGF*s) interact with other factors to regulate limb outgrowth and chondrogenic patterning[3]. While some FGFs may be redundant during limb development, the multiple *fgf* genes and FGF proteins differ subtly from each other in their expression patterns and/or receptor-binding specificities, suggesting that many FGFs could have distinct functions. To investigate the differences between two key FGFs, FGF4 and FGF8, in regulation of limb outgrowth and patterning, I used chick-limb micromass culture as an *in vitro* model and analyzed cell division and chondrogenesis under different concentrations of exogenous FGFs. To examine the roles of FGF4 and FGF8, I quantitatively assayed chick-forelimb micromass cartilage patterns and average cell-division rates in response to FGF4 and/or FGF8 treatment. Since FGF4 and FGF8 co-express in the posterior limb *Apical Ectoderm Ridge* (*AER*) (Martin, 1998), I also explored micromass patterning under simultaneous application of FGF4 and FGF8, which

[3] Here, "FGF" stands for an FGF protein, "*fgf*" stands for an *fgf* gene.

caused pattern changes different from the simple combination of the effects of FGF4 and FGF8. Both carboxyfluoroscein-succinimidyl-ester (*CFSE*) staining to measure rates of cell-division within the cultures and flow cytometry showed that the cell-division rate increased roughly linearly with the concentration of FGF4 and FGF8 over the range 12.5 ng/ml—100 ng/ml. FGF4 enhances cell division more than FGF8 does at the same concentration. I then explain the different effects of FGF4 and FGF8 on chondrogenic patterning and cell proliferation based on published receptor-binding specificities. The effects of these FGFs may result from partial overlap of their downstream signaling pathways. I also propose a model for the roles of FGF4 and FGF8 during limb outgrowth and chondrogenesis: The distal and posterior cells in the limb bud divide more frequently due to high levels of expression of FGFs in the distal-posterior domain and their descendants contribute a greater fraction of the final volume of the limb than the descendants of cells in other areas.

5.1 Introduction

5.1.1 Limb Development

Vertebrate limb outgrowth and patterning depend on the establishment and maintenance of three signaling centers within the limb bud: (1) the *apical ectodermal ridge* (*AER*), an epithelial structure running from the anterior to the posterior of the distal margin of the bud; (2) the *zone of polarizing activity* (*ZPA*) in the mesenchyme at the posterior of the bud, which expresses diffusible *Sonic Hedgehog* (*Shh*); (3) nonridge ectoderm. Elimination of the AER

prevents subsequent proximo-distal growth. Diffusible FGFs define AER function, connect signaling centers and can compensate for an excised AER (Niswander *et al.,* 1993; Vogel and Tickle 1993; Niswander *et al.,*1994; Vogel *et al.,* 1995; Hara *et al.,* 1998; Martin, 1998; Lewandoski *et al.,* 2000; Sun *et al.,* 2002; Sanz-Ezquerro and Tickle 2003). Grafting the ZPA to the anterior side of a host limb bud results in mirror-image duplication of the posterior limb. Shh is responsible for anterior-posterior limb patterning and can compensate for an excised ZPA (Tickle *et al.,* 1997).

5.1.2 Roles of FGFs and their Receptors during Limb Development

FGFs belong to a large family (at least 22 members) of growth factors (Zhang *et al.,* 2006). Developing chick limb expresses five FGF genes, *fgf2, fgf4, fgf8, fgf9, and fgf10* (*fgf17* in mouse) (Martin, 1998), and four *fibroblast-growth-factor receptors* (*FGFR*). FGFR1 and FGFR2 play roles in early limb development (Deng *et al.,* 1997; Xu *et al.,*1998; Li *et al.,* 2005). The AER expresses *fgf2, fgf4, fgf8,* and *fgf9*, and the mesencyme underlying the AER expresses *fgf2* and *fgf10* (Martin, 1998).

5.1.3 Importance of FGF4 and FGF8

Although removal of AER truncates limb growth (Martin, 1998), ectopic FGF1, FGF2 (Savage and Fallon 1995), FGF4 (Niswander *et al.,* 1993), FGF8 and FGF10 (Martin, 1998)

can rescue limb growth. Paradoxically, knockout of *fgf2*, *fgf4* (Moon *et al.,* 2000; Sun *et al.,* 2000), *fgf9* (Lewandoski *et al.,* 2000), or *fgf17* (Xu *et al.,* 2000) individually has no effect on limb development. Inactivation of *fgf8* results in a small limb (*hypoplasia*) (Sun *et al.,* 2002; Lu *et al.,* 2006). In the absence of both FGF4 and FGF8 activity, limb development fails (Sun *et al.,* 2002). FGF8 signaling from the AER forms a positive feedback loop with FGF10 in the underlying mesenchyme, which is essential for limb initiation, outgrowth and patterning (Lewandoski *et al.,* 2000). *fgf4* RNA localizes to the posterior AER and establishes a positive feedback loop with *Shh* in the ZPA (Niswander *et al.,* 1994). Thus, both FGF4 and FGF8 are essential to proximo-distal and antero-posterior growth and patterning.

5.1.4 Micromass Cell Culture

Chondrogenic mesenchymal condensation in chick-limb-mesenchyme micromass cultures provides an *in vitro* model for limb growth, which allows exploration of morphogens' effects on cartilage patterning and limb growth using *serum-free defined media* (*SFDM*, Paulsen and Solursh, 1988) and in the absence of external cues from the non-AER ectoderm, body flank, AER and ZPA. At the cellular level, micromass cultures exhibit chondrogenic condensations similar to those in limb mesoblast *in vivo*, although the random spot-stripe patterns that form *in vitro* lack the controlled architecture of the developing limb bud.

5.2 Materials and Methods

5.2.1 Micromass Cell-Culture Techniques

Micromass cell-culture experiments use pools of mesenchymal tissue isolated from the distal 0.2 mm of Hamburger and Hamilton (*HH*) (Hamburger and Hamilton, 1992) stage 24-25 wing buds of *White Leghorn* embryos (Purdue University, West Lafayette, IN) (Downie and Newman, 1994, 1995). This tissue is free of myoblasts and myogenic precursors (Newman *et al.,* 1981). I treated the limb tip with 10mM EDTA for 20 minutes at 37°C to remove the ectoderm cells (Downie and Newman, 1994). The cultures therefore consisted almost entirely of mesenchymal cells. I plated cells at 1.75×10^5 per 10 µl spot on 24-well plates (Costar Cat. No. 3526) with DMS (90% DM[4] with 10% Fetal bovine serum (*FBS*) and antibiotics). I added Serum-free defined medium (Paulsen and Solursh, 1988) (60% Ham's F12, 40% DMEM, 5 µg/ml insulin, 10 nM hydrocortisone, 50 µg/ml L-ascorbic acid (to enhance chondrogenesis), 5 µg/ml chicken transferrin (a blood plasma protein for iron-ion delivery) and antibiotics) into each well. I then added FGF4 (R & D Systems, molecular weight 16 KD), FGF8 (R & D Systems, molecular weight 23 KD) or a combination of the two at concentrations of 12.5, 25, 50, or 100 ng/ml. This range covered those reported to change chondrogenesis patterning (Moftah *et al.,* 2002). Cells attached to the plates after 45 minutes. I replaced the old medium with fresh SFDM after 48 hours, and daily thereafter. I fixed cultures after 6 days and stained them for cartilage matrix with Alcian blue at pH 1.0

[4] DM–60% Ham's F12 and 40% Dulbecco's Modified Eagle's Medium (*DMEM*).

(Downie and Newman, 1994; Moftah *et al.,* 2002). I visualized and recorded the cartilage patterns using a Nikon binocular dissection microscope at 1.5 × with a double fiber-optic side light and calibrated the length scale of the images with a micrometer under the same magnification.

5.2.2 Image Analysis

5.2.2.1 Measurement of the Average Interval

To measure the periodicity of the chondrogenic patterns, I used the *Average Interval*, L_A, the mean distance between neighboring peaks (center lines of the chondrogenic areas) or between the spot centers (Fig. 4.1), computed using the *peak-length* method (Miura *et al.,* 2000; Kiskowski *et al.,* 2004), which defines the average peak interval to be twice the total number of pixels in the region of interest (*ROI*) divided by the number of pixels that contain *peaks* (center lines of chondrogenic areas) and *valleys* (center lines of nonchondrogenic areas):

$$L_A \equiv \frac{\text{Number of total pixels} \times 2}{\text{Number of peak and valley pixels}}, \tag{5.1}$$

This method is independent of the size of the chondrogenic condensations and the types of chondrogenic patterns (*i.e.,* spots or stripes) (Miura *et al.,* 2000, 2006; Kiskowski *et al.,* 2004) as long as the chondrogenic and nonchondrogenic areas are separated. I implemented

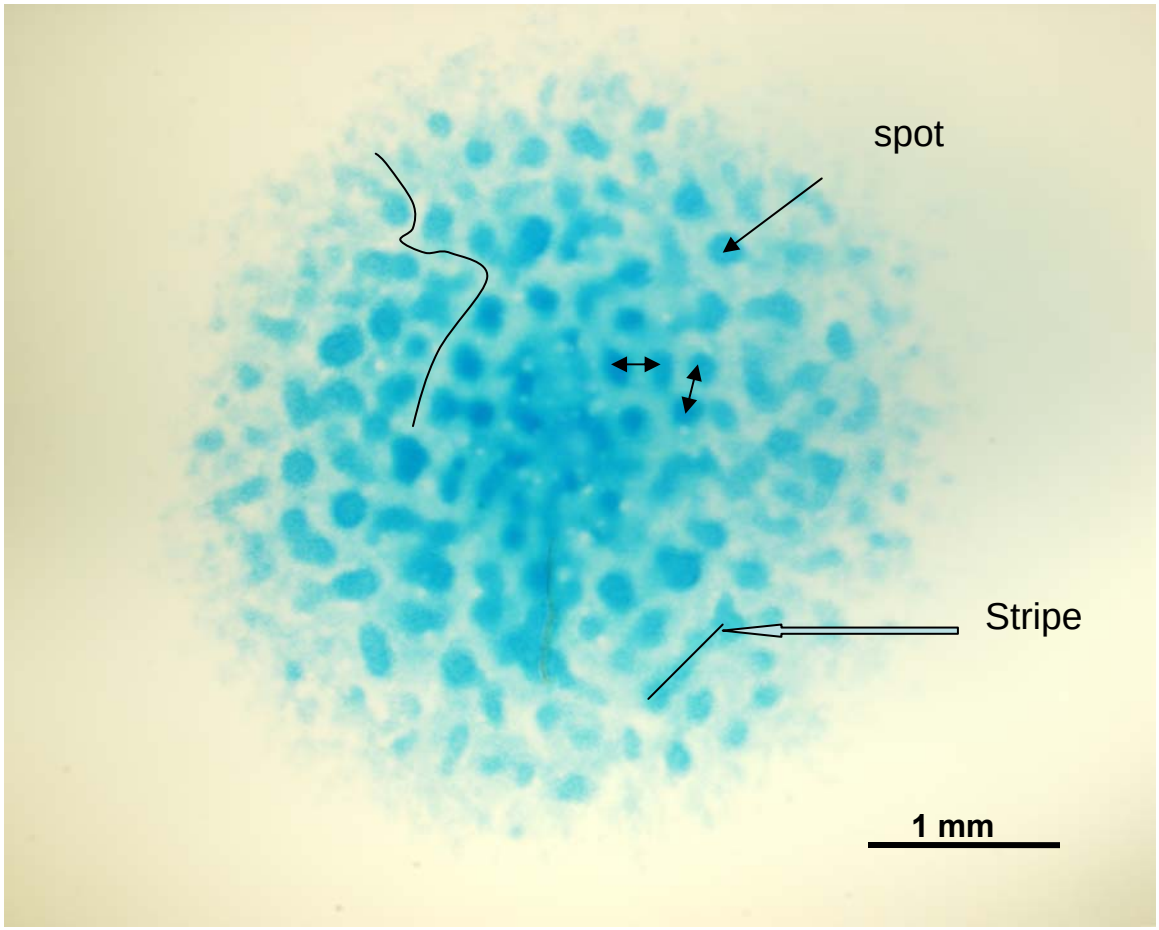

Figure 5.1: Typical limb-cell micromass-culture image. The chondrogenic domains are stained by Alcian blue. The thick arrow points to a stripe. The thin arrow points to a spot. The black curve indicates a valley line, which is the center line of a nonchondrogenic area between chondrogenic spots or stripes. Another black line indicates a peak line, which is the center line of a chondrogenic stripe. The double arrows show the distances between centers of chondrogenic spots and between peak lines.

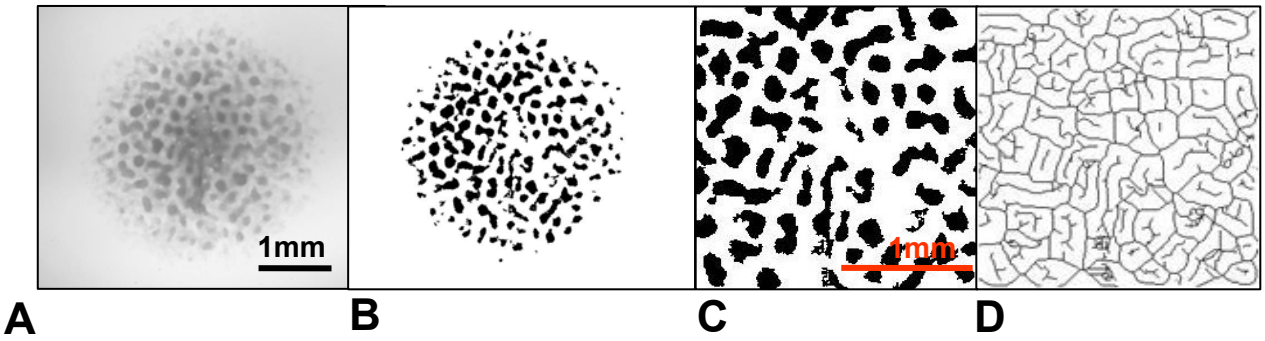

Figure 5.2: Image processing to compute the average interval between clusters using the peak-length method. A. A gray-scale image of an Alcian-blue-stained micromass culture. **B.** Binary-thresholded image of A, showing well-separated chondrogenic and nonchondrogenic areas. **C.** Detail of B (250 × 250 pixels). **D.** Peak (chondrogenic) and valley (nonchondrogenic) lines marking the center lines of chondrogenic and nonchondrogenic areas in C.

the algorithm described in Miura *et al.,* and Kiskowski *et al.,* (Miura *et al.,* 2000, 2006; Kiskowski *et al.,* 2004) using ImageJ software, specifically for Alcian-blue-stained micromass culture (see Appendix 7.D for the detailed operation procedure and Macro code).

1) I first segregated chondrogenic from non-chondrogenic areas in the gray-scale image (Fig. 5.2A) by background subtraction using a 'rolling ball' of size 10 pixels (27 × 27 μm^2) to produce the results in Fig. 5.2B. The main idea of the 'rolling ball' algorithm is to apply a local threshold to optimally remove the surrounding noise (for details on the algorithm, see documentation for the ImageJ package at http://rsb.info.nih.gov/ij).

2) I then generated a binary image using the 'Particle Analysis' operation in ImageJ (See Appendix 7.D) and selected for any chondrogenic area bigger than 10 pixels (27×27 μm^2).

3) Finally, I selected a region of interest (100 × 100 or 250 × 250 pixels), skeletonized both the primary binary image (shown in Fig. 5.2C) and its inverted image, and counted the number of peak and valley pixels. Fig. 5.2D illustrates the peak and valley lines for the selected region in Fig. 5.2C.

5.2.2.2 Measuring the integrated density of Alcian-blue staining

The *chondrogenic degree* is normally determined by measuring the density of extracted Alcian-blue stain from the micromass culture (Downie and Newman, 1994, 1995). I used image analysis to integrate the Alcian-blue density over the two-dimensional micromass image to estimate the degree of chondrogenesis. I converted the RGB image into a gray-scale image and inverted it, so regions with strong Alcian-blue staining had large gray-scale values. I then subtracted the background intensity using the rolling ball algorithm in ImageJ (see Appendix 7.E for code). This algorithm reduces background noise and maintains initial differences in intensity. I then integrated the intensity over the whole image using ImageJ (see Appendix 7.E for code). I further defined the *cartilage-fraction ratio* as the *integrated Alcian-blue staining* (*IS*) divided by the *total micromass area* (*TA*). To minimize differences between runs, I normalized IS and TA for test samples by dividing them by the IS or TA

values for SDFM-treated samples. I use the *normalized cartilage-fraction ratio* (*NCFR*) to stand for the chondrogenic degree:

$$NCFR = \frac{\sum IS_{\text{sample}} / \sum IS_{\text{SDFM}}}{\sum TA_{\text{sample}} / \sum TA_{\text{SFDM}}}, \tag{5.2}$$

where the sum is over three different runs.

Similarly, in order to check for changes in average nodule size, I used ImageJ to measure the average size of the cartilage nodules. I used the same 'rolling ball' size for all the images to remove background noise and used the same *particle threshold size* in the 'Particle Analysis' function of ImageJ for all the images. I then divided the average nodular size for each run with FGF treatment by the average for runs with SFDM treatment only.

5.2.3 CFSE Staining and Flow-Cytometry Analysis of Cell Division

If I stain cells with a pulse label of CFSE, all cells take up a comparable amount of CFSE. When cells later divide, the CFSE partitions equally between the daughter cells, reducing staining intensity by a factor of two. I can then measure the cell-division rate by checking the fluorescence intensity using flow-cytometry (Lyon and Parish, 1994; Cooperman *et al.,* 2004). For limb-micromass culture specifically, before plating, I suspended cells in DM (60% DMEM, 40% F-12), incubated them at a concentration of 1×10^6 cells/ml in DM with 5μM CFSE for 10 minutes at 37°C with CO_2, then added 1/5 FBS, and washed with DMS twice. I then plated cells into culture wells at 1.75×10^5/10 μl per spot. For each experiment, I plated CFSE-untreated cells as autofluorescence controls, and Colchicine-treated (1 ng/ml,

colchicine inhibits cell division) and CFSE-treated cells as no-cell-division controls. I used CFSE-treated cells cultured with SFDM only as untreated controls. I incubated CFSE-treated cells with SFDM and FGFs for the first two days, and with SFDM only thereafter. After 4 days, I detached cells with 0.5% trypsin-0.2% EDTA (Gibco) for 20 minutes at 37°C, added FBS, about 1/10 by volume of trypsin solution, and fixed them with 4% paraformaldehyde. Afterwards, I washed the cells, filtered them through a 50 μm nylon filter (Small Parts, Inc.), and stored them in PBS with 2% FBS in the dark at 4°C for about 12-16 hours for analysis the next morning. Analysis used a FACS@Calibur flow-cytometer and cell-Quest Pro software (BD Biosciences, CA). The *absolute division rate*, R_{D}, is:

$$R_{\mathrm{D}} \equiv \frac{\text{MIF of no Division Control} - \text{MIF of Autofluorescence}}{\text{MIF of Sample} - \text{MIF of Autofluorescence}}, \tag{5.3}$$

where, *MIF* is the *Mean Intensity of Fluorescence* of the samples as given by cell-Quest Pro, *MIF of no Division Control* is the MIF for colchicine-treated and CFSE-treated cells. *MIF of Autofluorescence* is the MIF from CFSE-untreated cells and *MIF of Sample* is the MIF for the CFSE-treated cells with SFDM only or also with FGFs.

5.3 Results

Fig. 5.3 shows representative images of Alcian-blue stained cultures for SFDM only (Figs. 5.3A1-4), various FGF4 concentrations (Fig. 5.3B1-4), various FGF8 concentrations (Figs. 5.3C1-4), and various FGF4 and FGF8 treatments (Figs. 5.3D1-4).

5.3.1 Total Micromass Area and Integrated Density of Alcian-Blue Staining

Fig. 5.4A shows that the total area occupied by cells differs for different FGF treatments. Each data point averages three runs of two replicates each. The two-dimensional micromass area decreases significantly with increasing FGF dosage (paired-sample t-test, $P \sim 0.05$, for details, see caption of Fig. 5.4).

Fig. 5.4B shows the Normalized Cartilage-Fraction Ratio (*NCFR*). Since the NCFR represents the degree of chondrogenesis, Fig. 5.4B shows that both FGF4 and FGF4 and FGF8 in combination inhibit chondrogensis (most P values < 0.1), while FGF8 alone may enhance chondrogenesis slightly (most P values > 0.2).

5.3.2 Average Intervals and Nodule Sizes

Fig. 5.4C shows the mean average intervals from three runs, each with two replicates. FGF8 may slightly increase average intervals, while FGF4 decreases them (most P values > 0.2). Consistent with the change in average intervals in Fig. 5.4C, FGF8 may reduce nodule size (paired-sample t-test, $P > 0.1$), while FGF4 increases it ($P < 0.01$) at low and high concentrations and FGF4 and FGF8 double treatment increases it at high concentration ($P = 0.01$).

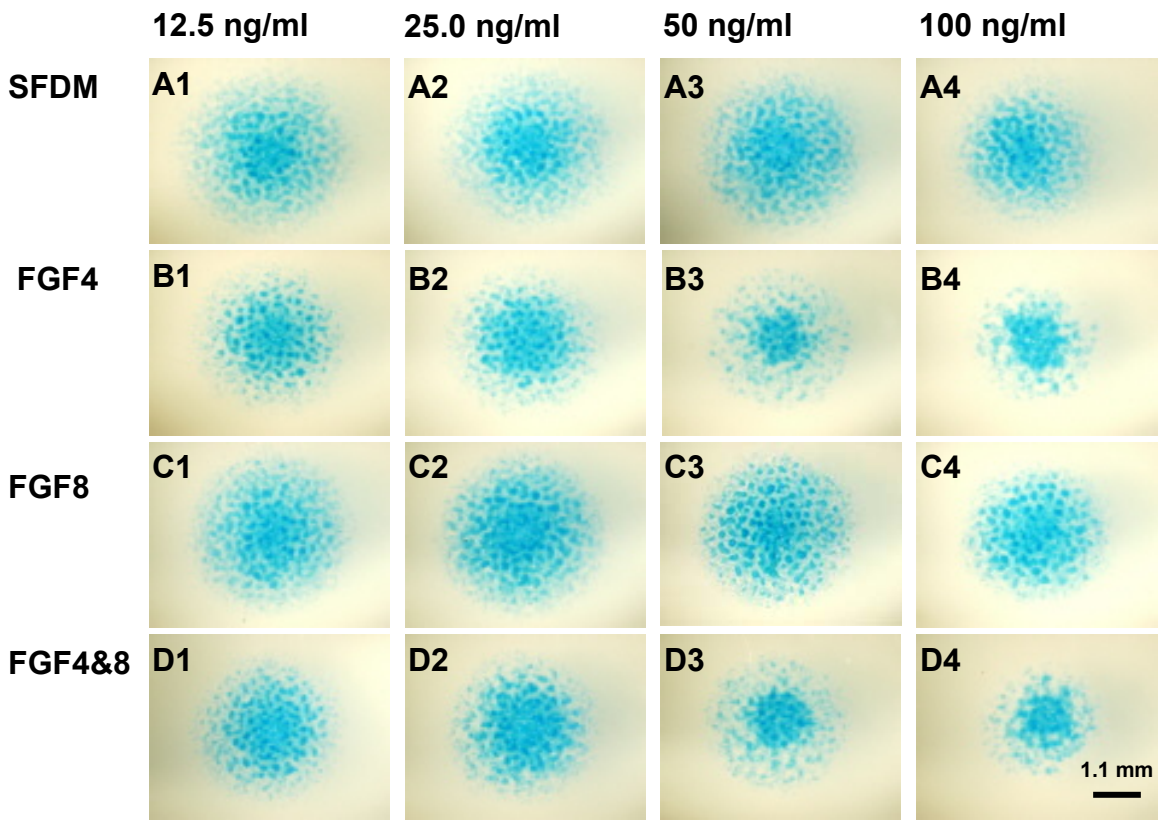

Figure 5.3: Alcian-blue stained chick-forelimb-cell micromass cultures after six days of incubation. FGF treatment types are indicated to the left of each row, FGF concentrations at the top of each column. **A1-A4.** Micromass culture with SFDM only. **B1-B4.** Micromass cultures treated with FGF4 at 12.5 ng/ml, 25 ng/ml, 50 ng/ml and 100 ng/ml; **C1-C4.** Micromass cultures treated with FGF8 at 12.5 ng/ml, 25 ng/ml, 50 ng/ml and 100 ng/ml; **D1-D4.** Micromass cultures treated with FGF4 and FGF8 each at 12.5 ng/ml, 25 ng/ml, 50 ng/ml and 100 ng/ml. FGF4 (B4) but not FGF8 (C4) inhibits cartilage formation at high concentrations. FGF4 and FGF8 double treatment (D4) also inhibits chondrogenesis.

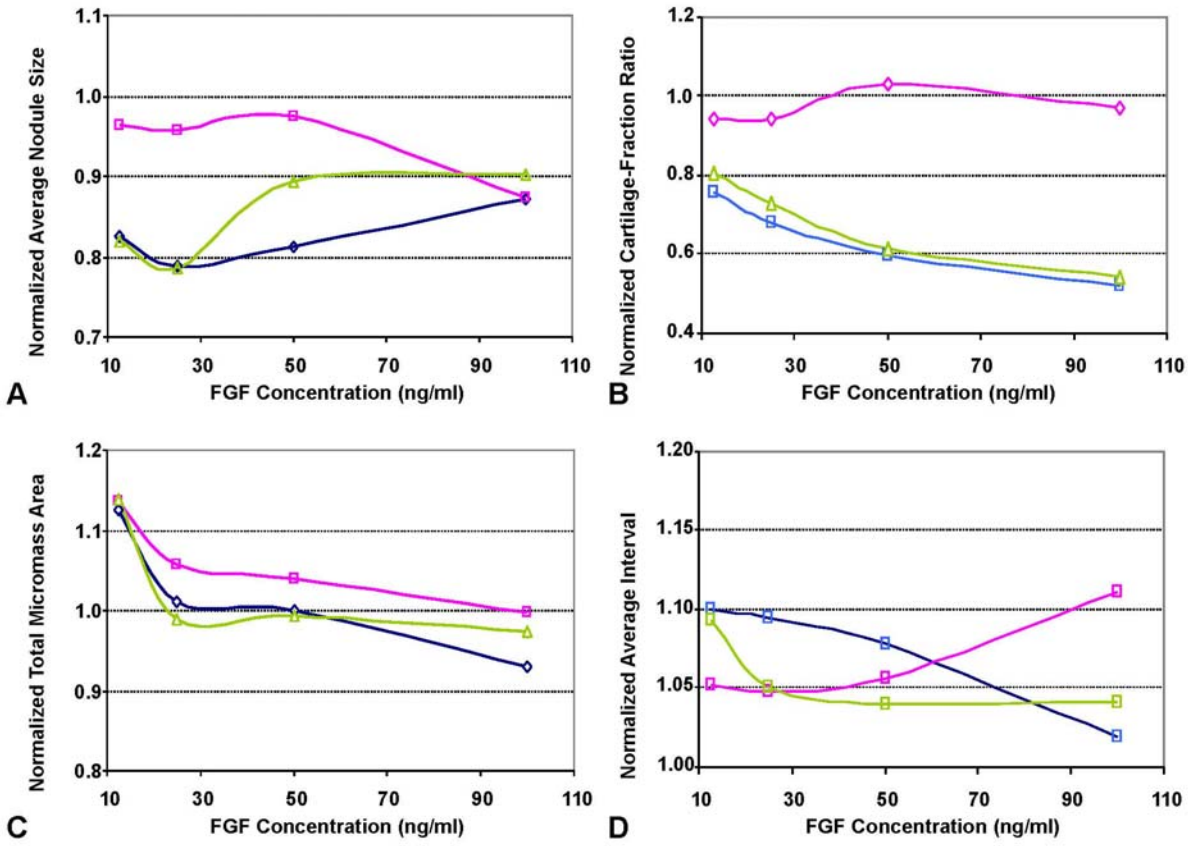

Figure 5.4: Micromass chondrogenic features after various FGF treatments. All values are means for three runs normalized by values for control samples treated with SFDM only. **Blue**, FGF4 treatment. **Red**, FGF8 treatment. **Green**, FGF4 and FGF8 double treatment. Using the paired-sample student t-test, I checked the statistical significance of changes, caused by different FGF dosage ranges (low–12.5 ng/ml to 25 ng/ml, middle–25 ng/ml to 50 ng/ml, and high–50 ng/ml to 100 ng/ml). **A.** Normalized Average Total Micromass Area. The P value under FGF8 treatment is only significant for low concentrations ($P = 0.06$). The P values for the area changes under middle range FGF4 treatment and FGF4 and FGF8 double treatment are not significant. For the other cases, P values ranged from 0.03 to 0.10. **B.** The NCFR as defined in Eq. (5.2). FGF8 causes no obvious changes ($P > 0.25$) for low or high

doses, the change in the middle range is significant (P = 0.09). FGF4 treatment at low and high doses decreases the ratio ($P \leq 0.1$) but the change is not significant in the middle range (P = 0.25). FGF4 and FGF8 double treatment may decrease the ratio at high concentrations (P = 0.01). **C.** Normalized average intervals between cartilage nodules or peaks/valleys show no change with treatment (P values range from 0.1 to 0.49, most > 0.2). **D.** The normalized average size of cartilage nodules. The size changes caused by FGF4 at low and high ranges are significant ($P \leq 0.01$). The changes caused by FGF8 are not significant ($P \geq 0.1$). The change at high concentrations for FGF4 and FGF8 double treatment is significant (P = 0.01).

5.3.3 Average Rates of Cell Division

Fig. 5.5A shows a typical flow-cytometry histogram (x–relative CFSE stain intensity, y–event counts) for CFSE-stain analysis. The horizontal CFSE fluorescence-intensity axis has a MIF cell autofluorescence of about 20. The MIF of FGF4-treated cells is about 700-900, the MIF of FGF8-treated cells is about 1000-1300. The MIF for cells treated with SFDM only is about 2400. Table 5.1 shows mean cell-division rates. Both FGF4 and FGF8 enhance cell division, with the division rate increasing with increasing FGF concentration. FGF4 has a stronger effect than FGF8 at the same concentration. FGF4 and FGF8 double treatment may produce higher cell-division rates than either FGF treatment alone, but the values were not statistically significant. Using the paired-sample student t-test, I checked the statistical significance of differences in cell-division rates over three different dosage ranges (*low*–12.5 to 25 ng/ml, *middle*–25 to 50 ng/ml, and *high*–50 to 100 ng/ml). Different FGF4 doses caused

significant changes (P values from 0.01 to 0.07). For FGF8 treatment, cell division changed significantly only for high doses (P = 0.04).

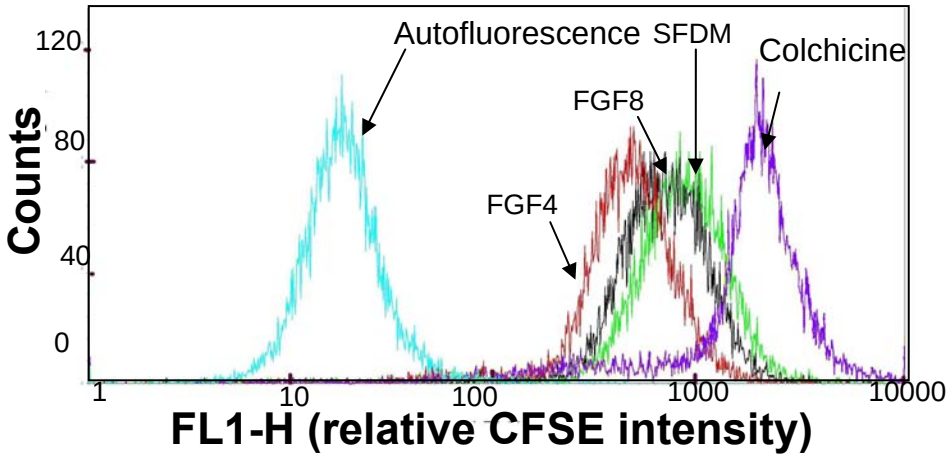

Figure 5.5: Mean cell-division rates assayed by CFSE staining. Typical flow-cytometry histograms (x–relative CFSE stain intensity, y–event counts). From left to right, the curves show an autofluorescence control (since some cells have strong autofluorescence, I use cells without CFSE treatment as autofluorescence controls), FGF4-treated cells, FGF8-treated cells, SFDM-control cells and no-division-control cells (10,000 cells and four runs for each treatment. In each run, all the samples were selected from a sample pool prepared at the same time, by the same person, using the same treatments).

5.4 Discussion

5.4.1 Effects of FGFs on Cell Division

The average cell-division rates in FGF-treated micromass cultures ranged from one half to one per day. Increasing FGF concentration increased the division rate, but only slightly for treatment with a single FGF. The cell-division rate in chick limb buds *in vivo* is much higher than that *in vitro*, three divisions per day (Vargesson *et al.,* 1997). A possible explanation for this difference is that micromass cultures are missing other important proliferation signals present *in vivo* (Sun *et al.,* 2002, Cooperman *et al.,* 2004). FGF8 enhances cell division slightly, which is consistent with Moftah's results for FGF8 in DMS (Moftah *et al.,* 2002). FGF4 enhances cell division more than FGF8 does at the same concentration, which is consistent with Martin's experiments, where replacing *fgf8* with *fgf4* induced *polysyndactyly* (webbing and the presence of extra fingers or toes) (Lu *et al.,* 2006).

5.4.2 Effects of FGFs on Chondrogenesis

At different developmental stages, micromass cells express different types and amounts of FGFs and FGFRs. Thus, the uncertainty caused by the sample collection and experimental manipulations required to set up micromass cultures can cause variations between

experimental runs. This variation can affect chondrogenic patterning, which may explain the variation in the average intervals I measured for treatments which were nominally the same.

Table 5.1: Means and standard deviations of cell-division rates for limb-cell micromass cultures for various FGF treatments. The average cell-division rate for micromass cultures with SFDM treatment was 0.55 divisions per day. Thus, cell division in untreated *in vitro* cultures was very limited.

FGF Concentration (ng/ml)	Means and Standard Deviations of Cell-Division Rates (per day)	
	FGF4	FGF8
12.5	0.89 ± 0.17	0.68 ± 0.16
25	0.95 ± 0.18	0.70 ± 0.15
50	1.00 ± 0.18	0.70 ± 0.14
100	1.10 ± 0.25	0.77 ± 0.13

My sample size is quite small. Increasing the sample size might allow verification of the apparent effect of FGFs on pattern intervals. Alternatively, FGFs might not change the pattern intervals directly, though they may increase the density threshold for chondrogenic patterning by inhibiting chondrogenesis. FGFs are usually considered to be permissive rather than instructive signaling molecules and can affect both growth and patterning (Tickle *et al.*, 1997); *e.g.*, FGF2 and FGF8 interact with FGFR2 to cause perinodular inhibition (Newman *et al.,* 2002). Inevitably, during embryonic development, patterns arise in conjunction with growth. How growth and patterning interact remains unclear, since most mathematical analyses of patterning have neglected growth (Turing, 1952; Crampin *et al.,*1999; Meinhardt,

2003), even though rapid growth can induce patterning instabilities (Barrass *et al.,* 2006). Signaling cascades also interact, *e.g.,* the Wnt- and FGF-signaling pathways both employ GSK3β to regulate β-Catenin and Snail signaling (Katoh and Katoh 2006). Some signaling pathways are also multi-functional; *e.g*., FGFs can regulate cell proliferation, differentiation, survival and motility simultaneously. My experiments were a partially-successful attempt to establish a clear quantitative description of these functions for FGF4 and FGF8.

5.4.3 Effects of FGF-Receptor Binding Specificity

Ligand-binding specificity and the differential-signaling capacity of individual FGF receptors regulate the activity of FGF-signaling pathways (Ornitz *et al.,* 1996). FGF2, FGF4 and FGF8 exert both negative and positive effects on chondrogenesis *via* MEK-ERK activation (Bobick *et al.,* 2007). *In vitro*, individual FGFR proteins bind different FGFs with differing affinities (Ornitz *et al.,* 1996; Itoh and Ornitz 2004; Zhang *et al.,* 2006).

The three distinct FGF receptors that transduce FGF signaling in the developing limb appear in distinct spatiotemporal patterns. Activation of each of these receptors may have distinct effects on cell function. Moftah *et al*. remark: "FGFR1 (Deng *et al.,* 1997; Li *et al.,* 2005) is widely dispersed throughout the precartilage mesenchyme prior to chondrogenic condensation, and may mediate the mitogenic effect of growth factors during bud outgrowth. FGFR2 (Xu *et al.,* 1998) first appears in the mesoblast of the developing limb in the condensing precartilage mesenchyme and may mediate perinodular inhibition of

chondrogenesis (Noji *et al.,* 1993; Szebenyi *et al.,* 1995)" (Moftah *et al.,* 2002). Different FGFs may bind to different FGFRs and contribute to the same goal—limb outgrowth (Yonei-Temura *et al.,* 1999). FGFR1 and FGFR2 may both be present in my experiments, since the cultures demonstrate both cartilage inhibition and proliferation.

Table 5.2: Relative mitogenic activity of the binding of FGFs to specific FGF receptors. Measured by the incorporation of [^{3}H]thymidine. The listed mitogenic activities generally agree with reported receptor-binding properties of FGFs (Ornitz *et al.,* 1996). FGF1 is the only FGF that can activate all FGF receptors. Ornitz *et al*. (Ornitz *et al*., 1996) used FGF1 as an internal standard to determine the relative activity of the binding of other FGFs to different FGFRs. Setting the mitosis rate induced by binding of FGF1 to a given receptor to 100, the activity of binding of other FGFs to the various receptors is defined to be:

$$\frac{\text{Mitosis Rate for } \mathrm{FGF_x} \text{ binding to } \mathrm{FGFR_y}}{\text{Mitosis Rate for } \mathrm{FGF_1} \text{ binding to } \mathrm{FGFR_y}} \times 100.$$

Receptor	FGF4[5]	FGF8[6]
FGFR1b	15.6	5.3
FGFR2b	14.9	5.9
FGFR1c	102.3	57.5
FGFR2c	94.3	91.6

[5] From Ornitz *et al*., 1996.
[6] From Zhang *et al*., 2006.

Table 5.2 lists the binding affinities/specificities of FGF4 and FGF8 with FGFR1 and FGFR2. For cells expressing FGFR1c, FGF4 has twice the mitogenic activity (102.3) of FGF8 (57.5), which may explain why FGF4 is a stronger promoter of cell division and inhibitor of cartilage formation than FGF8 in my experiments. Since FGF4 and FGF8 bind to FGFR2c with the same affinity and since FGF8 maintains FGF10 expression when it binds to FGFR2c (Xu *et al.,* 1998; Lizarraga, 1999), FGF4 may maintain an epithelial-to-mesenchymal regulatory feedback loop when it binds to FGFR2c.

5.4.4 Model of the Role of FGFs in Limb Outgrowth and Patterning

My experiments suggest that the role of FGF4 and FGF8 in promotion of cell division is dose dependent, and that each FGF may have specific effects on cartilage-nodule intervals and sizes. While gradients of FGFs and variations in their downstream MARP/ERK signaling activity have been detected in limb (Nikbakht and Mclachlan, 1997; Pascoal *et al.,* 2007), null results in experiments which induced mutations in FGF receptors suggest that the outgrowth and patterning of the more proximal portions of the limb are insensitive to FGF-receptor signaling (Naski and Ornitz 1998; Talamillo *et al.,* 2005). In contrast, the distal-most limb appears dependent on the degree of FGF-receptor signaling (Talamillo *et al.,* 2005). Combining my results with current understanding, I propose a limb outgrowth-and-patterning model based on the following assumptions:

(1) FGF8 concentration decreases from distal to proximal, and FGF4 concentration decreases from the distal-posterior AER towards the proximal-anterior region of the

limb. These assumptions are based on indirect detection of FGFs' effects (Nikbakht and Mclachlan, 1997; Pascoal *et al.,* 2007).

(2) Higher FGF levels increase cell-division rates. Thus, distal and posterior limb regions have faster cell division.

(3) FGFs modulate the distal pattern of chondrogenesis. As the limb grows and the AER moves away from the more proximal regions of the limb, the pattern of chondrogenesis originally laid down when the region was close to the AER remains unchanged, except for expansion due to cell division.

(4) FGFs induce cartilage nodules with type-dependent and dose-dependent intervals and sizes.

(5) High FGF4 concentrations inhibit cartilage formation.

The domain expansion map in Fig. 5.6A suggests that the distal-posterior domain should expand more than the proximal-anterior domain and contribute more cells to the limb at later stages, consistent with the experimental results of Vargesson (Fig. 5.7, Vargesson *et al.,* 1997) using DiI labeling. Thus, the combined effects of FGF4 and FGF8 may explain differences in digit size and spacing (Fig. 5.6B).

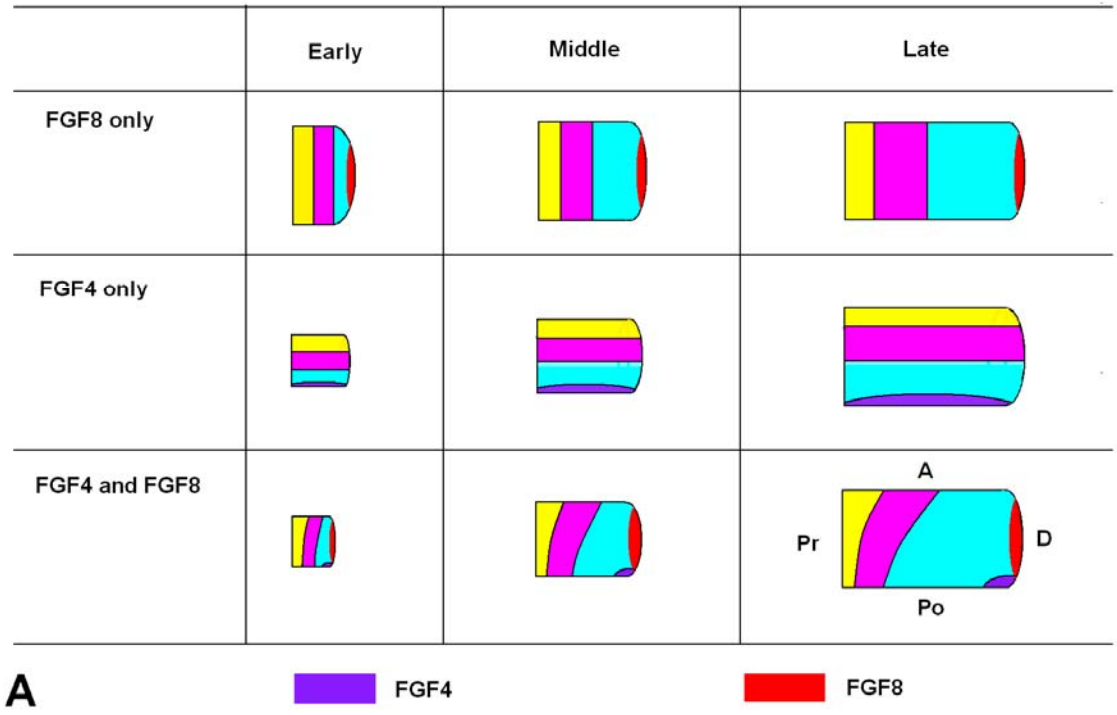
Early
Middle
Late
FGF8 only
FGF4 only
FGF4 and FGF8
A
Pr
D
Po
A
FGF4
FGF8

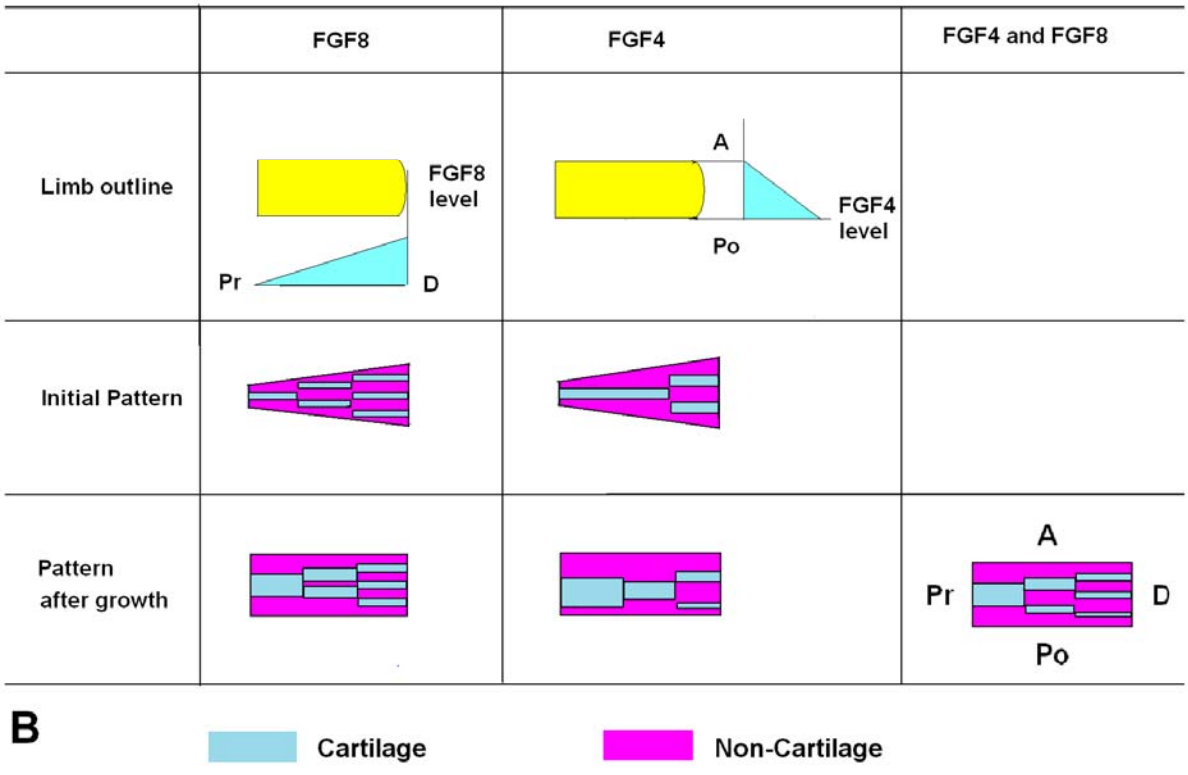
FGF8
FGF4
FGF4 and FGF8
Limb outline
FGF8 level
Pr
D
A
Po
FGF4 level
Initial Pattern
Pattern after growth
A
Pr
D
Po
B
Cartilage
Non-Cartilage

Figure 5.6: Schematic diagram of limb outgrowth-and-patterning model. A. Dependence of cell-domain expansion on FGFs. Stages: **Left**, early. **Center**, middle. **Right**, late. **First row**: with FGF8 only, the distal domain (*D*) expands more than the proximal domain (*Pr*). **Second row**: with FGF4 only, the FGF gradient promotes cell division more in the posterior domain (*Po*) than in the anterior domain (*A*). **Third row**: when FGF4 and FGF8 work together, the distal-posterior domain will contribute most cells in the limb. **B. Patterning model. Left column**: FGF8 controls cartilage intervals. Large concentrations increase intervals and reduce nodule sizes. **Center column**: FGF4 also increases intervals and decreases nodule sizes. Combining the growth in (A) with the nodule pattern induced by the FGFs increases the size of nodules in the proximal domain. **Right column**: FGF4 and FGF8 together produce larger spacings with smaller nodules in the posterior-distal domain.

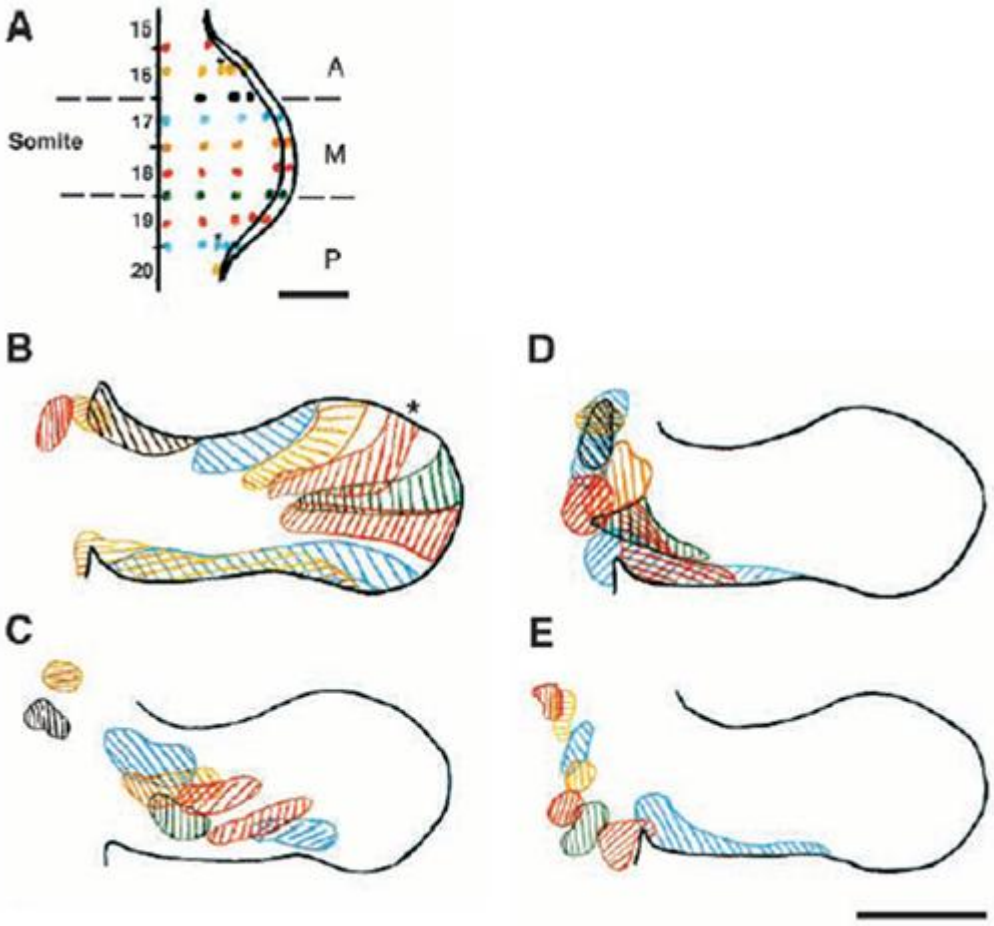

Figure 5.7: Schematic diagram of cell fates in chick limb bud. A. DiI labeling in HH stage 20 wing bud. **B.** Sub-apical mesenchyme populations at HH stage 28. **C.** Mesenchyme, labelled 500 μm from the somites at HH stage 20, at HH stage 28. **D.** Mesenchyme labelled 250 μm from the somites at HH stage 20, at HH stage 28. **E.** Mesenchyme labelled 50-75 μm from the somites at HH stage 20, at HH stage 28. Scale bar represents 300 μm (diagram from Vargesson *et al.*, 1997).

CHAPTER SIX

CONCLUSION AND FUTURE WORK

6.1 Conclusion

Genes and their direct interactions can now be characterized. However, we still cannot predict phenotype from genotype because morphogenesis combines molecular, cellular, tissue and organ scales and because each scale contains complex dynamic interactions. Progress requires effective approaches to identifying the main themes and neglecting unnecessary information.

I have presented a framework (Chapter One) and a few examples (Chapters Two through Five) of multiscale approaches to morphogenesis. My work on cell sorting links molecular binding between cadherins to cell-cell interactions and cell-sorting structures, which are simple morphological forms. In the more complex morphogenesis of somitogenesis, cell-cell adhesion and repulsion and cell-ECM interactions plausibly translate genetic information into physical interactions and then into phenotype. In the case of limb growth, the Progress Zone Model has dominated interpretation of proximo-distal limb patterning, though recent experiments partially support the Early-Specification Model. Molecular evidence supports

neither model. My assays of the roles of FGFs in chondrogenic patterning and cell division in micromass cell culture suggest an alternative model for limb outgrowth and patterning.

To show how the methodologies I have developed can apply to other developmental problems, I propose a new approach to understanding the origin of left-right asymmetry in embryos.

6.2 Future Work: Dynamic Orchestration of Cell Movement and Electrophoresis and the Role of Serotonin in Creating Left-Right Asymmetry in the Early Chick Gastrula

6.2.1 Introduction

Vertebrates combine a roughly bilaterally-symmetric body plan with left-right (*LR*) asymmetric organs. Experimental observations of the asymmetries in gene expression (Mercola and Levin, 2001; Levin, 2005) leave open many questions about the mechanisms leading to the initial distinction between left and right. Gap junctions (Levin and Mercola, 1999), H^+/K^+-ATPase (Levin *et al.,* 2002), H^+-V-ATPase (Adams *et al.,* 2006) and serotonin signaling cascades (Fukumoto *et al.,* 2005a, 2005b; Levin *et al.,* 2006) are all upstream of LR-asymmetric genes. A bioelectric circuit composed of gap junctions (Levin and Mercola, 1999) and ion pumps (Levin *et al.,* 2002; Adams *et al.,* 2006) might provide both an

electrophoretic driving force and channels for distribution of morphogen-like small molecules, such as serotonin. This mechanism could translate subcellular asymmetries into large-scale, multi-cellular asymmetry. A mathematical electrophoretic model (Esser *et al.,* 2006) works well for *Xenopus*, but may not produce the correct LR serotonin gradient over the right time scale for chick, which has a different gastrulation architecture and more cells at the time of gastrulation. Serotonin, its receptors 5-HT-R3 and 5-HT-R4, its degradation enzyme MAO (Fukumoto *et al.,* 2005a), and transporters SERT and VMAT (Fukumoto *et al.,* 2005b) are all involved in LR asymmetry in both *Xenopus* and chick. Fully understanding serotonin distribution and related signaling will clarify the origin of LR asymmetry and serotonin's function in controlling early embryogenesis (Levin *et al.,* 2006), and suggest potential pharmaceutical interventions to prevent LR-related birth defects.

6.2.2 Hypotheses

How is serotonin distributed and how does it function in early gastrulation-stage chick? I propose that cell movement and electrophoretic forces may orchestrate the serotonin distribution. During early gastrulation in chick, the epithelial cells move long distance to form vortices on both sides of the primitive streak (Fig. 6.1, Cui *et al.,* 2005; Chuai *et al.,* 2006). Serotonin first appears in the *area opaca*, the opaque peripheral area of the blastoderm, and later in the primitive streak (Levin, 2005). If cells carried serotonin, they would redistribute serotonin on a time-scale of 10 hours. Furthermore, ectoderm/epithelial ingression may form a nonconducting region (*isolation zone*) in the mesoderm, cause

mesenchymal lateral movement and lead to a membrane-depolarization positive feedback loop triggered by 5-HT-R3 on the left side of the primitive streak, which orients the LR axis with respect to the dorso-ventral (*DV*) and anterior-posterior (*AP*) axes.

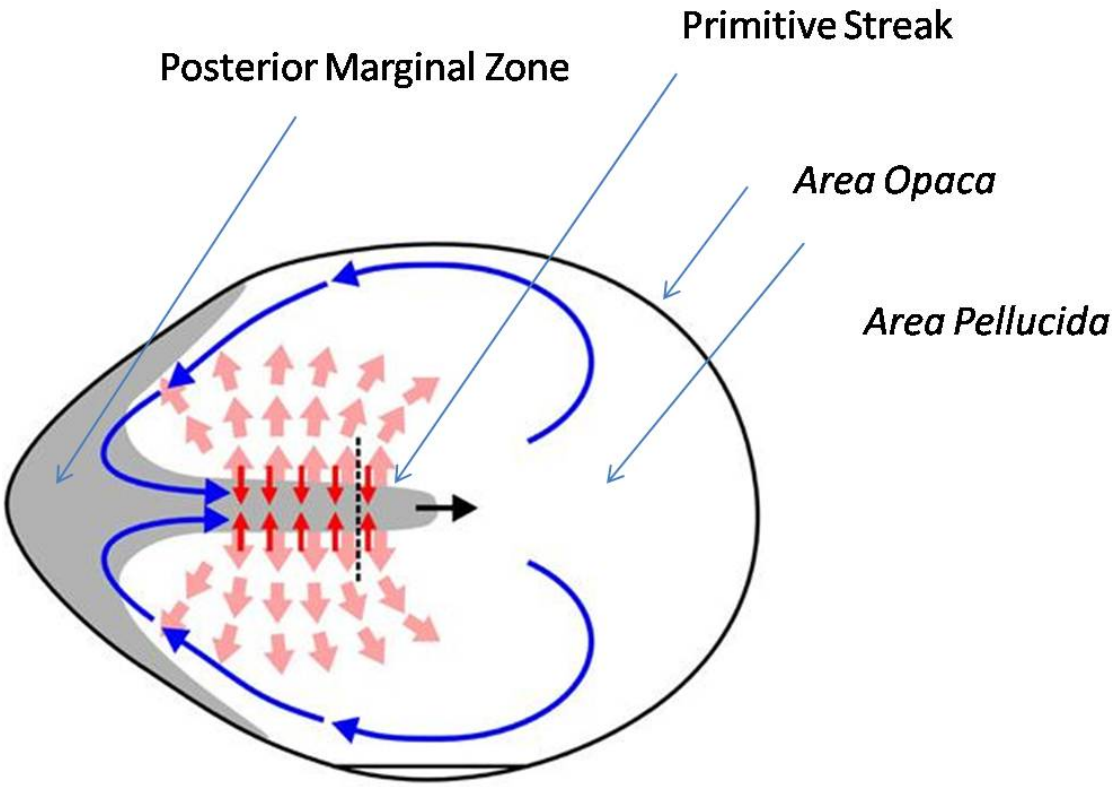

Figure 6.1: Schematic diagram of cell migration in a chick gastrula. As lateral epiblast cells move towards the posterior marginal zone, posterior epiblast cells move towards the primitive streak, forming a pair of counter-rotating vortices in the posterior two-thirds of the embryo (Diagram from Dormann and Weijer, 2006).

In unincubated chick, serotonin clusters in discrete spots around the periphery of the *area opaca*. At stage HH 1-4, primitive-streak cells express serotonin. Serotonin's receptor, 5-HT-R3, a ligand-gated Na^+ and K^+ cation channel, may trigger plasma-membrane depolarization on the left side of the streak in an acid environment.

6.2.2.1 Cell movement during early gastrulation in chick may transport serotonin to the right position at the right time

Cells move extensively in the early chick gastrula as in fig. 6.1 (Chuai *et al.,* 2006). According to Gilbert: "At stage 2, the *primitive streak* forms a dense cell layer between the epiblast and endoblast. At stage 3, it becomes a mesenchymal rod. Soon afterward (HH 3^+), the ingression of epiblast cells into the streak (*groove formation*) causes the mesenchyme of the streak to start lateral migration. At stage 4, *Hensen's node* appears at the tip of the streak." (Gilbert, 2006). The timing and direction of cell movement may bring serotonin from the periphery of the blastomere into the streak domain.

6.2.2.2 The asymmetry of small molecules and gene expression and activity match specific morphogenesis events in early-gastrulation chick embryos

An ion pump H^+/K^+-ATPase appearing between HH stages 2^+ and 4^-, produces and maintains an asymmetric membrane potential (HH stages 3-4^+), which affects asymmetric gene expression. H^+-V-ATPase, expressed in the primitive streak of chicks between HH stages 2-4, supplies protons to the serotonin transporter VMAT (Fukumoto *et al.,* 2005b), regulates

pH in early chick blastoderm, and is required for normal localization of serotonin (Adams *et al.,* 2006). Connexin43 is expressed throughout the chick blastoderm, except in the node and streak at HH stages 2-3. Thus gap junction channels form everywhere except in the streak (Levin and Mercola, 1999). From HH 3^+ (about the time the asymmetric membrane potential appears and about the time the groove forms), the earliest asymmetric genes are right-sided activin-RIIa (Levin *et al.,*1997) and left-sided HNF3-β. At HH 4, Hensen's node appears. By stage HH 4-4^+, shh appears on the left, fgf8 on the left, and nodal just to the left of the node (Levin *et al.,* 1995). This pattern suggests that ingression may separate the left and right sides of the streak mesoderm, isolating the two sides.

6.2.3 Suggested Approaches

To validate my hypotheses, I will first track cell subpopulations, single cells and serotonin *in vivo* throughout the embryo between HH stage 1 and HH stage 4. I will disrupt cell movement and/or the bioelectric circuit (Levin and Mercola, 1999; Levin *et al*., 2002; Adams *et al.,* 2006) to check the diffusion rate of serotonin in the absence of cell movement and electrophoresis. I will check whether this disruption affects only LR asymmetry or both LR asymmetry and patterning along the other axes and integrate these results with morphogenesis modeling to check their biological interpretation. I describe the procedures for these studies below:

6.2.3.1 Cell-movement tracking

I will conduct fluorescent labeling (GFP, DiI, Bodipy-ceramide), time-lapse imaging and tracking of cell subpopulations and single cells (Yang *et al.,* 2002; Cui *et al.,* 2005; Chuai *et al.,* 2006).

6.2.3.2 Serotonin tracking *in vivo*

I will develop a method to fluorescently tag serotonin. The problem is to keep serotonin's low molecular weight (176 Da), which allows it to pass through gap junctions between cells, and maintain its physiological functions. I will use Fluorescence Recovery after Photobleaching (*FRAP*) to measure the diffusion rate of serotonin (Reits and Neefjes, 2001). Alternative methods are also available, *e.g*., labeling cell populations at specific positions in the embryo, and fixing the embryo at certain time points to produce temporal and spatial mappings of serotonin expression for certain cell populations.

6.2.3.3 Cell and serotonin tracking

First, I will track cells and serotonin *in ovo* at the same time. Then I will apply pharmacological treatments and genetic manipulation to disrupt or express ion pumps and gap junctions (Levin and Mercola, 1999; Levin *et al.,* 2002; Adams *et al.,* 2006), and repeat my tracking experiments. Then, I will block cell movement (Yang *et al.,* 2002; Cui *et al.,* 2005; Chuai *et al.,* 2006) and repeat my tracking experiments. In addition, I will use *in situ* hybridization and immunohistochemistry to confirm the expression of downstream

asymmetric genes and proteins (Levin *et al.,* 1995; Levin and Mercola, 1999; Levin, 2005; Adams *et al.,* 2006).

To check the time correlation between cell movement, serotonin concentration and membrane depolarization, I will also image the membrane voltage using Bis-(1,3-dibarbituric-acid)-trimethine-oxanol (*DiBAC$_4$(3)*).

6.2.3.4 Modeling of the serotonin distribution and cell movement during early chick gastrulation

I will use the Glazier-Graner-Hogeweg model (*GGH*) (Graner and Glazier, 1992; Glazier and Graner, 1993) coupled with an electrophoresis model (Esser *et al.,* 2006) to study the coordination of electrical potential with cell movement and reproduce the experimental results of chemical and genetic manipulations. The integrated model will provide a comprehensive quantitative tool to validate the biological interpretation of my experiments.

6.2.4 Expected Results

(1) If cell flow alone causes the serotonin distribution, serotonin speed will be equivalent to cell speed. If I interrupt the ion pump or ion-pump-dependent voltage, the serotonin distribution will not change.

(2) If the serotonin distribution is driven only by electrophoretic forces, interrupting cell movement will have no influence on the serotonin distribution.

(3) Cell movement and electrophoretic forces may both contribute to the serotonin distribution, in which case both disruptions will disturb the serotonin distribution.

(4) The two mechanisms may function at different locations or times, with cell flow creating the initial serotonin distribution, and electrophoretic forces stabilizing and maintaining the serotonin localization.

(5) To check whether serotonin induces depolarization of cell membranes, I will compare the local time progression of serotonin concentration and membrane polarization.

(6) Since synthesis, degradation and diffusion of serotonin occur at the same time, time-lapse tracking of cells and serotonin is important to understanding the role of these three mechanisms.

7. APPENDICES

7.A Protocols for Cell-Sorting Experiments

7.A.1 Introduction

Cell lines expressing recombinant cadherins are common models in the study of cell sorting (Steinberg and Tekeichi, 1994; Nose *et al*., 1988; Duguay *et al*., 2003; Foty and Steinberg, 2005). Developing these lines involves cell-line construction and selection, Ca^{2+}-independence and Ca^{2+}-dependence assays, and cell-aggregate building for cell-sorting analysis.

7.A.2 Materials

[Superscripts refer to catalog numbers on page 153, section 7.A.5]

1. Chinese Hamster Ovary (*CHO*) cells[1] expressing E-cadherin-GFP.
2. 10% (2%) DMS: Dulbecco's modified Eagle medium (*DMEM*)[2, 3] with 10% (2%) Fetal Bovine Serum[4] and 10 units/ml Penicillin, and 10 μg/ml Streptomycin[5].
3. G418[6].
4. 35 mm[7] or 60 mm[8] Petri dishes.

5. HBSS CMF with $NaHCO_3$[9].
6. HCMF.
7. 0.25 M $CaCl_2$ Medium.
8. Trypsin[10].
9. DNase I[11].
10. 1.25% agar-coated Petri dishes.
11. EGTA[12].
12. HCMF with 10% Bovine Serum Albumin[13].
13. Microscalpel.
14. CO_2-independent media[14].
15. Round-bottom tubes[15].
16. Qiagen transfection Reagent[16].
17. Cloning Ring[17].
18. DNA Plasmid (for E-cadhein-GFP fusion protein; Yamada *et al*., 2005).

7.A.3 Procedures

7.A.3.1 Cell Line Construction and Selection (Nose et al., 1988; Duguay et al., 2003)

1. Grow wild-type Chinese Hamster Ovary (*CHO*) cells in 10% DMS in a humidified 5% CO_2 atmosphere at 37°C.
2. Transfect 60-80% confluent cells with 5 μg plasmid in a 35 mm dish using Qiagen transfection reagent according to the vendor's instructions.

3. Select cells expressing E-cadherin-GFP using 400 μg/ml G418 for two days.
4. Transfer the transfected cells to a 100 mm dish.
5. Select cells expressing E-cadherin-GFP using 400 μg/ml G418 for about two weeks.
6. Isolate single clones by cloning Ring (following vendor's instructions).
7. Analyze the E-cadherin-GFP expression levels of individual clones using flow-cytometry:
    1) Detach cells using 0.2% trypsin for 5 minutes.
    2) Incubate cells in CO_2-indepent media with 2% FBS.
    3) Culture cells in rotary shaker at 80-120 rpm at 37°C for 3-5 hours.
    4) Fix cells for 2-5 minutes using 2% formaldehyde. Pellet cells and wash twice using HCMF.
    5) Store cells in the dark in HCMF with 2% FBS on ice.
    6) Flow-cytometry will depend on the instrument used.
8. Observe cell morphology and E-cadherin-GFP expression using a multiphoton laser-scanning confocal microscope.
9. Select the cell lines positive for E-cadherin-GFP expression on their membranes but with little or no E-cadherin-GFP in their cytoplasm.

7.A.3.2 Ca 2+-Independence Assay and Ca2+-Dependence Assay (Nose et al., 1988)

1. Incubate cells with 0.01% trypsin in HCMF plus either 1 mM $CaCl_2$ (*TC-treatment*) or 1 mM EGTA (*TE-treatment*) at 37°C for 30 minutes.

2. Wash the trypsinized cells by gently pipetting in HCMF at 4°C (about 30 times) to obtain a single-cell suspension.

TC-aggregation

1. Place TC-treated cells 1×10^6 per 2 ml HCMF containing 1 mM $CaCl_2$ and 1% bovine serum albumin and either no, 0.1 mM or 1 mM $CaCl_2$ in each well of a 6-well Petri dish.
2. Incubate cells on a rotary shaker (80 rpm) for 30-60 minutes at 37°C.

TE-aggregation

1. Place TE-treated cells 1×10^6 per 2 ml of CO_2 independent medium with 10% FBS in each well of a 6-well Petri dish.

2. Incubate cells on a rotary shaker (80-100 rpm) for about 10 hours at 37°C.

7.A.3.3 Production of Cell Aggregates for Cell-Sorting Experiments (from Steinberg and Takeichi, 1994)

1. Wash near-confluent cells twice with Hanks balanced salt solution (HBSS CMF (Ca^{2+} and Mg^{2+} free)) containing 2 mM $CaCl_2$.
2. Treat cells with trypsin 0.01% (diluted from 2.5% stock) with 1 mM $CaCl_2$ for 20 minutes.
3. Re-suspend the cells in CO_2-independent media with 2% FBS (GIBCO).
4. Allow cells to recover from trypsinization for 0.5-2 hours on a shaker at 80 rpm at 37°C.

5. Pipette the cell suspensions as necessary to disperse any small aggregates.
6. Pellet the cell suspensions in round-bottomed culture tubes by brief centrifugation at 1200 rpm in a table-top centrifuge.
7. Incubate the thin cell pellets for 3-22 hours to allow them to firm.
8. Cut the thin pellets into small fragments (200 × 200 μm^2) with a microscalpel.
9. Allow the fragments to round up in DMEM with 2% FBS and 50 μg/ml DNase I on 1.25% agarose-coated Petri dishes at 37°C in a 5% CO_2 environment.
10. Select fragments of 150-300 μm in diameter for cell-sorting analysis.

7.A.4 Recipes

HBSS CMF, HBSS and HCMF Buffer

COMPONENT	HBSS CMF (g/L)	HBSS (g/L)	HCMF (g/L)
$CaCl_2 \cdot 2H_2O$	—	0.1855	—
$MgSO_4$ (anhydrous)	—	0.09767	—
KCl	0.40	0.40	0.40
KH_2PO_4 (anhydrous)	0.06	0.06	0.06
$NaHCO_3$	0	0.35	—
NaCl	8.0	8.0	8.0
Na_2HPO_4 (anhydrous)	0.04788	0.04788	0.04788
D-Glucose	1.0	1.0	1.0
Phenol Red•Na	—	0.11	—
HEPES			2.383

Preparation:

Dissolve the relevant reagents for the buffer (in the above table) in distilled water. Adjust pH to 7.4.

Sterilization: Filter sterilize.

Store at 4°C.

0.5/0.1 M EGTA (pH=8.0)

Preparation:

Dissolve EGTA in 800 ml distilled water.

Adjust the pH to 8.0 using NaOH (~20 g of NaOH pellets). EDTA will dissolve at pH 8.0.

Adjust volume to 1 liter with distilled water.

Sterilization: Autoclave.

Store at room temperature.

DNase I

Preparation:

Add 1 mg DNase I per ml HBSS CMF with 5 mM $CaCl_2$.

Prepare fresh each time.

Store at -20°C.

$CaCl_2$ Medium

Preparation: 0.25 M stock medium in distilled water.

Sterilization: Autoclave.

Store at room temperature.

10% BSA

Preparation: Dissolve 10 g in 100 ml medium.

Sterilization: Filter through a 0.45 μm pore-size filter first, then through a 0.22 μm pore-size low-protein-binding filter.

Store at 4°C in the dark.

7.A.5 Catalog Numbers

1. CHO (ECACC 85050302).
2. DMEM (GIBCO 10313).
3. DMEM (GIBCO 11965-118).
4. FBS (GIBCO 16000-044).
5. Penicillin-streptomycin (GIBCO 15140).
6. G418 (GIBCO 11811-023).
7. 35mm Petri dishes (Corning).
8. 60mm Petri dishes (Falcon, Corning).
9. HBSS CMF with $NaHCO_3$ (made according to Sigma recipes H4891 or H6648).
10. Trypsin 2.5% (Invitrogen 15090-046).
11. DNase I (Sigma D5025).
12. EGTA (Sigma E3889).
13. Bovine Serum Albumin (Sigma A3311).
14. CO_2-independent media (GIBCO 18045-088).
15. Round-bottom tubes (BD Biosciences).
16. SuperFect Transfection Reagent (Qiagen 301305).

17. Cloning Ring (Fisher 14-512-78).

7.B Protocols for Chick-Limb Micromass Culture

7.B.1 Introduction

Micromass culture is a way to culture cells as confluent monolayers in order to mimic *in ovo* cellular conditions. As an *in vitro* approach, it allows "rapid prescreening of various bioactive compounds (*e.g.*, hormones, growth factors, vitamins, adhesion factors) for effects on limb mesenchymal cell differentiation" (Paulsen and Solursh, 1988).

For the study of chick-limb-cell chondrogenesis specifically, I developed my protocol from the original work of Paulsen and Solursh (Paulsen and Solursh, 1988) and my training experience in the Newman laboratory (Downie and Newman, 1994, 1995). It includes modification from Cheng Cui's protocol (Cui, 2005), and others, which I developed in the Glazier laboratory.

7.B.2 Materials

1. White Leghorn fertilized chicken eggs.

2. 70% ethanol.
3. Cold EBSS with Ca^{2+} and Mg^{2+}.
4. Fine-tip forceps.
5. 15 ml centrifuge tube.
6. EBSS without Ca^{2+}/Mg^{2+}.
7. EDTA.
8. Fetal Bovine Serum (*FBS*).
9. Trypsin.
10. DMS.
11. SFDM.
12. 18 G Needle and 3 ml syringe.
13. Nylon filter on a filter gasket.
14. Hemacytometer and Microscope.
15. Centrifuge.
16. CO_2 incubator.
17. 37˚C water bath.

7.B.3 Procedures

7.B.3.1 Collect Limb Tips (5 dozen eggs)

1. Incubate eggs at 38°C, with humidity above 60%, until HH stage 24-25 (Hamburger and Hamilton, 1951). Spray 70% ethanol on eggs.
2. Open the eggs and extract the embryos into a dish[1] containing cold EBSS with Ca^{2+} and Mg^{2+}.
3. Remove the outer membrane around the embryos and transfer them to a new dish containing EBSS with Ca^{2+} and Mg^{2+}.
4. Use fine-tip forceps to cut off the limb tips, 0.3 mm (for stage 25), or 0.2 mm for stage 24) (Newman *et al*., 1981) from the distal end and put them into a new dish containing EBSS with Ca^{2+} and Mg^{2+}.
5. Collect tips and put them into a 15 ml centrifuge tube[2].

7.B.3.2 Removal of Ectoderm Using EDTA Treatment

1. Pellet collected tips at 500 rpm for about 2 minutes.
2. Remove EBSS with Ca^{2+} and Mg^{2+}.
3. Add 5 ml of EBSS[3] without Ca^{2+} or Mg^{2+} and 100 µl EDTA[4].
4. Incubate for 20 minutes at 37°C (CO_2 5%). Do not close the centrifuge-tube lid too tight.
5. Add 100 µl of FBS[5] to stop EDTA reaction.

6. Transfer tips to a clean dish with fresh EBSS with Ca^{2+} and Mg^{2+}. Gently pipette to remove ectoderm. Use a microscope to determine the cells from which ectoderm has been removed.
7. Pick out large pieces of mesenchyme and transfer into about 5 ml of fresh EBSS with Ca^{2+} and Mg^{2+}.
8. Spin at 500 rpm to pellet.
9. Remove most of the medium, leaving a small amount in the tube with the pellet.

7.B.3.3 Preparation of Cells for Incubation

1. Pellet tips at 500 rpm for 5 minutes.
2. Add 4.5 ml EBSS without Ca^{2+} or Mg^{2+} and 500 µl Trypsin[6].
3. Incubate about 15-20 minutes at 37°C (CO_2 5%). Loosen the tube lid a little bit.
4. Warm about 5 ml of DMS at 37°C.
5. Obtain a filter unit and place in a nylon filter[7] on a filter gasket[8].
6. Obtain a 3 ml syringe[9] and 18 G needle[10].
7. After trypsinizing tips, close tube tightly. Spin at 500 rpm for 5 minutes to pellet.
8. Remove media from the tube.
9. Add 2.5 ml fresh pre-warmed DMS into the tube.
10. Place needle and syringe in the tube and pull the media up and down 20 times to dissociate cells.
11. Suck cells up into syringe.

12. Remove needle, replace with the filter unit and gently push media with cells through the filter into a clean 15 ml tube.
13. Remove 10 µl of cell suspension for cell counting.
14. Place 15 ml tube in centrifuge and pellet at 500 rpm for 15 minutes.

7.B.3.4 Plating

1. Remove as much DMS from the 15 ml tube as possible. I assume that 20 µl of medium is left. Add the proper amount of DMS to obtain the desired cell density, typically about 1.6-2.0 × 10^4 cells/µl. The volume V in µl of DMS to be added is:

$$V = \frac{x \cdot y}{z} - 20,$$

where x (cells) is the number of cells in one cell-counting chamber (0.1 mm^3), y is the original volume of the cell suspension (about 2-2.5 ml) and z is the target cell concentration (typically, 10^4 cells/µl). To count cell using a Hemacytometer, refer to the Sigma product specification for "Bright-Line™ Hemacytometer Sigma Z35,962-9."
2. Use a micropipette to pull medium with cells up and down 5-10 times. Do not introduce air bubbles.
3. Add 10 µl of cell suspension to each well of a 24-well TC-treated microplate[11] or to 60 mm cell-culture treated dishes[12] and incubate in a 5% CO_2 atmosphere at 37°C.
4. Warm enough DMS to flood the cell-culture wells.
5. After 45 minutes, flood each well with 0.5 ml or 1 ml of fresh pre-warmed (37°C) DMS.

7.B.4 Recipes

EBSS with Ca^{2+} and Mg^{2+} (1 liter).

Components:

One pack of modified Earle's Balanced Salts[13].

2.20 g Sodium Bicarbonate ($NaHCO_3$).

Preparation: Add 900 ml deionized and distilled H_2O, adjust pH to 7.2; fill up to 1 liter.

Sterilization: Filter through 0.22 μm filter.

Store at 2-8°C.

DMEM (1 liter).

Components:

One pack of Dulbecco's Modified Eagle's Medium[14].

3.70 g Sodium Bicarbonate ($NaHCO_3$).

Preparation: Add 900 ml ddH_2O; adjust pH to 7.2; fill up to 1 liter.

Sterilization: Filter through 0.22 μm filter.

Store at 2-8°C in the dark

F-12 (Ham) with L-Glutamine and sodium bicarbonate (1 liter)

Components:

One pack of F-12[15].

1.18 g sodium bicarbonate ($NaHCO_3$).

Preparation: Add 900 ml ddH_2O; adjust pH to 7.2; fill up to 1 liter.

Sterilization: Filter through 0.22 μm filter.

Store at 2-8°C in the dark.

DM

Components:

600 ml F-12.

400 ml DMEM.

Store at 2-8°C in the dark.

Serum-Free Defined Medium (*SFDM*, 1 liter)

Components:

	Final concentration	Add	Function
F-12	60%	600 ml	
DMEM	40%	400 ml	
10 × chick transferrin	5 μg/ml	1000 μl	Enhances myogenesis
10 × L-Ascorbic Acid	50 μg/ml	5000 μl	Enhances chondrogenesis
10 × Insulin	5 μg/ml	500 μl	Minimal additive, also promotes growth
1 × hydrocortisone	100 Nm	100 μl	Minimal additive for cell culture medium
Pen-Strep	10 units/ml penicillin, 10 μg/ml streptomycin	10 ml	Antibiotics

Store at 2-8°C in the dark.

DMS (100 ml)

Components:

90 ml DM.

10 ml FBS[16].

Store at 2-8°C in the dark.

Prepare fresh if possible. Discard after two weeks.

Transferrin: 5 mg/ml in DM

Components:

50.0 mg transferrin[17].

10 ml DM (60 ml F-12 + 40 ml DMEM).

Prepare fresh for each use.

Store at -20°C for up to 6 months.

Ascorbic Acid 10 mg/ml

Components:

100 mg ascorbic acid[18].

10 ml DM.

Prepare fresh for each use.

Store at -20°C.

Insulin 10 mg/ml

Components:

Preparation: 10 mg/ml Insulin[19] in 0.01 N[7] HCl.

Sterilization: Sterilize the HCl solution before adding the Insulin.

Store at 0°C for up to 6 months.

Hydrocortisone[20] 1 mM in distilled H_2O

Store at -20°C for up to 1 year.

Penicillin-Streptomycin (*Pen-Strep*[21])

Store at -20°C.

7.B.5 Catalog Numbers

1. 100 mm Petri dishes (Fisher 08-757-11Z).
2. 15ml tube (Fisher 14-959-49B).
3. EBSS without Ca^{2+} or Mg^{2+} (Gibco 14155-063).
4. EDTA (Fisher BP120-500).
5. FBS (HyClone SH30071.01).
6. Trypsin (Gibco 15400-054).
7. Nylon filter (Nytex 20-μm mono-filament nylon mesh, 13 mm in diameter. TETKO, 333 South Highland Ave, Briarcliff Manor, Tel: 914-941-7767, or 1-800-995-0531).
8. Filter gasket (Millipore SX0001300).

[7] Unit for HCl.

9. 3 ml syringe (Fisher 14-823-40).
10. 18 G needle (Fisher 14-826-5D).
11. 24-well plate (Corning 3526).
12. 60 mm plate (Corning 430166).
13. EBSS with Ca^{2+} and Mg^{2+} (Sigma E6132).
14. DMEM (Gibco 12100-046).
15. F-12 (Gibco 21700-075).
16. FBS (Invitrogen 16000-036).
17. Transferrin (Sigma C0880).
18. Ascorbic acid (Sigma A4403).
19. Insulin (Sigma I1882).
20. Hydrocortisone (Sigma H0135).
21. Penicillin-Streptomycin (Invitrogen 15140-148).

7.C Protocols for Alcian-Blue Staining of Chick-Limb Micromass Cultures

7.C.1 Introduction

Stain sulfated proteoglycans with Alcian blue to show cartilage patterns (Moftah *et al*., 2002).

7.C.2 Materials

1. Fixative.
2. 3% Acetic Acid Solution, pH 1.0.
3. 3% Acetic Acid Solution, pH 2.5.
4. 0.5% Alcian-blue Solution.
5. PBS.

7.C.3 Procedures

1. Rinse cell cultures with PBS 3 times.
2. Fix cultures in fixation medium for 5 minutes.
3. Wash cultures with 3% acetic acid, pH 1.0, for 1 minute.
4. Stain cultures overnight with 0.5% Alcian-blue solution.
5. Remove Alcian-blue solution.
6. Wash with 3% acetic acid, pH = 1.0, to remove unbound stain.
7. Add 3% acetic acid, pH = 2.5.
8. Visualize cartilage patterns under a binocular dissecting microscope.

7.C.4 Recipes

Fixative

Components:

25 ml 4% Paraformaldehyde.

75 ml of 1 × PBS.

0.5 g Cetyl Pyridinium Chloride.

Preparation: Stir overnight.

Store at room temperature.

3% Acetic Acid Solution

Components:

15.0 ml Glacial Acetic Acid.

485.0 ml Distilled Water.

Preparation: Adjust pH to 1.

Store at room temperature.

0.5% Alcian-blue Solution

Components:

0.5 g Alcian-blue 8GS.

100.0 ml 3% Acetic Acid pH 1.

Preparation: Stir overnight and filter.

Store at 4˚C.

7.C.5 Catalog Numbers

1. Alcian-blue 8GS (EMS 10207-100g or 10305-25g).
2. Cetyl pyridinium chloride (Sigma C0732-100G or C9902-25G).

7.D ImageJ Macro Code for Peak-Length Determination of the Average Interval

Chapter Five describes the peak-length method to determine the average interval in chick-limb micromass culture. I developed this implementation specifically for Alcian-blue-stained cultures. I used "Subtract Background" in ImageJ to remove unevenly distributed background noise and then used "Skeletonize" in ImageJ to obtain the number of peak and valley pixels in the chondrogenic patterns.

The average interval depends on the "Rolling Ball" size, so all data analysis must use the same size Rolling Ball. This method is more reliable than Fourier transforms or manual peak-peak measurement. However, choosing the Region of Interest (*ROI*) for skeletonization and further calculation is subjective.

The image transform is written in ImageJ Macro code. For instructions on how to write and run ImageJ Macro code, please refer to the ImageJ website (http://rsb.info.nih.gov/ij/). Path names and files names will need to be adjusted for different computers.

The code includes three separate files: **GetMask.txt** generates a binary image with separated chondrogenic and non-chondrogenic regions. **Selquadr.txt** selects regions of 100 × 100 pixels. **SkeltonMeasure.txt** skeletonizes the image and calculates the number of peak and valley pixels.

(1) ***GetMask.txt***

```
---------------------------------------------------------------------------------------------------------------
open("C:\\Documents and Settings\\zhangyi\\Desktop\\2p42.jpg");
run("8-bit");
run("Size...", "width=640 height=512 constrain interpolate");
run("Brightness/Contrast...");
run("Enhance Contrast", "saturated=0.5");
resetMinAndMax();
run("Subtract Background...", "rolling=10 white");
run("Threshold");
run("Analyze Particles...", "size=10-finity circularity=0.00-1.00 show=Masks display exclude
summarize");
saveAs("Jpeg", "C:\\Documents and Settings\\zhangyi\\Desktop\\Mask of 2p42.jpg");
close();
close();
```

(2) ***Selquadr.txt*** Run this code four or more times to cover the area of a typical micromass image.

```
---------------------------------------------------------------------------------------------------------------
makeRectangle(207, 135, 250, 250);
---------------------------------------------------------------------------------------------------------------
```

(3) ***SkeletonMeasure.txt*** Run this code four or more times to cover the area of a typical micromass image.

```
---------------------------------------------------------------------------------------------------------------
run("Copy");
newImage("Untitled", "8-bit White", 250, 250, 1);
run("Paste");
run("Invert");
```

```
saveAs("Jpeg", "C:\\Documents and Settings\\zhangyi\\Desktop\\invert_2p42.jpg");
run("Invert");
run("Threshold");
run("Skeletonize");
saveAs("Jpeg", "C:\\Documents and Settings\\zhangyi\\Desktop\\2p42_sk1.jpg")
run("Measure");
close();
open("C:\\Documents and Settings\\zhangyi\\Desktop\\invert_2p42.jpg");
run("Threshold");
run("Invert");
run("Skeletonize");
saveAs("Jpeg", "C:\\Documents and Settings\\zhangyi\\Desktop\\2p42_sk2.jpg")
run("Measure");
close();
```

7.E ImageJ Macro Code to Calculate the Integrated Density of Alcian-Blue Staining in Micromass Culture

Chapter Five describes the method and purpose of the calculation of the integrated density of Alcian-blue staining.

INH.txt

```
open("C:\\Documents and Settings\\zhangyi\\1p22.jpg");
run("8-bit");
run("Size...", "width=640 height=512 constrain interpolate");
run("Brightness/Contrast...");
run("Enhance Contrast", "saturated=0.5");
resetMinAndMax();
run("Subtract Background...", "rolling=50 white");
run("Set Measurements...", " mean integrated limit redirect=None decimal=3");
run("Invert");
saveAs("Jpeg", "C:\\Documents and Settings\\zhangyi\\INH_1p22.jpg"),
run("Measure");
```

7.F Code for the Cell-Sorting Kinetics Simulation in Chapter Three

7.F.1 Introduction

Chapter Three describes my *Glazier-Graner-Hogeweg* (*GGH*) model of cell-sorting kinetics. Running a GGH simulation using CompuCell3D requires initial installation of the CC3D package (from www.compucell3d.org), followed by loading the appropriate CC3DML and/or Python scripts into the CC3D Player. My simulations employ both CC3DML and Python scripts. The CompuCell3D implementation consists of three files:

(1) ***ContSortingcontinous.xml*** contains a basic description of the GGH parameters (Eqs. (3.5) and (3.9)), such as the lattice size, simulation duration in Monte Carlo Steps (*MCS*), intrinsic Cell Motility (*Temperature*), definitions of cell types and adhesion energies between different types of cells and instructions on how to load the Volume Energy term (whose parameters the Python script will initialize). It also provides the values of k (*Contactspecificity*), J_0 (*offset*), and specifies the cadherin binding model (Eqs. (3.3), (3.3′) and (3.3″)).

(2) ***ContSortingcontinuous.py*** sets up the simulation (instantiating C++ and Python objects and implementing the main GGH loop), defines the cadherin expression range (for continuous cadherin-expression levels) or levels (for discrete cadherin-expression levels), and calculates the heterotypic boundary length (Eqs. (3.10'), (3.10″) and (3.10‴)).

(3) ***ContSortSteppables.py*** defines and manages transitions between cell types.

The listings include brief comments explaining the significance of the code modules and indicating how to change the parameters to implement the different simulations in this thesis.

For details about how to install CompuCell3D and how to run the code, refer to the CompuCell3D website www.compucell3d.org. In brief, load *ContSortingcontinous.xml* and *ContSortingcontinuous.py* into the *CompuCell3D Player* and adjust the setting of the Player for proper visualization and image recording.

7.F.2 Code

(1) *ContSortingcontinous.xml*

```
<CompuCell3D>
<Potts>
<Dimensions x="200" y="200" z="1"/> <!-- for a two-dimensional simulation-->
<Anneal>10</Anneal>
<Steps>1000000</Steps>
<Temperature>20</Temperature>
<Flip2DimRatio>1</Flip2DimRatio>
<Boundary_x>Periodic</Boundary_x>
<Boundary_y>Periodic</Boundary_y>
<RandomSeed>271617</RandomSeed>
<FlipNeighborMaxDistance>2.25</FlipNeighborMaxDistance>
</Potts>

<Plugin Name="Volume">
<TargetVolume>25</TargetVolume>
<LambdaVolume>25</LambdaVolume>
</Plugin>

<Plugin Name="CenterOfMass" />
```

```
<Plugin Name="CellType">
<CellType TypeName="Medium" TypeId="0"/>
<CellType TypeName="CadExpLevel1" TypeId="1"/>
</Plugin>

<Plugin Name="ContactLocalProduct">
<ContactSpecificity Type1="Medium" Type2="Medium">2</ContactSpecificity>
<ContactSpecificity Type1="Medium" Type2="CadExpLevel1">0</ContactSpecificity>
<ContactSpecificity Type1="CadExpLevel1" Type2="CadExpLevel1">0.02
        </ContactSpecificity>
<ContactFunctionType>Quadratic</ContactFunctionType>
<!-- other options are quadratic, Min, default type is linear -->
<EnergyOffset>16</EnergyOffset>
<Depth>2.25</Depth>
</Plugin>

<Steppable Type="BlobInitializer">
<Gap>0</Gap>
<Width>5</Width> <!-- cell size -->
<CellSortInit>no</CellSortInit>
<Radius>50</Radius> <!-- blob size -->
</Steppable>

</CompuCell3D>
```

(2) ***ContSortingcontinuous.py***

```
def mainfcn():

import sys
from os import environ
import string
sys.path.append(environ["PYTHON_MODULE_PATH"])

import SystemUtils
SystemUtils.setSwigPaths()
SystemUtils.initializeSystemResources()

# Import the PluginManager for Python
import CompuCellPython
import CompuCellAuxPython
import PlayerPython
from PyPluginsExamples import VolumeEnergyFunction
from PyPluginsExamples import SurfaceEnergyFunction
from PyPluginsExamples import MitosisPy
```

```
# This function wraps the plugin-initialization code.
     CompuCellPython.initializePlugins()

# Create a Simulator. This returns a Python object that wraps Simulator.
   sim = CompuCellPython.Simulator()

   simthread=PlayerPython.getSimthreadBasePtr();
   simthread.setSimulator(sim)
   simulationFileName=simthread.getSimulationFileName()
   print "simulationFileName=", simulationFileName

# Add the Python-specific extensions.
   reg = sim.getClassRegistry()

   CompuCellPython.parseConfig(simulationFileName, sim)

# Set up the Python Energy-function holder.
   extraEnergy=CompuCellAuxPython.EnergyFunctionPyWrapper()
   extraEnergy.setSimulator(sim)
   extraEnergy.setPotts(sim.getPotts())

   sim.getPotts().registerEnergyFunction(extraEnergy.getEnergyFunctionPyWrapperPtr())

   typeChangeWatcher=CompuCellAuxPython.TypeChangeWatcherPyWrapper()
   from PyPluginsExamples import TypeChangeWatcherExample
   typeChangeWatcherExample=TypeChangeWatcherExample(typeChangeWatcher)
   typeChangeWatcher.registerPyTypeChangeWatcher(typeChangeWatcherExample)

   sim.getPotts().getTypeTransition().registerTypeChangeWatcher(typeChangeWatcher)

   dim=sim.getPotts().getCellFieldG().getDim()
   print "dim=", dim

   sim.extraInit()
# After all CC3DML steppables and plugins have been loaded, we call extraInit to
# complete initialization.

   cSpecificityField=simthread.createFloatFieldPy(dim,"ContSpec")

# Initialize the contactspecifisity Field. This location in the code is important and must be
# called before preStartInit or the field list will not be initialized properly.

   simthread.preStartInit()
   sim.start()
   simthread.postStartInit()
```

```
    screenUpdateFrequency=simthread.getScreenUpdateFrequency()

    from PySteppables import SteppableRegistry

    steppableRegistry=SteppableRegistry()

    from ContSortSteppables import ContactLocalProductSteppable
    clpSteppable=ContactLocalProductSteppable(sim)
  # typeContactEnergyTable={0:0.0, 1:1.00, 2:12.00, 3:23.00}
  # The format is as follows:
  # type: N, e.g., 1:20.1234, 2:12.19.
  # type ContactEnergyTable={0:0.0, 1:15.00, 2:16.25, 3:17.50, 4:18.75, 5:20.0, 6:21.25,
  #                                  7:22.50, 8:23.75, 9:25.0}

    typeContactEnergyTable={0:0.0, 1:[1.0, 23.00]}
  # The format is as follows: real random number generated within the range:
  # Type: [N_min,N_max], e.g., 1:[20,30], 2:[40,50].
  # Continuous visualization shows expression levels not cell types.
    clpSteppable.setTypeContactEnergyTable(typeContactEnergyTable)
    clpSteppable.setInitMCS(20)
  # Here you set the MCS at which specificity/type reassignment takes place.
    clpSteppable.setMaxType(1)
  # Here you set the max type assignment.
    steppableRegistry.registerSteppable(clpSteppable)

  # For heterotypic boundary calculation at specific MCS (1).
     from ContSortSteppables import StepChecker
     stepDictionary={200:0, 1000:0, 2000:0, 5000:0, 10000:0, 20000:0, 50000:0, 100000:0,
     150000:0, 200000:0, 250000:0, 300000:0, 350000:0, 400000:0, 450000:0, 500000:0,
     550000:0, 600000:0, 650000:0, 700000:0, 750000:0, 800000:0, 850000:0, 900000:0,
     950000:0, 999800:0, 1000000:0} # put step numbers here in the form: step:0
     stepChecker=StepChecker()
     stepChecker.setStepDictionary(stepDictionary)

     from ContSortSteppables import ContactSpecVisualizationSteppable
contactVisSteppable=ContactSpecVisualizationSteppable(_simulator=sim,_frequency=100)
  # Here you change the frequency with which the Python-based visualizer is called.
    contactVisSteppable.setScalarField(cSpecificityField)

  # For heterotypic boundary calculation at specific MCS (2).
     contactVisSteppable.setStepChecker(stepChecker)
     steppableRegistry.registerSteppable(contactVisSteppable)
     from ContSortSteppables import HeterotypicBoundaryCalculator
     hbc=HeterotypicBoundaryCalculator(_simulator=sim,_frequency=200)
  # Change frequency here.
    hbc.setMaxType(1) # Here you have to set the maximum cell type
```

```
# The next two lines are necessary if you are using hbc.setScaleLocally(False).

# cadherinConcentrationList=[0,2.0,3.70] # List specificities here [N_type_1,
# N_type_2, ...].
# hbc.setCadherinConcentrationList(cadherinConcentrationList) # pass this list to
# steppable.
# hbc.setNMedium(1.2).
# Sets cadherin concentration for medium - Nmedium is 0 by default.
  hbc.setScaleLocally(True)
# If you setScaleLocally to true the boundary will be scaled on a pixel-by-pixel basis. This
# is important if you want to get "exact" scaling when each cell has a different specificity,
# N. However, if specificity is assigned on a type-by-type basis, setting or unsetting it does
# not matter and the result is the same as in the case where you calculate the boundary
# length with no scaling and scale the total boundary length later.

# For heterotypic boundary calculation at specific MCS (3).
  hbc.setStepChecker(stepChecker)

 steppableRegistry.registerSteppable(hbc)
 steppableRegistry.init(sim)
 steppableRegistry.start()

 for i in range(sim.getNumSteps()):
    sim.step(i)
    steppableRegistry.step(i)
    if not i % screenUpdateFrequency:
       simthread.loopWork(i)
       simthread.loopWorkPostEvent(i)
 sim.finish()
 steppableRegistry.finish(i)

 mainfcn()
```

(3) ***ContSortSteppables.py***

```
# Steppables

# This module contains examples of certain more and less useful steppables written in
# Python.
  from CompuCellPython import NeighborFinderParams
  import CompuCellPython
  from whrandom import random
  from whrandom import randint
  import types
  from PySteppables import *
```

```
import CompuCellAuxPython

class StepChecker:
  def __init__(self):
    self.stepDictionary=None
  def setStepDictionary(self,_dict):
    self.stepDictionary=_dict
  def checkIfStepInDictionary(self,_step):
    if self.stepDictionary.has_key(_step):
      return True
    else:
      return False

class ContactLocalProductSteppable(SteppablePy):
  def __init__(self,_simulator,_frequency=10):
    SteppablePy.__init__(self,_frequency)
    self.simulator=_simulator
    self.contactProductPlugin=CompuCellAuxPython.getContactLocalProductPlugin()
    self.inventory=self.simulator.getPotts().getCellInventory()
    self.mcsInit=1
    self.maxType=1
  def setTypeContactEnergyTable(self,_table):
    self.table=_table
  def setInitMCS(self,_mcs):
    if _mcs>=1:
      self.mcsInit=_mcs

  def setMaxType(self,_maxType):
    if _maxType>=1:
      self.maxType=_maxType

  def initializeTypes(self,_maxType):
    invItr=CompuCellPython.STLPyIteratorCINV()
    invItr.initialize(self.inventory.getContainer())
    invItr.setToBegin()
    cell=invItr.getCurrentRef()
    while (1):
      if invItr.isEnd():
        break
      cell=invItr.getCurrentRef()
      print "Blob Initializer CELL ID=",cell.id
      cell.type=randint(1,_maxType)
      invItr.next()

  def initializeSpecificity(self):
    invItr=CompuCellPython.STLPyIteratorCINV()
```

```
      invItr.initialize(self.inventory.getContainer())
      invItr.setToBegin()
      cell=invItr.getCurrentRef()

cProductDataAccessor=self.contactProductPlugin.getContactProductDataAccessorPtr()
      jVecItr=CompuCellAuxPython.jVecPyItr()
      while (1):
        if invItr.isEnd():
          break
          cell=invItr.getCurrentRef()
          jVec=cProductDataAccessor.get(cell.extraAttribPtr).jVec
      specificityObj=self.table[cell.type];
      if isinstance(specificityObj,types.ListType):
          jVec.set(0,(specificityObj[1]-specificityObj[0])*random())
        else:
      jVec.set(0,specificityObj)
      invItr.next()

  def start(self):
    self.initializeSpecificity()
  def step(self,mcs):
    if mcs==self.mcsInit:
      self.initializeTypes(self.maxType)
      self.initializeSpecificity()


from PlayerPython import fillScalarValue as conSpecSet
class ContactSpecVisualizationSteppable(SteppablePy):
  def __init__(self,_simulator,_frequency=10):
    SteppablePy.__init__(self,_frequency)
    self.simulator=_simulator
    self.contactProductPlugin=CompuCellAuxPython.getContactLocalProductPlugin()
    self.cellFieldG=self.simulator.getPotts().getCellFieldG()
    self.dim=self.cellFieldG.getDim()

  def setScalarField(self,_field):
    self.scalarField=_field

  def setStepChecker(self, _stepChecker):
    self.stepChecker=_stepChecker

  def start(self):pass

  def step(self,mcs):
    if not self.stepChecker.checkIfStepInDictionary(mcs):
      return
```

```
 cProductDataAccessor=self.contactProductPlugin.getContactProductDataAccessorPtr()
 cell=None
 cellFieldG=self.cellFieldG
 for x in xrange(self.dim.x):
    for y in xrange(self.dim.y):
       for z in xrange(self.dim.z):
          pt=CompuCellPython.Point3D(x,y,z)
          cell=cellFieldG.get(pt)
          if cell:
             jVec=cProductDataAccessor.get(cell.extraAttribPtr).jVec
             conSpecSet(self.scalarField,x,y,z,jVec.get(0))
          else:
             conSpecSet(self.scalarField,x,y,z,0.0)

import sys
class HeterotypicBoundaryCalculator(SteppablePy):
   def __init__(self,_simulator,_frequency=1):
      SteppablePy.__init__(self,_frequency)
      self.simulator=_simulator
      self.cellFieldG=self.simulator.getPotts().getCellFieldG()
      self.dim=self.cellFieldG.getDim()
      self.boundaryStrategy=CompuCellPython.BoundaryStrategy.getInstance()

self.maxNeighborIndex=self.boundaryStrategy.getMaxNeighborIndexFromDepth(1.1)
      self.maxType=0
      self.coreFileName="HeterotypicBoundary"
      self.extension="dat"
      self.specificityList=[]
      self.contactProductPlugin=CompuCellAuxPython.getContactLocalProductPlugin()
      self.NMedium=0.0
      self.scaleLocally=0

   def setStepChecker(self, _stepChecker):
      self.stepChecker=_stepChecker

   def setScalarField(self,_field):
      self.scalarField=_field

   def setMaxType(self,_maxType):
      self.maxType=_maxType
      self.boundaryLengthMap={}
      for i in xrange(self.maxType+1):
         for j in xrange(self.maxType+1):
            self.boundaryLengthMap[self.index(i,j)]=0
```

```
    def setOutputFileName(self,_fileName):
  self.fileName=_fileName

def setNMedium(self,_N):
  self.NMedium=_N

def setScaleLocally(self,_scale):
  self.scaleLocally=_scale

def setCadherinConcentrationList(self,_list):
  self.cadherinConcentrationList=_list

def index(self,type1,type2):
  return type1*(self.maxType+1)+type2

def outputResults(self,mcs,_scaleFlag=""):
  fulfileName=self.coreFileName+_scaleFlag+"_"+str(mcs)+"."+self.extension
  file=open(fulfileName,"w")
  file.write("Format: type1,type2 boundary(type1,type2)\n")
  for type1 in xrange(self.maxType+1):
    for type2 in xrange(self.maxType+1):
file.write("%d %d %f\n" % (type1, type2, self.boundaryLengthMap[self. index(type1,
type2)]))
print "type1=",type1,"type2=", type2,"boundary =", self. boundaryLengthMap[self.
index(type1, type2)]

    file.close()

  def start(self):pass

  def areCellsDifferent(self,_cell1,_cell2):
    if (_cell1 and _cell2 and _cell1.id!=_cell2.id) or (not _cell1 and _cell2) or (_cell1
      and  not _cell2):
      return 1
    else:
      return 0

  def step(self,mcs):
    if not self.stepChecker.checkIfStepInDictionary(mcs):
    return


cProductDataAccessor=self.contactProductPlugin.getContactProductDataAccessorPtr()
    cell=None
    cellFieldG=self.cellFieldG
    nCell=None
```

```
# nPt=CompuCellPython.Point3D(0,0,0)
# pixelNeighbor=self.boundaryStrategy.getNeighborDirect(nPt,0)
    type1=0
    type2=0
    N1=0.0
    N2=0.0
    scalingFactor=0.0

# Resetting boundaries
    for i in xrange(self.maxType+1):
      for j in xrange(self.maxType+1):
        self.boundaryLengthMap[self.index(i,j)]=0

    for x in xrange(self.dim.x):
      for y in xrange(self.dim.y):
        for z in xrange(self.dim.z):
          pt=CompuCellPython.Point3D(x,y,z)
          cell=cellFieldG.get(pt)

          if not cell:
            type1=0
            N1=self.NMedium
          else:
            type1=cell.type
            N1=cProductDataAccessor.get(cell.extraAttribPtr).jVec.get(0)

# Print "cell.id=",cell.id
          for i in xrange (self.maxNeighborIndex+1):
            pixelNeighbor=self.boundaryStrategy.getNeighborDirect(pt,i)
            if pixelNeighbor.distance: # neighbor is valid
              nCell=cellFieldG.get(pixelNeighbor.pt)
              if CompuCellPython.areCellsDifferent(nCell,cell):

                if not nCell:
                  type2=0
                  N2=self.NMedium
                else:
                  type2=nCell.type
                  N2=cProductDataAccessor.get(nCell.extraAttribPtr).jVec.get(0)

                if self.scaleLocally:
                  scalingFactor=(N1-N2)**2
                else:
                  scalingFactor=1.0

      self.boundaryLengthMap[self.index(type1,type2)]+=scalingFactor
```

```
        if self.scaleLocally:
          self.outputResults(mcs,"_locally_scaled_")
        else:
          self.outputResults(mcs)

        if not self.scaleLocally:
          self.scaleBoundaryLength(mcs,"_globally_scaled_")

    def scaleBoundaryLength(self,mcs,_scaleFlag):
      fulfileName=self.coreFileName+_scaleFlag+str(mcs)+"."+self.extension
      file=open(fulfileName,"w")
      file.write("Format: type1,type2 boundary(type1,type2)\n")

      print "SCALED BOUNDARY LENGTH"
      for type1 in xrange(self.maxType+1):
        for type2 in xrange(self.maxType+1):
          scalingFactor=0.0
          if type1==type2:
            scalingFactor=1.0
          else:
            scalingFactor=(self.cadherinConcentrationList[type1]-
                           self.cadherinConcentrationList [type2]) **2

          scaledLength=self.boundaryLengthMap[self.index(type1,type2)]*scalingFactor
          file.write("%d %d %f\n" % (type1,type2,scaledLength))
          print "type1=",type1," type2=",type2," boundary=",scaledLength
```

7.G Code for the Somite-Segmentation Simulations in Chapter Four

7.G.1 Introduction

The CC3DML file (***somite.xml***) contains the basic description of GGH parameters, such as lattice size, simulation duration in Monte Carlo Steps, Intrinsic Cell Motility (*Temperature*), definitions of adhesion energies between different types of cells, instructions to load Volume

and Surface energy terms (the parameters of which Python script will initialize) and modules tracking cells' centers of mass and a Cell Lattice initialization routine (UniformInitializer).

The two Python scripts include one, ***somite.py*** that sets up the simulation (instantiating C++ and Python objects and implementing the main GGH loop) and a script that contains implementations of *Steppables* (***somiteSteppables.py***). Steppables define and manage transitions between cell types (SomiteMaskSteppable) and changes in Volume and Surface parameters (SomiteVolumeSurfaceSteppable).

The listings include brief comments explaining the significance of the code modules and indicating how to change the parameters to implement the different simulations. For convenience, complete files for implementing the somitogenesis simulations are also available for download from: http://compucell3d.org/Models/somiteSimulationFiles.tgz.

7.G.2 Somitogenesis Code

(1) *somite.py*

```
    def mainfcn():
  # Initialization section.
    import sys
    from os import environ
    import string
    sys.path.append(environ["PYTHON_MODULE_PATH"])

    import SystemUtils
    SystemUtils.setSwigPaths()
    SystemUtils.initializeSystemResources()
```

```
  import CompuCell
  import PlayerPython
# This function wraps the plugin-initialization code.
  CompuCell.initializePlugins()

# Create a Simulator. This section returns a Python object that wraps simulator.
  sim = CompuCell.Simulator()

  simthread=PlayerPython.getSimthreadBasePtr();
  simthread.setSimulator(sim)
  simulationFileName=simthread.getSimulationFileName()

# Add the Python-specific extensions.
  reg = sim.getClassRegistry()

  CompuCell.parseConfig(simulationFileName, sim)
# End of Initialization section.
# Registering objects that will allow adding cell attributes during simulation runtime.
# For more information see CompuCell3D Python scripting tutorials at:
# www.compucell3d.org.
  from CompuCell import PyAttributeAdder
  from PyListAdder import ListAdder
  from sys import getrefcount
  adder=PyAttributeAdder()
  adder.registerRefChecker(getrefcount)
  listAdder=ListAdder()
  adder.registerAdder(listAdder)
  potts=sim.getPotts()
  potts.registerAttributeAdder(adder.getPyAttributeAdderPtr())

# Further initialization of Player and CompuCell3D C++ code.
  dim=sim.getPotts().getCellFieldG().getDim()
# After all CC3DML steppables and plugins have been loaded,
# we call extraInit to complete initialization.
  sim.extraInit()
  simthread.preStartInit()
  sim.start()
  simthread.postStartInit()
  screenUpdateFrequency=simthread.getScreenUpdateFrequency()

# Instantiating and registering Python-based plugins.
# Notice that all Python steppables are registered with steppableRegistry,
# e.g., steppableRegistry.registerSteppable(somiteMaskSteppable).
  from PySteppables import SteppableRegistry
```

```
    steppableRegistry=SteppableRegistry()

    from somiteSteppables import SomiteMaskSteppable
    somiteMaskSteppable=SomiteMaskSteppable(_simulator=sim,_frequency=10)
  # Sweep as [T0, T0+T, T0+2T],
  # T0=2000, 3000, 400, 5000, 6000; T=1000, 2000, 3000, 4000, 5000;
  # Specify here the MCS at which transitions take place.
    transitionStepsList=[5000, 7000, 9000]
    somiteMaskSteppable.setTransitionStepsList(transitionStepsList)
    somiteMaskSteppable.blur(0.0)
    steppableRegistry.registerSteppable(somiteMaskSteppable)

    from somiteSteppables import SomiteVolumeSurfaceSteppable
    somiteVolumeSurfaceSteppable=SomiteVolumeSurfaceSteppable(\
    _simulator=sim,_frequency=100)
  # Specify here the max MCS at which changes take place - this way
  # code in this steppable does not execute after all transitions have taken place.
    somiteVolumeSurfaceSteppable.setMaxTransitionStep(\
    somiteMaskSteppable.getMaxTransitionStep())
    steppableRegistry.registerSteppable(somiteVolumeSurfaceSteppable)

    steppableRegistry.init(sim)
    steppableRegistry.start()

  # Main GGH-algorithm loop.
    for i in range(sim.getNumSteps()):
      sim.step(i)
      steppableRegistry.step(i)
      if not i % screenUpdateFrequency:
        simthread.loopWork(i)
        simthread.loopWorkPostEvent(i)
    sim.finish()
    steppableRegistry.finish()

   mainfcn()
```

(2) ***somite.xml***

```
    <CompuCell3D>
    <!-- This section defines basic parameters of the GGH model.-->
    <Potts>
    <Dimensions x="170" y="1" z="450"/>
    <Anneal>1</Anneal>
    <Steps>100</Steps>
    <Temperature>100</Temperature>
```

```
<Flip2DimRatio>1</Flip2DimRatio>
</Potts>

<!-- Each CC3DML file must include a list
 of all cell types used in the simulation.-->
 <Plugin Name="CellType">
<CellType TypeName="Medium" TypeId="0"/>
<CellType TypeName="ncam" TypeId="1"/>
<CellType TypeName="ncad" TypeId="2" />
<CellType TypeName="eph-rec" TypeId="3"/>
<CellType TypeName="eph-rec-ncam" TypeId="4" />
<CellType TypeName="eph-rec-ncad" TypeId="5" />
<CellType TypeName="eph-lig-ncam" TypeId="6" />
<CellType TypeName="eph-lig-ncad" TypeId="7" />
<CellType TypeName="eph-lig" TypeId="8" />
<CellType TypeName="psm" TypeId="9" />
 </Plugin>

 <!-- This plugin tells the Player which lattice
 projection should be displayed at the start.-->
<Plugin Name="PlayerSettings">
<Project2D XZProj="1"/>
<InitialProjection Projection="xz"/>
</Plugin>

<!-- Additional initialization of volume and surface target values
and lambdas is required. This is done in the Python scripts.-->
<Plugin Name="VolumeLocalFlex"/>
<Plugin Name="SurfaceLocalFlex"/>

 <!-- List of contact energies between different cell types.-->
<Plugin Name="Contact">
<Energy Type1="Medium" Type2="Medium">0</Energy>
<Energy Type1="Medium" Type2="ncam">15</Energy>
<Energy Type1="Medium" Type2="ncad">15</Energy>
<Energy Type1="Medium" Type2="eph-rec">15</Energy>
<Energy Type1="Medium" Type2="eph-rec-ncam">15</Energy>
<Energy Type1="Medium" Type2="eph-rec-ncad">15</Energy>
<Energy Type1="Medium" Type2="eph-lig-ncam">15</Energy>
<Energy Type1="Medium" Type2="eph-lig-ncad">15</Energy>
<Energy Type1="Medium" Type2="eph-lig">15</Energy>
<Energy Type1="Medium" Type2="psm">15</Energy>
<Energy Type1="ncam" Type2="ncam">-20.25</Energy>
<Energy Type1="ncam" Type2="ncad">-24</Energy>
<Energy Type1="ncam" Type2="eph-rec">-20.25</Energy>
<Energy Type1="ncam" Type2="eph-rec-ncam">-20.25</Energy>
```

```
<Energy Type1="ncam" Type2="eph-rec-ncad">-24</Energy>
<Energy Type1="ncam" Type2="eph-lig-ncam">-20.25</Energy>
<Energy Type1="ncam" Type2="eph-lig-ncad">-24</Energy>
<Energy Type1="ncam" Type2="eph-lig">-20.25</Energy>
<Energy Type1="ncam" Type2="psm">-20.25</Energy>
<Energy Type1="ncad" Type2="ncad">-38.44</Energy>
<Energy Type1="ncad" Type2="eph-rec">-24</Energy>
<Energy Type1="ncad" Type2="eph-rec-ncam">-24</Energy>
<Energy Type1="ncad" Type2="eph-rec-ncad">-38.44</Energy>
<Energy Type1="ncad" Type2="eph-lig-ncam">-24</Energy>
<Energy Type1="ncad" Type2="eph-lig-ncad">-38.44</Energy>
<Energy Type1="ncad" Type2="eph-lig">-24</Energy>
<Energy Type1="ncad" Type2="psm">-38.44</Energy>
<Energy Type1="eph-rec" Type2="eph-rec">-20.25</Energy>
<Energy Type1="eph-rec" Type2="eph-rec-ncam">-20.25</Energy>
<Energy Type1="eph-rec" Type2="eph-rec-ncad">-24</Energy>
<Energy Type1="eph-rec" Type2="eph-lig-ncam">-20.25</Energy>
<Energy Type1="eph-rec" Type2="eph-lig-ncad">-24.0</Energy>
<Energy Type1="eph-rec" Type2="eph-lig">-20.25</Energy>
<Energy Type1="eph-rec" Type2="psm">-20.25</Energy>
<Energy Type1="eph-rec-ncam" Type2="eph-rec-ncam">-20.25</Energy>
<Energy Type1="eph-rec-ncam" Type2="eph-rec-ncad">-24</Energy>
<Energy Type1="eph-rec-ncam" Type2="eph-lig-ncam">-20.25</Energy>
<Energy Type1="eph-rec-ncam" Type2="eph-lig-ncad">-24.0</Energy>
<Energy Type1="eph-rec-ncam" Type2="eph-lig">-20.25</Energy>
<Energy Type1="eph-rec-ncam" Type2="psm">-20.25</Energy>
<Energy Type1="eph-rec-ncad" Type2="eph-rec-ncad">-38.44</Energy>
<Energy Type1="eph-rec-ncad" Type2="eph-lig-ncam">-24</Energy>
<Energy Type1="eph-rec-ncad" Type2="eph-lig-ncad">-38.44</Energy>
<Energy Type1="eph-rec-ncad" Type2="eph-lig">-24.0</Energy>
<Energy Type1="eph-rec-ncad" Type2="psm">-38.44</Energy>
<Energy Type1="eph-lig-ncam" Type2="eph-lig-ncam">-20.25</Energy>
<Energy Type1="eph-lig-ncam" Type2="eph-lig-ncad">-24</Energy>
<Energy Type1="eph-lig-ncam" Type2="eph-lig">-20.25</Energy>
<Energy Type1="eph-lig-ncam" Type2="psm">-20.25</Energy>
<Energy Type1="eph-lig-ncad" Type2="eph-lig-ncad">-38.44</Energy>
<Energy Type1="eph-lig-ncad" Type2="eph-lig">-24</Energy>
<Energy Type1="eph-lig-ncad" Type2="psm">-38.44</Energy>
<Energy Type1="eph-lig" Type2="eph-lig">-20.25</Energy>
<Energy Type1="eph-lig" Type2="psm">-20.25</Energy>
<Energy Type1="psm" Type2="psm">-20.25</Energy>
<Depth>2.3</Depth>
 </Plugin>

 <!-- This plugin tracks the center of mass of each cell
 and is necessary for laying out the prepattern of cadherin expression.-->
```

```
    <Plugin Name="CenterOfMass"/>

    <!-- UniformInitializer lays out the initial pattern of cells. Here,
    a rectangular block corresponding to the presomitic mesoderm (PSM).-->
    <Steppable Type="UniformInitializer">
       <Region>
          <BoxMin x="35" y="0" z="30"/>
          <BoxMax x="135" y="1" z="430"/>
          <Gap>0</Gap>
          <Width>5</Width>
         <Types>psm</Types>
       </Region>
    </Steppable>
    </CompuCell3D>
```

(3) ***somiteSteppables.py***

```
    from PySteppables import *
    import CompuCell
    import sys
    import CompuCell
    import random

  # The function forEachCellInInventory takes as arguments the inventory of cells
  # and a function that will operate on a single cell.
  # It runs singleCellOperation on each cell from the cell inventory.
    def forEachCellInInventory(inventory,singleCellOperation):
    invItr=CompuCell.STLPyIteratorCINV()
    invItr.initialize(inventory.getContainer())
    invItr.setToBegin()
    cell=invItr.getCurrentRef()
    while (not invItr.isEnd()):
      cell=invItr.getCurrentRef()
      singleCellOperation(cell)
      invItr.next()

  # TypeTransition is a class that describes
  # cell-type transitions (self.typeIdSource, self.typeIdTarget)
  # and at what time (in MCS) the transition should take place.
    class TypeTransition:
    def __init__(self,_typeIdSource,_typeIdTarget,_step):
      self.typeIdSource=_typeIdSource
      self.typeIdTarget=_typeIdTarget
      self.step=_step
```

```
# The SomiteMaskSteppable defines a set of masks that describe cell types.
# Overlaying a mask is equivalent to defining new type transitions for a given cell.
# Masks are overlaid before simulation begins, which is why fixed mask coordinates work
# (e.g., self.x_rect_low=45). As discussed in the text, the development of the prepattern of
# cadherin expression can be thought of as a series of cell-type transitions.
  class SomiteMaskSteppable(SteppablePy):
  def __init__(self,_simulator,_frequency=1):
    SteppablePy.__init__(self,_frequency)
    self.simulator=_simulator
    self.cellFieldG=self.simulator.getPotts().getCellFieldG()
    self.dim=self.cellFieldG.getDim()
    self.inventory=self.simulator.getPotts().getCellInventory()
    self.typeNameTable={"Medium":0,"AL":1,"RH":2,"3":3,"4":4,"5":5,\
                        "6":6,"7":7,"8":8,"PSM":9}

# Base mask parameters.
    self.z_base_low=30
    self.z_base_size=100
# mask rectangle parameters.
    self.x_rect_low=45
    self.z_rect_low=40
    self.x_rect_size=80
    self.z_rect_size=80
# mask0 parameters.
    self.z_low_mask0=30
    self.z_size_mask0=10
# mask1 parameters.
    self.z_low_mask1=40
    self.z_size_mask1=40
# mask2 parameters.
    self.z_low_mask2=80
    self.z_size_mask2=40
# mask3 parameters.
    self.z_low_mask3=120
    self.z_size_mask3=10
# The above determine the shifts in the masks' z_low positions.
# They should be applied to all masks in the correct order.
    self.shift=100
    self.maskMargin=10
    self.stepForTransition=0
    self.transitionStepsList=[]
    self.maxTransitionStep=0
    self.sigmaBlur=0.0

  def getMaxTransitionStep(self):
    return self.maxTransitionStep
```

```
  def setTransitionStepsList(self,_transitionStepsList):
    self.transitionStepsList=_transitionStepsList
    self.maxTransitionStep=max(self.transitionStepsList)

# When overlaying a mask, attach to each cell a transition from its current type to a
# target type. Later, at the transition, simply read from the attached list of transitions and
# perform those for which the current time (in MCS) matches the times defined in the
# transition-description list.

# The functions below implement a series of masks that are used to construct
# the prepattern.
  def maskBase(self,cell,xCM,yCM,zCM,attrib):
    if (zCM >= self.z_base_low and zCM<self.z_base_low+self.z_base_size):
      sourceId=cell.type
      cell.type=self.typeNameTable["AL"]
      # To record a type transition.
      attrib.append(TypeTransition(sourceId,cell.type,self.stepForTransition))

  def maskRectangle(self,cell,xCM,yCM,zCM,attrib):
    if(xCM>=self.x_rect_low and xCM <self.x_rect_low+self.x_rect_size \
    and zCM >= self.z_rect_low and zCM<self.z_rect_low+self.z_rect_size and\
    cell.type==self.typeNameTable["AL"]):
      sourceId=cell.type
      cell.type=self.typeNameTable["RH"]
      attrib.append(TypeTransition(sourceId,cell.type,self.stepForTransition))

  def mask0(self,cell,xCM,yCM,zCM,attrib):
    if(zCM>=self.z_low_mask0 and zCM <self.z_low_mask0+self.z_size_mask0):
      if(cell.type==self.typeNameTable["AL"]):
        sourceId=cell.type
        cell.type=self.typeNameTable["3"]
        attrib.append(TypeTransition(sourceId,cell.type,\
        self.stepForTransition))

  def mask1(self,cell,xCM,yCM,zCM,attrib):
    if(zCM>=self.z_low_mask1 and zCM <self.z_low_mask1+self.z_size_mask1):
      if(cell.type==self.typeNameTable["AL"]):
        sourceId=cell.type
        cell.type=self.typeNameTable["4"]
        attrib.append(TypeTransition(sourceId,cell.type,\
  self.stepForTransition))
      elif(cell.type==self.typeNameTable["RH"]):
        sourceId=cell.type
        cell.type=self.typeNameTable["5"]
        attrib.append(TypeTransition(sourceId,cell.type,\
```

```
                self.stepForTransition))

  def mask2(self,cell,xCM,yCM,zCM,attrib):
    if(zCM>=self.z_low_mask2-self.maskMargin and zCM \
    <self.z_low_mask2+self.z_size_mask2):
      if(cell.type==self.typeNameTable["AL"]):
        sourceId=cell.type
        cell.type=self.typeNameTable["6"]
        attrib.append(TypeTransition(sourceId,cell.type,\
        self.stepForTransition))
      elif(cell.type==self.typeNameTable["RH"]):
        sourceId=cell.type
        cell.type=self.typeNameTable["7"]
        attrib.append(TypeTransition(sourceId,cell.type,\
        self.stepForTransition))

  def mask3(self,cell,xCM,yCM,zCM,attrib):
    if(zCM>=self.z_low_mask3 and zCM <self.z_low_mask3+self.z_size_mask3):
      sourceId=cell.type
      cell.type=self.typeNameTable["8"]
      attrib.append(TypeTransition(sourceId,cell.type,self.stepForTransition))

  def maskPSM(self,cell,xCM,yCM,zCM,attrib):
    cell.type=self.typeNameTable["PSM"]

  def blur(self,_sigmaBlur):
    self.sigmaBlur=_sigmaBlur

# The imposeMask function is a Closure that takes as its first argument mask and returns a
# function that operates on a single cell, making use of the mask object. For more
# information on Closures in Python. Please consult, e.g., the Python Cookbook, or search
# using a web search-engine with “python Closure” as keywords. Notice that the result
# (return imposeMaskForSingleCell) is a function that operates on a single cell exactly as
# required by the forEachCellInInventory algorithm.

  def imposeMask(self,mask):
    def imposeMaskForSingleCell(cell):
      xCM=cell.xCM/float(cell.volume)
      yCM=cell.yCM/float(cell.volume)
      zCM=cell.zCM/float(cell.volume)
      pyAttrib=CompuCell.getPyAttrib(cell)
      mask(cell,xCM,yCM,zCM,pyAttrib)
    return imposeMaskForSingleCell

# Overlaying masks can be coded very elegantly in just two lines making use of the
# imposeMask Closure and the forEachCellInInventory algorithm.
```

```
   def overlayMasks(self,mask):
      imposeMaskFunction=self.imposeMask(mask)
      forEachCellInInventory(inventory=self.inventory,\
           singleCellOperation=imposeMaskFunction)

# The singleCellTransition Closure returns a function that operates on a single cell and
# implements a type transition for a single cell. A Closure is required because of the extra
# argument _mcs in addition to the cell variable.
   def singleCellTransition(self,_mcs):
      def transition(cell):
         pyAttrib=CompuCell.getPyAttrib(cell)
         attribSize=len(pyAttrib)
         if(attribSize>1):
            for i in xrange(1,attribSize):
# The transition will take place if and only if the current time (in MCS) (_mcs) matches the
# step variable defined in the transition object.
            if(pyAttrib[i].step==_mcs):
               cell.type=pyAttrib[i].typeIdTarget
            return transition

# The doTransitions function iterates over each cell and makes type transitions as
#  necessary.
      def doTransitions(self,_mcs):
      singleCellTransitionFunction=self.singleCellTransition(_mcs)
      forEachCellInInventory(inventory=self.inventory,\
           singleCellOperation=singleCellTransitionFunction)

# The following implements the misdifferentiation of cells due to inaccurate positional
# information. The doBlurSingleCell Closure returns a function operating on a single cell
# object that calculates the center of mass cCM of a given cell, adds a random vector V to it
# (the coordinates of which are chosen from a Gaussian distribution) and changes the type
# of the current cell to the type of a cell located at cCM+V (or leaves the cell type
# untouched, if the cell at cCM+V happens to be medium).

   def doBlurSingleCell(self,_mcs):
      def blurFunction(cell):
         xCM=cell.xCM/float(cell.volume)
         yCM=cell.yCM/float(cell.volume)
         zCM=cell.zCM/float(cell.volume)
          if self.sigmaBlur!=0.0:
# print "Will do the bluring ",random.gauss(0.0,self.sigmaBlur)
         xCM+=random.gauss(0.0,self.sigmaBlur)
         yCM+=random.gauss(0.0,self.sigmaBlur)
         zCM+=random.gauss(0.0,self.sigmaBlur)
         pt=CompuCell.Point3D()
         pt.x=int(xCM)
```

```
      pt.y=int(yCM)
      pt.z=int(zCM)
      neighborCell=self.cellFieldG.get(pt)
    if neighborCell:
       cell.type=neighborCell.type
       return blurFunction

# Iterate over each cell and apply the blur (misdifferentiation).
  def doBlur(self,_mcs):
     doBlurSingleCellFunction=self.doBlurSingleCell(_mcs)
     forEachCellInInventory(inventory=self.inventory,\
     singleCellOperation=doBlurSingleCellFunction)

# This function runs before the simulation begins. It lays out the cadherin prepattern. i.e., it
# initializes a set of potential type transitions for each cell.
  def start(self):
     if(len(self.transitionStepsList)<3):
        print "You need to provide list with MC steps \
        at which spin reassignment takes place"
        sys.exit()
# Initialize the anterior compartment (low z coordinates) initial prepattern.
        self.stepForTransition=self.transitionStepsList[0]
        self.overlayMasks(self.maskBase)
        self.overlayMasks(self.maskRectangle)
        self.overlayMasks(self.mask0)
        self.overlayMasks(self.mask1)

# Initialize transitions for anterior (low z) middle (medium z) and posterior (high z) somite
# cells. Notice the progression from low values of z to higher values of z by manipulating
# class variables, such as self.z_base_low and self.z_low_mask0 and shifting them for each
# of the transition steps.
        for i in xrange(1,3):
         self.stepForTransition=self.transitionStepsList[i]
         self.overlayMasks(self.mask2)
         self.overlayMasks(self.mask3)
# z_low for mask 2 and 3 is shifted after the call to overlay masks.
         self.z_low_mask2+=self.shift
         self.z_low_mask3+=self.shift
         self.z_base_low+=self.shift
         self.z_rect_low+=self.shift
         self.overlayMasks(self.maskBase)
         self.overlayMasks(self.maskRectangle)
         self.z_low_mask0+=self.shift
         self.z_low_mask1+=self.shift
         self.overlayMasks(self.mask0)
         self.overlayMasks(self.mask1)
```

```
# Because the overlayMasks function has the side effect of changing cell types, we need to
# reset the cell types after imposing the masks. At the beginning of the simulation all the
# cells are of type PSM (presomitic mesoderm).
        self.overlayMasks(self.maskPSM)
# This function runs every 10 MCS,
# see somiteMaskSteppable=SomiteMaskSteppable(_simulator=sim,_frequency=10) in
# somite.py.
      def step(self,mcs):
      if(mcs<=self.maxTransitionStep):
        if mcs in self.transitionStepsList:
          self.doTransitions(mcs)
          self.doBlur(mcs)
          return
        return

# SomiteVolumeSurfaceSteppable is responsible for periodically assigning new volume
# and surface energy parameters. These parameters are local to each cell, so when cells
# change types these parameters need to be updated as well. I have hard-coded the
# parameters (targerVolume, lambda) (targetSurface, lambda).

   class SomiteVolumeSurfaceSteppable(SteppablePy):
      def __init__(self,_simulator,_frequency=1):
      SteppablePy.__init__(self,_frequency)
      self.simulator=_simulator
      self.cellFieldG=self.simulator.getPotts().getCellFieldG()
      self.dim=self.cellFieldG.getDim()
      self.inventory=self.simulator.getPotts().getCellInventory()
      self.maxTransitionStep=0
# Format type:[targetVolume,lambda], example 2:[25.0,20.0].
      self.typeVolumeParamMap={1:[25.0,20.0], 2:[25.0,20.0],3:[36.0,20.0], \
                                    4:[36.0,20.0],5:[16.0,20.0],6:[36.0,20.0],7:[16.0,20.0],
                                    8:[36.0,20.0],9:[25.0,20.0]}
# Format type:[targetSurface,lambda], example 2:[20.0,20.0].
      self.typeSurfaceParamMap={1:[20.0,20.0],2:[20.0,20.0],3:[24.0,20.0],4:[24.0,20.0],\
                                    5:[16.0,20.0],6:[24.0,20.0],7:[16.0,20.0],8:[24.0,20.0],
                                    9:[20.0,20.0]}

      def setMaxTransitionStep(self,_maxTransitionStep):
      self.maxTransitionStep=_maxTransitionStep

# At the beginning of the simulation, all cells have these volume parameters.
      def volumeInitSet(self,cell):
      cell.targetVolume=25.0
      cell.lambdaVolume=20.0
# At the beginning of the simulation, all cells have these surface parameters.
      def surfaceInitSet(self,cell):
```

```
      cell.targetSurface=20.0
    cell.lambdaSurface=20.0

# At later stages, the volume and surface parameters will change using
# self.typeVolumeParamMap and self.typeSurfaceParamMap.
      def volumeParamSet(self,cell):
      par=self.typeVolumeParamMap[cell.type]
      cell.targetVolume=par[0]
      cell.lambdaVolume=par[1]

      def surfaceParamSet(self,cell):
      par=self.typeSurfaceParamMap[cell.type]
      cell.targetSurface=par[0]
      cell.lambdaSurface=par[1]

      def setParameters(self,paramSetFcn):
      forEachCellInInventory(inventory=self.inventory,\
           singleCellOperation=paramSetFcn)

      def start(self):
      self.setParameters(self.volumeInitSet)
      self.setParameters(self.surfaceInitSet)

# This function is run every 100 MCS,
# see somiteVolumeSurfaceSteppable = SomiteVolumeSurfaceSteppable(_simulator=sim,
# _frequency=100) in somte.py. Notice that this function runs whether a transition takes
# place or not, which is redundant, but makes the code easier to read.
      def step(self,mcs):
      if(mcs<=self.maxTransitionStep):
        self.setParameters(self.volumeParamSet)
        self.setParameters(self.surfaceParamSet)
      return
```

8. BIBLIOGRAPHY

1. Adams, C.L., Chen, Y.T., Smith, S.J., Nelson, W.J., 1998. Mechanisms of epithelial cell-cell adhesion and cell compaction revealed by high-resolution tracking of E-cadherin-green fluorescent protein. *The Journal of Cell Biology* **142**, 1105-1119.
2. Adams, C.L., Nelson, W.J., 1998. Cytomechanics of cadherin-mediated cell-cell adhesion. *Current Opinion in Cell Biology* **10**, 572-577.
3. Adams, D.S., Robinson, K.R., Fukumoto, T., Yuan, S., Albertson, R.C., Yelick, P., Kuo, L., McSweeney, M., Levin, M., 2006. Early, H+-V-ATPase-dependent proton flux is necessary for consistent left-right patterning of non-mammalian vertebrates. *Development* **133**, 1657-1671.
4. Afonin, B., Ho, M., Gustin, J.K., Meloty-Kapella, C., Domingo, C.R., 2006. Cell behaviors associated with somite segmentation and rotation in *Xenopus laevis*. *Developmental Dynamics* **235**, 3268-3279.
5. Angres, B., Barth, A., Nelson, W.J., 1996. Mechanism for transition from initial to stable cell-cell adhesion: kinetic analysis of E-cadherin-mediated adhesion using a quantitative adhesion assay. *The Journal of Cell Biology* **134**, 549-557.
6. Aulehla, A., Herrmann, B.G., 2004. Segmentation in vertebrates: clock and gradient finally joined. *Genes & Development* **18**, 2060-2067.
7. Aulehla, A., Pourquié, O., 2006. On periodicity and directionality of somitogenesis. *Anatomy and Embryology* **211**, S3-S8.
8. Aulehla, A., Wehrle, C., Brand-Saberi, B., Kemler, R., Gossler, A., Kanzler, B., Herrmann, B.G., 2003. *Wnt3a* plays a major role in the segmentation clock

controlling somitogenesis. *Developmental Cell* **4**, 395-406.

9. Baker, R.E., Schnell, S., Maini, P.K., 2003. Formation of vertebral precursors: past models and future predictions. *Journal of Theoretical Medicine* **5**, 23-35.
10. Baker, R.E., Schnell, S., Maini, P.K., 2006. A clock and wavefront mechanism for somite formation. *Developmental Biology* **293**, 116-126.
11. Baker, R.K., Antin, P.B., 2003. Ephs and ephrins during early stages of chick embryogenesis. *Developmental Dynamics* **228**, 128-142.
12. Barrass, I., Crampin, E.J., Maini, P.K., 2006. Mode transitions in a model reaction-diffusion system driven by domain growth and noise. *Bulletin of Mathematical Biology* **68**, 981-995.
13. Barrios, A., Poole, R.J., Durbin, L., Brennan, C., Holder, N., Wilson, S.W., 2003. Eph/ephrin signaling regulates the mesenchymal-to-epithelial transition of the paraxial mesoderm during somite morphogenesis. *Current Biology* **13**, 1571-1582.
14. Baumgartner, W., Hinterdorfer, P., Ness, W., Raab, A., Vestweber, D., Schindler, H., Drenckhahn, D., 2000. Cadherin interaction probed by atomic force microscopy. *Proceedings of the National Academy of Sciences of the United States of America* **97**, 4005-4010.
15. Behrens, J., Birchmeier, W., Goodman, S.L., Imhof, B.A., 1985. Dissociation of Madin-Darby canine kidney epithelial cells by the monoclonal antibody anti-arc-1: mechanistic aspects and identification of the antigen as a component related to uvomorulin. *The Journal of Cell Biology* **101**, 1307-1315.

16. Bement, W.M., Forscher, P., Mooseker, M.S., 1993. A novel cytoskeletal structure involved in purse string wound closure and cell polarity maintenance. *The Journal of Cell Biology* **121**, 565-578.

17. Bergemann, A.D., Cheng, H.J., Brambilla, R., Klein, R., Flanagan, J.G., 1995. ELF-2, a new member of the Eph ligand family, is segmentally expressed in mouse embryos in the region of the hindbrain and newly forming somites. *Molecular and Cellular Biology* **15**, 4921-4929.

18. Bernus, O., Verschelde, H., Panfilov, A.V., 2003. Spiral wave stability in cardiac tissue with biphasic restitution. *Physical Review E* **68**, 021917.

19. Berx, G., Van Roy, F., 2001. The E-cadherin/catenin complex: an important gatekeeper in breast cancer tumorigenesis and malignant progression. *Breast Cancer Research* **3**, 289-293.

20. Beysens, D.A., Forgacs, G., Glazier, J.A., 2000. Cell sorting is analogous to phase ordering in fluids. *Proceedings of the National Academy of Sciences of the United States of America* **97**, 9467-9471.

21. Bitzur, S., Kam, Z., Geiger, B., 1994. Structure and distribution of N-cadherin in developing zebrafish embryos: morphogenetic effects of ectopic over-expression. *Developmental Dynamics* **201**, 121-136.

22. Bobick, B.E., Thornhill, T.M., Kulyk, W.M., 2007. Fibroblast growth factors 2, 4, and 8 exert both negative and positive effects on limb, frontonasal, and mandibular chondrogenesis *via* MEK-ERK activation. *Journal of Cellular Physiology* **211**, 233-243.

23. Boggon, T.J., Murray, J., Chappuis-Flament, S., Wong, E., Gumbiner, B.M., Shapiro, L., 2002. C-cadherin ectodomain structure and implications for cell adhesion mechanisms. *Science* **296**, 1308-1313.

24. Chappuis-Flament, S., Wong, E., Hicks, L.D., Kay, C.M., Gumbiner, B.M., 2001. Multiple cadherin extracellular repeats mediate homophilic binding and adhesion. *The Journal of Cell Biology* **154**, 231-243.

25. Chaturvedi, R., Huang, C., Kazmierczak, B., Schneider, T., Izaguirre, J.A., Glimm, T., Hentschel, H.G., Glazier, J.A., Newman, S.A., Alber, M.S., 2005. On multiscale approaches to three-dimensional modelling of morphogenesis. *Journal of the Royal Society Interface* **2**, 237-253.

26. Chen, C.P., Posy, S., Ben-Shaul, A., Shapiro, L., Honig, B.H., 2005. Specificity of cell-cell adhesion by classical cadherins: Critical role for low-affinity dimerization through beta-strand swapping. *Proceedings of the National Academy of Sciences of the United States of America* **102**, 8531-8536.

27. Christley, S., Alber, M.S., Newman, S.A., 2007. Patterns of mesenchymal condensation in a multiscale, discrete stochastic model. *PLoS Computational Biology* **3**, e76.

28. Chu, Y.S., Thomas, W.A., Eder, O., Pincet, F., Perez, E., Thiery, J.P., Dufour, S., 2004. Force measurements in E-cadherin-mediated cell doublets reveal rapid adhesion strengthened by actin cytoskeleton remodeling through Rac and Cdc42. *The Journal of Cell Biology* **167**, 1183-1194.

29. Chuai, M., Zeng, W., Yang, X., Boychenko, V., Glazier, J.A., Weijer, C.J., 2006. Cell movement during chick primitive streak formation. *Developmental Biology* **96**, 137-149.

30. Collier, J.R., Mcinerney, D., Schnell, S., Maini, P.K., Gavaghan, D.J., Houston, P., Stern, C.D., 2000. A cell cycle model for somitogenesis: mathematical formulation and numerical simulation. *Journal of Theoretical Biology* **207**, 305-316.

31. Cooke, J., Zeeman, E.C., 1976. A clock and wavefront model for control of the number of repeated structures during animal morphogenesis. *Journal of Theoretical Biology* **58**, 455-476.

32. Cooke, J.E., Kemp, H.A., Moens, C.B., 2005. EphA4 is required for cell adhesion and rhombomere-boundary formation in the zebrafish. *Current Biology* **15**, 536-542.

33. Cooperman, J., Neely, R., Teachey, D.T., Grupp, S., Choi, J.K., 2004. Cell division rates of primary human precursor B cells in culture reflect *in vivo* rates. *Stem Cells* **22**, 1111-1120.

34. Crampin, E.J., Gaffney, E.A., Maini, P.K., 1999. Reaction diffusion on growing domains: senarios for robust pattern formation. *Bulletin of Mathematical Biology* **61**, 1093-1120.

35. Cui, C., Yang, X., Chuai, M., Glazier, J.A., Weijer, C.J., 2005. Analysis of tissue flow patterns during primitive streak formation in the chick embryo. *Developmental Biology* **284**, 37-47.

36. Cui, C., 2005. *Dynamics of Cell Movement and Tissue Motion in Gastrulation and Micromass Cell Culture*, Ph.D. Dissertation, Indiana University, Department of Physics. Available for download from:

http://biocomplexity.indiana.edu/jglazier/cv.php?pg=2#sd.

37. Dan, D., Mueller, C., Chen, K., Glazier, J.A., 2005. Solving the advection-diffusion equations in biological contexts using the cellular Potts model. *Physical Review E* **72**, 041909.

38. De Bellard, M.E., Ching, W., Gossler, A., Bronner-Fraser, M., 2002. Disruption of segmental neural crest migration and ephrin expression in delta-1 null mice. *Developmental Biology* **249**, 121-130.

39. Debiais, F., Lemonnier, J., Hay, E., Delannoy, P., Caverzasio, J., Marie, P.J., 2001. Fibroblast growth factor-2 (FGF-2) increases N-cadherin expression through protein kinase C and Src-kinase pathways in human calvaria osteoblasts. *Journal of Cellular Biochemistry* **81**, 68-81.

40. Deng, C., Bedford, M., Li, C., Xu, X., Yang, X., Dunmore, J., Leder, P., 1997. Fibroblast growth factor receptor-1 (FGFR-1) is essential for normal neural tube and limb development. *Developmental Biology* **185**, 42-54.

41. Dequeant, M.L., Glynn, E., Gaudenz, K., Wahl, M., Chen, J., Mushegian, A., Pourquié, O., 2006. A complex oscillating network of signaling genes underlies the mouse segmentation clock. *Science* **314**, 1595-1598.

42. Diez del Corral, R., Olivera-Martinez, I., Goriely, A., Gale, E., Maden, M., Storey, K., 2003. Opposing FGF and retinoid pathways control ventral neural pattern, neuronal differentiation, and segmentation during body axis extension. *Neuron* **40**, 65-79.

43. Dillon, R., Othmer, H.G., 1999. A mathematical model for outgrowth and spatial patterning of the vertebrate limb bud. *Journal of Theoretical Biology* **197**, 295-330.

44. Dillon, R., Gadgil, C., Othmer, H.G., 2003. Short- and long-range effects of *Sonic hedgehog* in limb development. *Proceedings of the National Academy of Sciences of the United States of America* **100**, 10152-10157.

45. Downie, S.A., Newman, S.A., 1994. Morphogenetic differences between fore and hind limb precartilage mesenchyme: relation to mechanisms of skeletal pattern formation. *Developmental Biology* **162**, 195-208.

46. Downie, S.A., Newman, S.A., 1995. Different roles for fibronectin in the generation of fore and hind limb precartilage condensations. *Developmental Biology* **172**, 519-530.

47. Duband, J.L., Dufour, S., Hatta, K., Takeichi, M., Edelman, G.M., Thiery, J.P., 1987. Adhesion molecules during somitogenesis in the avian embryo. *The Journal of Cell Biology* **104**, 1361-1374.

48. Duboule, D., 2002. Making progress with limb models. *Nature* **418**, 492-493.

49. Dubrulle, J., McGrew, M.J., Pourquié, O., 2001. FGF signaling controls somite boundary position and regulates segmentation clock control of spatiotemporal *Hox* gene activation. *Cell* **106**, 219-232.

50. Dubrulle, J., Pourquié, O., 2004. Coupling segmentation to axis formation. *Development* **131**, 5783-5793.

51. Duguay, D., Foty, R.A., Steinberg, M.S., 2003. Cadherin-mediated cell adhesion and tissue segregation: qualitative and quantitative determinants. *Developmental Biology* **253**, 309-323.

52. Durbin, L., Brennan, C., Shiomi, K., Cooke, J., Barrios, A., Shanmugalingam, S., Guthrie, B., Lindberg, R., Holder, N., 1998. Eph signaling is required for

segmentation and differentiation of the somites. *Genes & Development* **12**, 3096-3109.

53. Eldar, A., Shilo, B.Z., Barkai, N., 2004. Elucidating mechanisms underlying robustness of morphogen gradients. *Current Opinion in Genetics & Development* **14**, 435-439.

54. Esser, A.T., Smith, K.C., Weaver, J.C., Levin, M., 2006. Mathematical model of morphogen electrophoresis through gap junctions. *Developmental Dynamics* **235**, 2144-2159.

55. Foty, R.A., Steinberg, M.S., 2005. The differential adhesion hypothesis: a direct evaluation. *Developmental Biology* **278**, 255-263.

56. Freeman, M., 2002. Morphogen gradients, in theory. *Developmental Cell* **2**, 689-690.

57. Fukumoto, T., Kema, I.P., Levin, M., 2005a. Serotonin signaling is a very early step in patterning of the left-right axis in chick and frog embryos. *Current Biology* **15**, 794-803.

58. Fukumoto, T., Blakely, R., Levin, M., 2005b. Serotonin transporter function is an early step in left-right patterning in chick and frog embryos. *Developmental Neuroscience* **27**, 349-363.

59. Frenkel, J., 1945. Viscous flow of crystalline bodies under the action of surface tension. *Journal of Physics* **4**, 385-431.

60. Friedlander, D.R., Mege, R.M., Cunningham, B.A., Edelman, G.M., 1989. Cell sorting-out is modulated by both the specificity and amount of different cell adhesion molecules (CAMs) expressed on cell surfaces. *Proceedings of the National Academy of Sciences of the United States of America* **86**, 7043-7047.

61. Gilbert, S.F., 2006. *Developmental Biology*. 8th edition (Sinauer Associates, Sunderland, Massachusetts).

62. Glazier, J.A., Graner, F., 1993. Simulation of the differential adhesion driven rearrangement of biological cells. *Physical Review E* **47**, 2128-2154.

63. Glazier, J.A., Zhang, Y., Swat, M., Zaitlen, B., Schnell, S., 2007. Coordinated Action of N-CAM, N-cadherin, EphA4 and ephrinB2 translates genetic prepattern into structure during somitogenesis in chick. *Current Topics in Developmental Biology* **81**, 205-247.

64. Godt, D, Tepass, U., 1998. Drosophila oocyte localization is mediated by differential cadherin-based adhesion. *Nature* **395**, 387-391.

65. Goldbeter, A., Gonze, D., Pourquié, O., 2007. Sharp developmental thresholds defined through bistability by antagonistic gradients of retinoic acid and FGF signaling. *Developmental Dynamics* **236**, 1495-1508.

66. Gossler, A., Hrabe de Angelis, M., 1998. Somitogenesis. *Current Topics in Developmental Biology* **38**, 225-287.

67. Graner, F., Glazier, J.A., 1992. Simulation of biological cell sorting using a two-dimensional extended Potts model. *Physical Review Letters* **69**, 2013-2016.

68. Gregor, T., Wieschaus, E.F., McGregor, A.P., Bialek, W., Tank, D.W., 2007a. Stability and nuclear dynamics of the Bicoid morphogen gradient. *Cell* **130**, 141-152.

69. Gregor, T., Tank, D.W., Wieschaus, E.F., Bialek, W., 2007b. Probing the Limits to Positional Information. *Cell* **130**, 153-164.

70. Grima, R., Schnell, S., 2007. Can tissue surface tension drive somite formation? *Developmental Biology* **81**, 435-460.

71. Gumbiner, B.M., 2005. Regulation of cadherin-mediated adhesion in morphogenesis. *Nature Reviews. Molecular Cell Biology* **6**, 622-634.

72. Gurdon, J.B., Bourillot, P.Y., 2001. Morphogen gradient interpretation. *Nature* **413**, 797-803.

73. Hamburger, V., Hamilton, H.L., 1992. A series of normal stages in the development of the chick embryo. *Developmental Dynamics* **195**, 231-272.

74. Halbleib, J.M., Nelson, W.J., 2006. Cadherins in development: cell adhesion, sorting, and tissue morphogenesis. *Genes & Development* **20**, 3199-3214.

75. Hara, K., Kimura, J., Ide, H., 1998. Effects of FGFs on the morphogenic potency and AER-maintenance activity of cultured progress zone cells of chick limb bud. *The International Journal of Developmental Biology* **42**, 591-599.

76. Harbott, L.K., Nobes, C.D., 2005. A key role for Abl family kinases in EphA receptor-mediated growth cone. *Molecular and Cellular Neuroscience* **30**, 1-11.

77. Hirai, H., Maru, Y., Hagiwara, K., Nishida, J., Takaku, F., 1987. A novel putative tyrosine kinase receptor encoded by the eph gene. *Science* **238**, 1717 -1720.

78. Henry, C.A., Hall, L.A., Burr Hille, M., Solnica-Krezel, L., Cooper, M.S., 2000. Somites in zebrafish doubly mutant for *knypek* and *trilobite* form without internal mesenchymal cells or compaction. *Current Biology* **10**, 1063-1066.

79. Horikawa, K., Radice, G., Takeichi, M., Chisaka, O., 1999. Adhesive subdivisions intrinsic to the epithelial somites. *Developmental Biology* **215**, 182-189.

80. Horikawa, K., Ishimatsu, K., Yoshimoto, E., Kondo, S., Takeda, H., 2006. Noise-resistant and synchronized oscillation of the segmentation clock. *Nature* **441**, 719-723.

81. Hynes, R.O., 2002. Integrins: bidirectional, allosteric signaling machines. *Cell* **110**, 673-687.

82. Itoh, N., Ornitz, D.M., 2004. Evolution of the *Fgf* and *Fgfr* gene families. *Trends in Genetics* **20**, 563-569.

83. Jiang, Y.J., Aerne, B.L., Smithers, L., Haddon, C., Ish-Horowicz, D., Lewis, J., 2000. Notch signalling and the synchronization of the somite segmentation clock. *Nature* **408**, 475-479.

84. Jochen, F., 2004. *The Emergence of Complexity*. (Kassel University Press, Kassel, Germany).

85. Kasemeier-Kulesa, J.C., Bradley, R., Pasquale, E.B., Lefcort, F., Kulesa, P.M., 2006. Eph/ephrins and N-cadherin coordinate to control the pattern of sympathetic ganglia. *Development* **133**, 4839-4847.

86. Katoh, M., Katoh, M., 2006. Cross-talk of WNT and FGF Signaling Pathways at GSK3beta to regulate beta-Catenin and SNAIL Signaling Cascades. *Cancer Biology & Therapy* **5**, 1059-1064.

87. Keller, E.F., Segal, L.A., 1971. Model for chemotaxis. *Journal of Theoretical Biology* **30**, 225-234.

88. Keynes, R.J., Stern, C.D., 1988. Mechanisms of vertebrate segmentation. *Development* **103**, 413-429.

89. Kicheva, A., Pantazis, P., Bollenbach, T., Kalaidzidis, Y., Bittig, T., Julicher, F., Gonzalez-Gaitan, M., 2007. Kinetics of morphogen gradient formation. *Science* **315**, 521-525.

90. Kimura, Y., Matsunami, H., Inoue, T., Shimamura, K., Uchida, N., Ueno, T.,

Miyazaki, T., Takeichi, M., 1995. Cadherin-11 expressed in association with mesenchymal morphogenesis in the head, somite, and limb bud of early mouse embryos. *Developmental Biology* **169**, 347-358.

91. Kiskowski, M.A., Alber, M.S., Thomas, G.L., Glazier, J.A., Bronstein, N.B., Pu, J., Newman, S.A., 2004. Interplay between activator-inhibitor coupling and cell-matrix adhesion in a cellular automaton model for chondrogenic patterning. *Developmental Biology* **271**, 372-387.
92. Kulesa, P.M., Fraser, S.E., 2002. Cell dynamics during somite boundary formation revealed by time-lapse analysis. *Science* **298**, 991-995.
93. Kulesa, P.M., Schnell, S., Rudloff, S., Baker, R.E., Maini, P.K., 2007. From segment to somite: Segmentation to epithelialization analyzed within quantitative frameworks. *Developmental Dynamics* **236**, 1392-1402.
94. Levin, M., Johnson, R.L., Stern, C.D., Kuehn, M., Tabin, C., 1995. A molecular pathway determining left-right asymmetry in chick embryogenesis. *Cell* **82**, 803-814.
95. Levin, M., 1997. Left-right asymmetry in vertebrate embryogenesis. *Bioessays* **19**, 287-296.
96. Levin, M., Mercola, M.,1999. Gap junction-mediated transfer of left-right patterning signals in the early chick blastoderm is upstream of *Shh* asymmetry in the node. *Development* **126**, 4703-4714.
97. Levin, M., Thorlin, T., Robinson, K.R., Nogi, T., Mercola, M., 2002. Asymmetries in H+/K+-ATPase and cell membrane potentials comprise a very early step in left-right patterning. *Cell* **111**, 77-89.

98. Levin, M., 2005. Left-right asymmetry in embryonic development: a comprehensive review. *Mechanisms of Development* **122**, 3-25.

99. Levin, M., Buznikov, G.A., Lauder, J.M., 2006. Of minds and embryos: left-right asymmetry and the serotonergic controls of pre-neural morphogenesis. *Developmental Neuroscience* **28**,171-185.

100. Lewandoski, M., Sun, X., Martin, G.R., 2000. Fgf8 signaling from the AER is essential for normal limb development. *Nature Genetics* **26**, 460-463.

101. Li, C., Xu, X., Nelson, D.K., Williams, T., Kuehn, M.R., Deng, C.X., 2005. FGFR1 function at the earliest stages of mouse limb development plays an indispensable role in subsequent autopod morphogenesis. *Development* **132**, 4755-4764.

102. Lin, A.L., Bertram, M., Martinez, K., and Swinney, H.L., 2000. Resonant Phase Patterns in a Reaction-Diffusion System. *Physical Review Letters* **84**, 4240–4243.

103. Linask, K.K., Ludwig, C., Han, M.D., Liu, X., Radice, G.L., Knudsen, K.A., 1998. N-cadherin/catenin-mediated morphoregulation of somite formation. *Developmental Biology* **202**, 85-102.

104. Lizarraga, G., Ferrari, D., Kalinowski, M., Ohuchi, H., Noji, S., Kosher, R.A., Dealy, C.N., 1999. FGFR2 signaling in normal and *limbless* chick limb buds. *Developmental Genetics* **25**, 331-338.

105. Lorger, M., Moelling, K., 2006. Regulation of epithelial wound closure and intercellular adhesion by interaction of AF6 with actin cytoskeleton. *Journal of Cell Science* **119**, 3385-3398.

106. Lu, P., Minowada, G., Martin, G.R., 2006. Increasing *Fgf4* expression in the mouse limb bud causes polysyndactyly and rescues the skeleton defects that result from loss of *Fgf8* function. *Development* **133**, 33-42.

107. Lyon, A.B., Parish, C.R., 1994, Determination of lymphocyte division by flow cytometry. *Journal of Immunological Methods* **171**, 131-137.

108. Mackenzie, D., 2006. Ramping up to multiscale: taking biomedical modeling to a new level. *Biomedical Computation Review* 19-26.

109. Maree, A.F., Hogeweg, P., 2001. How amoeboids self-organize into a fruiting body: multicellular coordination in *Dictyostelium discoideum*. *Proceedings of the National Academy of Sciences of the United States of America* **98**, 3879-3883.

110. Martin, G.R., 1998. The roles of FGFs in the early development of vertebrate limbs. *Genes & Development* **12**, 1571-1586.

111. Meinhardt, H., 1996. Models of biological pattern formation: common mechanism in plant and animal development. *The International Journal of Developmental Biology* **40**, 123-134.

112. Meinhardt, H., 2003. *The Algorithmic Beauty of Sea Shells.* Third edition (Springer, Berlin, Germany).

113. Mellitzer, G., Xu, Q., Wilkinson, D.G., 1999. Eph receptors and ephrins restrict cell intermingling and communication. *Nature* **400**, 77-81.

114. Mercola, M., Levin, M., 2001. Left-right asymmetry determination in vertebrates. *Annual Review of Cell and Developmental Biology* **17**, 779-805.

115. Merks, R.M.H., Brodsky, S.V., Goligorksy, M.S., Newman, S.A., Glazier, J.A., 2006. Cell elongation is key to *in silico* replication of *in vitro* vasculogenesis and subsequent remodeling. *Developmental Biology* **289**, 44-54.

116. Merks, R.H.M., Glazier, J.A., 2005. A cell-centered approach to developmental biology. *Physica A* **352**, 113-130.

117. Metropolis, N., Rosenbluth, A.W., Rosenbluth, M.N., Teller, A.H., Teller, E., 1953. Equations of state calculations by fast computing machines. *The Journal of Chemical Physics* **21**, 1087-1092.

118. Miura, T., Komori, M., Shiota, K., 2000. A novel method for analysis of the periodicity of chondrogenic patterns in limb bud cell culture: correlation of *in vitro* pattern formation with theoretical models. *Anatomy and Embryology* **201**, 419–428.

119. Miura, T., Shiota, K., Morriss-Kay, G., Maini, P.K., 2006. Mixed-mode pattern in *Doublefoot* mutant mouse limb–Turing reaction-diffusion model on a growing domain during limb development. *Journal of Theoretical Biology* **240**, 562-573.

120. Moftah, M.Z., Downie, S.A., Bronstein, N.B., Mezentseva, N., Pu, J., Maher, P.A., Newman, S.A., 2002. Ectodermal FGFs induce perinodular inhibition of limb chondrogenesis *in vitro* and *in vivo via* FGF receptor 2. *Developmental Biology* **249**, 270-282.

121. Moissoglu, K., Schwartz, M.A., 2006. Integrin signalling in directed cell migration. *Biology of the Cell* **98**, 547-555.

122. Mombach, J.C., Glazier, J.A., 1996. Single cell motion in aggregates of embryonic cells. *Physical Review Letters* **76**, 3032-3035.

123. Moon, A.M., Boulet, A.M., Capecchi, M.R., 2000. Normal limb development in conditional mutant of *Fgf4*. *Development* **127**, 989-996.

124. Moreno, T.A., Kintner, C., 2004. Regulation of segmental patterning by retinoic acid signaling during *Xenopus* somitogenesis. *Developmental Cell* **6**, 205-218.

125. Murai, K.K., Pasquale, E.B., 2003. 'Eph'ective signaling: forward, reverse and crosstalk. *Journal of Cell Science* **116**, 2823-2832.

126. Nakajima, Y., Morimoto, M., Takahashi, Y., Koseki, H., Saga, Y., 2006. Identification of EphA4 enhancer required for segmental expression and the regulation by Mesp2. *Development* **133**, 2517-2525.

127. Naski, M.C., Ornitz, D.M., 1998. FGF signaling in skeletal development. *Frontiers in Bioscience* **3**, d781-d794.

128. Nelson, W.J., Nusse, R., 2004. Convergence of Wnt, beta-catenin, and cadherin pathways. *Science* **303**, 1483-1487.

129. Newman, S.A., Frisch, H.L., 1979. Dynamics of skeletal pattern formation in developing chick limb. *Science* **205**, 662-668.

130. Newman, S.A., Forgacs, G., Muller, G.B., 2006. Before programs: the physical origination of multicellular forms. *The International Journal of Developmental Biology* **50**, 289-299.

131. Niessen, C.M., Gumbiner, B.M., 2002. Cadherin-mediated cell sorting not determined by binding or adhesion specificity. *The Journal of Cell Biology* **156**, 389-399.

132. Nieto, M.A., Gilardi-Hebenstreit, P., Charnay, P., Wilkinson, D.G., 1992. A receptor protein tyrosine kinase implicated in the segmental patterning of the hindbrain and mesoderm. *Development* **116**, 1137-1150.

133. Nikbakht, N., McLachlan, J.C., 1997. A proximo-distal gradient of FGF-like activity in the embryonic chick limb bud. *Cellular and Molecular Life Sciences* **53**, 447-451.

134. Niswander, L., Tickle, C., Vogel, A., Booth, I., Martin, G.R., 1993. FGF-4 replaces the apical ectodermal ridge and directs outgrowth and patterning of the limb. *Cell* **75**, 579-587.

135. Niswander, L., Jeffrey, S., Martin, G.R., Tickle, C., 1994. A positive feedback loop coordinates growth and patterning in the vertebrate limb. *Nature* **371**, 609-612.

136. Noji, S., Koyama, E., Myokai, F., Nohno, T., Ohuchi, H., Nishikawa, K., Taniguchi, S., 1993. Differential expression of three chick FGF receptor genes, FGFR1, FGFR2 and FGFR3, in limb and feather development. *Progress in Clinical and Biological Research* **383B**, 645-654.

137. Nose, A., Nagafuchi, A., Takeichi, M., 1988. Expressed recombinant cadherins mediate cell sorting in model systems. *Cell* **54**, 993-1001.

138. Ordahl, C.P., 1993. Myogenic lineages within the developing somite. In: Bernfield, M., (Editor), *Molecular Basis of Morphogenesis.* (John Wiley and Sons, New York, NY), pp. 165–176.

139. Ornitz, D.M., Xu, J., Colvin, J.S., McEwen, D.G., MacArthur, C.A., Coulier, F., Gao, G., Goldfarb, M., 1996. Receptor specificity of the fibroblast growth factor family. *The Journal of Biological Chemistry* **271**, 15292-15297.

140. Palmeirim, I., Henrique, D., Ish-Horowicz, D., Pourquié, O., 1997. Avian *hairy* gene expression identifies a molecular clock linked to vertebrate segmentation and somitogenesis. *Cell* **91**, 639-648.

141. Panorchan, P., Thompson, M.S., Davis, K.J., Tseng, Y., Konstantopoulos, K., Wirtz, D., 2006. Single-molecule analysis of cadherin-mediated cell-cell adhesion. *Journal of Cell Science* **119**, 66-74.

142. Pascoal, S., Andrade, R.P., Bajanca, F., Palmeirim, I., 2007. Progressive mRNA decay establishes an *mkp3* expression gradient in the chick limb bud. *Biochemical and Biophysical Research Communications* **352**, 153-157.

143. Paulsen, D.F., Solursh, M., 1988. Microtiter micromass cultures of limb-bud mesenchymal cells. *In Vitro Cellular & Developmental Biology* **24**, 138-147.

144. Pertz, O., Bozic, D., Koch, A.W., Fauser, C., Brancaccio, A., Engel, J., 1999. A new crystal structure, Ca^{2+} dependence and mutational analysis reveal molecular details of E-cadherin homoassociation. *The EMBO Journal* **18**, 1738-1747.

145. Poliakov, A., Cotrina, M., Wilkinson, D.G., 2004. Diverse roles of Eph receptors and ephrins in the regulation of cell migration and tissue assembly. *Developmental Cell* **7**, 465-480.

146. Poplawski, N.J., Swat, M., Gens J.S. Glazier, J.A., 2007. Adhesion between cells, diffusion of growth factors, and elasticity of the AER produce the paddle shape of the chick limb. *Physica A* **373C**, 521-532.

147. Pourquié, O., 2004. The chick embryo: a leading model in somitogenesis studies. *Mechanisms of Development* **121**, 1069-1079.

148. Pourquié, O., Tam, P.P., 2001. A nomenclature for prospective somites and phases of cyclic gene expression in the presomitic mesoderm. *Developmental Cell* **1**, 619-620.

149. Prakasam, A.K., Maruthamuthu, V., Leckband, D.E., 2006. Similarities between heterophilic and homophilic cadherin adhesion. *Proceedings of the National Academy of Sciences of the United States of America* **103**, 15434-15439.

150. Price, S.R., De Marco Garcia, N.V., Ranscht, B., Jessell, T.M., 2002. Regulation of motor neuron pool sorting by differential expression of type II cadherins. *Cell* **109**, 205-216.

151. Primmett, D.R., Stern, C.D., Keynes, R.J., 1988. Heat shock causes repeated segmental anomalies in the chick embryo. *Development* **104**, 331-339.

152. Primmett, D.R., Norris, W.E., Carlson, G.J., Keynes, R.J., Stern, C.D., 1989. Periodic segmental anomalies induced by heat shock in the chick embryo are associated with the cell cycle. *Development* **105**, 119-130.

153. Radice, G.L., Rayburn, H., Matsunami, H., Knudsen, K.A., Takeichi, M., Hynes, R.O., 1997. Developmental defects in mouse embryos lacking N-cadherin. *Developmental Biology* **181**, 64-78.

154. Reits, E.A., Neefjes, J.J., 2001. From fixed to FRAP: measuring protein mobility and activity in living cells. *Nature Cell Biology* **3**, E145-E147.

155. Rhoads, D.S., Guan, J.L., 2007. Analysis of directional cell migration on defined FN gradients: Role of intracellular signaling molecules. *Experimental Cell Research* **313**, 3859-3867.

156. Richardson, M.K., Jeffery, J.E., Tabin, C.J., 2004. Proximodistal patterning of the limb: insights from evolutionary morphology. *Evolution & Development* **6**, 1-5.

157. Rieu, J.P., Upadhyaya, A., Glazier, J.A., Ouchi, N.B., Sawada, Y., 2000. Diffusion and deformations of single hydra cells in cellular aggregates. *Biophysical Journal* **79**, 1903-1914.

158. Salazar-Ciudad, I., Jernvall, J., Newman, S.A., 2003. Mechanisms of pattern formation in development and evolution. *Development* **130**, 2027-2037.

159. Sanz-Ezquerro, J.J., Tickle, C., 2003. Fgf signaling controls the number of phalanges and tip formation in developing digits. *Current Biology* **13**, 1830-1836.

160. Sato, Y., Yasuda, K., Takahashi, Y., 2002. Morphological boundary forms by a novel inductive event mediated by Lunatic fringe and Notch during somitic segmentation. *Development* **129**, 3633-3644.

161. Sato, Y., Takahashi, Y., 2005. A novel signal induces a segmentation fissure by acting in a ventral-to-dorsal direction in the presomitic mesoderm. *Developmental Biology* **282**, 183-191.

162. Saunders, J.W. Jr., 2002. Is the progress zone model a victim of progress? *Cell* **110**, 541-543.

163. Savage, M.P., Fallon, J.P., 1995. FGF-2 mRNA and its antisense message are expressed in a developmentally specific manner in the chick limb bud and mesonephros. *Developmental Dynamics* **202**, 343-353.

164. Schnell, S., Maini, P.K., 2000. Clock and induction model for somitogenesis. *Developmental Dynamics* **217**, 415-420.

165. Schnell, S., Maini, P.K., McInerney, D., Gavaghan, D.J., Houston, P., 2002. Models for pattern formation in somitogenesis: a marriage of cellular and molecular biology. *Comptes Rendus Biologies* **325**, 179-189.

166. Schnell, S., Grima, R., Maini, P.K., 2007. Multiscale modeling in biology. *American Scientist* **95**, 134-142.

167. Shapiro, L., Fannon, A.M., Kwong, P.D., Thompson, A., Lehmann, M.S., Grubel, G., Legrand, J.F., Als-Nielsen, J., Colman, D.R., Hendrickson, W.A., 1995. Structural basis of cell-cell adhesion by cadherins. *Nature* **374**, 327-337.

168. Sick, S., Reinker, S., Timmer, J., Schlake, T., 2006. WNT and DKK determine hair follicle spacing through a reaction-diffusion mechanism. *Science* **314**, 1447-1450.

169. Sivasankar, S., Brieher, W., Lavrik, N., Gumbiner, B., Leckband, D., 1999. Direct molecular force measurements of multiple adhesive interactions between cadherin ectodomains. *Proceedings of the National Academy of Sciences of the United States of America* **96**, 11820-11824.

170. Steinberg, M.S., 1963. Reconstruction of tissues by dissociated cells. Some morphogenetic tissue movements and the sorting out of embryonic cells may have a common explanation. *Science* **141**, 401-408.

171. Steinberg, M.S., 1970. Does differential adhesion govern self-assembly processes in histogenesis? Equilibrium configurations and the emergence of a hierarchy among populations of embryonic cells. *The Journal of Experimental Zoology* **173**, 395-433.

172. Steinberg, M.S., Wiseman, L.L., 1972. Do morphogenetic tissue rearrangements require active cell movements? The reversible inhibition of cell sorting and tissue spreading by cytochalasin B. *The Journal of Cell Biology* **55**, 606-615.

173. Steinberg, M.S., Takeichi, M., 1994. Experimental specification of cell sorting, tissue spreading, and specific spatial patterning by quantitative differences in cadherin

expression. *Proceedings of the National Academy of Sciences of the United States of America* **91**, 206-209.

174. Stern, C.D., Fraser, S.E., Keynes, R.J., Primmett, D.R., 1988. A cell lineage analysis of segmentation in the chick embryo. *Development* **104S**, 231-244.

175. Summerbell, D., Wolpert, L., 1973. Precision of development in chick limb morphogenesis. *Nature* **244**, 228-230.

176. Sun, X., Lewandoski, M., Meyer, E.N., Liu, Y.H., Maxson, R.E. Jr., Martin, G.R., 2000. Conditional inactivation of *Fgf4* reveals complexity of signaling during limb bud development. *Nature Genetics* **25**, 83-86.

177. Sun, X., Mariani, F.V., Martin, G.R., 2002. Functions of FGF signalling from the apical ectodermal ridge in limb development. *Nature* **418**, 501-508.

178. Szebenyi, G., Savage, M.P., Olwin, B.B., Fallon, J.F., 1995. Changes in the expression of fibroblast growth factor receptors mark distinct stages of chondrogenesis *in vitro* and during chick limb skeletal patterning. *Developmental Dynamics* **204**, 446-456.

179. Tabata, T., 2001. Genetics of morphogen gradients. *Nature Reviews. Genetics* **2**, 620-630.

180. Tabata, T., Takei, Y., 2004. Morphogens, their identification and regulation. *Development* **131**, 703-712.

181. Tabin, C., Wolpert, L., 2007. Rethinking the proximodistal axis of the vertebrate limb in the molecular era. *Genes & Development* **21**, 1433-1442.

182. Takahashi. Y., Inoue. T., Gossler. A., Saga, Y., 2003. Feedback loops comprising Dll1, Dll3 and Mesp2, and differential involvement of Psen1 are essential for rostrocaudal patterning of somites. *Development* **130**, 4259-4268.

183. Takeichi, M., 1993. Cadherins in cancer: implications for invasion and metastasis. *Current Opinion in Cell Biology* **5**, 806-811.

184. Talamillo, A., Bastida, M.F., Fernandez-Teran, M., Ros, M.A., 2005. The developing limb and the control of the number of digits. *Clinical Genetics* **67**, 143-153.

185. Tepass, U., Truong, K., Godt, D., Ikura, M., Peifer, M., 2000. Cadherins in embryonic and neural morphogenesis. *Nature Reviews. Molecular Cell Biology* **1**, 91-100.

186. Townes, P.L., Holtfreter, J., 1955. Directed movements and selective adhesion of embryonic amphibian cells. *The Journal of Experimental Zoology* **128**, 53-120.

187. Turing, A., 1952. The chemical basis of morphogenesis. *Philosophical Transactions of the Royal Society of London, Series B, Biological Science* **237**, 37-72.

188. Umulis, D.M., Serpe, M., O'Connor, M.B., Othmer, H.G., 2006. Robust, bistable patterning of the dorsal surface of the *Drosophila* embryo. *Proceedings of the National Academy of Sciences of the United States of America* **103**, 11613-11618.

189. Van Oss, C., Panfilov, A.V., Hogeweg, P., Siegert, F., Weijer, C.J., 1996. Spatial pattern formation during aggregation of the slime mould *Dictyostelium discoideum*. *Journal of Theoretical Biology* **181**, 203-213.

190. Vargesson, N., Clarke, J.D., Vincent, K., Coles, C., Wolpert, L., Tickle, C., 1997. Cell fate in the chick limb bud and relationship to gene expression. *Development* **124**, 1909-1918.

191. Vogel, A., Tickle, C., 1993. FGF-4 maintains polarizing activity of posterior limb bud cells *in vivo* and *in vitro*. *Development* **119**, 199-206.

192. Vogel, A., Roberts-Clarke, D., Niswander, L., 1995. Effect of FGF on gene expression in chick limb bud cells *in vivo* and *in vitro*. *Developmental Biology* **171**, 507-520.

193. Von der Hardt, S., Bakkers, J., Inbal, A., Carvalho, L., Solnica-Krezel, L., Heisenberg, C.P., Hammerschmidt, M., 2007. The Bmp gradient of the zebrafish gastrula guides migrating lateral cells by regulating cell-cell adhesion. *Current Biology* **17**, 475-487.

194. Wolpert, L., 1969. Positional information and the spatial pattern of cellular differentiation. *Journal of Theoretical Biology* **25**, 1-47.

195. Wolpert, L., 1971. Positional information and pattern formation. *Current Topics in Developmental Biology* **6**, 183-224.

196. Wolpert, L., 1996. One hundred years of positional information. *Trends in Genetics* **12**, 359-364.

197. Wolpert, L., 2002. The progress zone model for specifying positional information. *The International Journal of Developmental Biology* **46**, 869-870.

198. Wood, A., Thorogood, P., 1994. Patterns of cell behaviour underlying somitogenesis and notochord formation in intact vertebrate embryos. *Developmental Dynamics* **201**, 151-167.

199. Xu, J., Liu, Z., Ornitz, D.M., 2000. Temporal and spatial gradients of *Fgf8* and *Fgf17* regulate proliferation and differentiation of midline cerebellar structures. *Development* **127**, 1833–1843.

200. Xu, Q., Mellitzer, G., Robinson, V., Wilkinson, D.G., 1999. *In vivo* cell sorting in complementary segmental domains mediated by Eph receptors and ephrins. *Nature* **399**, 267-271.

201. Xu, X., Weinstein, M., Li, C., Naski, M., Cohen, R.I., Ornitz, D.M., Leder, P., and Deng, C., 1998. Fibroblast growth factor receptor 2 (FGFR2) mediated reciprocal regulation loop between FGF8 and FGF10 is essential for limb induction. *Development* **125**, 767-775.

202. Xu, X., Weinstein, M., Li, C., Deng, C., 1999. Fibroblast growth factor receptors (FGFRs) and their roles in limb development. *Cell and Tissue Research* **296**, 33-43.

203. Xu, X., Li, W.E., Huang, G.Y., Meyer, R., Chen, T., Luo, Y., Thomas, M.P., Radice, G.L., Lo, C.W., 2001. Modulation of mouse neural crest cell motility by N-cadherin and connexin 43 gap junctions. *The Journal of Cell Biology* **154**, 217-230.

204. Yajima, H., Yoneitamura, S., Watanabe, N., Tamura, K., Ide, H., 1999. Role of N-cadherin in the sorting-out of mesenchymal cells and in the positional identity along the proximodistal axis of the chick limb bud. *Developmental Dynamics* **216**, 274-284.

205. Yamada, S., Pokutta, S., Drees, F., Weis, W.I., Nelson, W.J., 2005. Deconstructing the cadherin-catenin-actin complex. *Cell* **123**, 889-901.

206. Yang, X., Dormann, D., Munsterberg, A.E., Weijer, C.J., 2002. Cell movement patterns during gastrulation in the chick are controlled by positive and negative chemotaxis mediated by FGF4 and FGF8. *Developmental Cell* **3**, 425-437.

207. Yonei-Tamura, S., Endo, T., Yajima, H., Ohuchi, H., Ide, H., Tamura, K., 1999. FGF7 and FGF10 directly induce the apical ectodermal ridge in chick embryos. *Developmental Biology* **211**, 133-143.

208. Yoshida, C., Takeichi, M., 1982. Teratocarcinoma cell adhesion: Identification of a cell-surface protein involved in calcium-dependent cell aggregation. *Cell* **28**, 217–224.

209. Zajac, M., Jones, G.L., Glazier, J.A., 2000. Model of convergent extension in animal morphogenesis. *Physical Review Letters* **85**, 2022-2025.

210. Zeng, W., Thomas, G.L., Glazier, J.A., 2004. Non-Turing stripes and spots: a novel mechanism for biological cell clustering. *Physica A* **341**, 482-494.

211. Zhang, X., Ibrahimi, O.A., Olsen, S.K., Umemori, H., Mohammadi, M., Ornitz, D.M., 2006. Receptor specificity of the fibroblast growth factor family. The complete mammalian FGF family. *The Journal of Biological Chemistry* **281**, 15694-15700.

212. Zhu, B., Chappuis-Flament, S., Wong, E., Jensen, I.E., Gumbiner, B.M., Leckband, D., 2003. Functional analysis of the structural basis of homophilic cadherin adhesion. *Biophysical Journal* **84**, 4033-4042.

Vita

Ying Zhang was born in China on August 15th, the same day as Napoléon Bonaparte. She graduated from Shanghai Jiao Tong University with B.S. degrees in Applied Physics and International Finance and an M.S. degree in Theoretical Physics. This thesis was defended on August 14th, 2007 in partial fulfillment of the requirements for the degree of Doctor of Philosophy in Biophysics and Molecular Biology.